

MARTIN DOMINIK MESCH

LINEAR & NONLINEAR PLASMONIC SENSING

COMPLEX COUPLED PLASMONIC STRUCTURES,
FUNCTIONALIZATION, AND NONLINEAR EFFECTS

LINEAR & NONLINEAR
PLASMONIC SENSING
COMPLEX COUPLED PLASMONIC
STRUCTURES, FUNCTIONALIZATION,
AND NONLINEAR EFFECTS

Von der Fakultät Mathematik und Physik
der Universität Stuttgart zur Erlangung der Würde
eines Doktors der Naturwissenschaften (Dr. rer. nat.)
genehmigte Abhandlung

vorgelegt von
MARTIN DOMINIK MESCH
aus Schrobenhausen

Hauptberichter: Prof. Dr. Harald Giessen

Mitberichter: Prof. Dr. Martin Dressel

Vorsitzender: Prof. Dr. Christian Holm

Tag der mündlichen Prüfung: 27. Juni 2016

4. Physikalisches Institut der Universität Stuttgart
Juni 2016

Martin Dominik Mesch: *Linear & Nonlinear Plasmonic Sensing, Complex Coupled Plasmonic Structures, Functionalization, and Nonlinear Effects*, Juni 2016

PUBLICATIONS

IN SCIENTIFIC JOURNALS

- [1] N. Liu, T. Weiss, M. Mesch, L. Langguth, U. Eigenthaler, M. Hirscher, C. Sönnichsen, and H. Giessen. Planar Metamaterial Analogue of Electromagnetically Induced Transparency for Plasmonic Sensing. *Nano Lett.*, 10:1103–1107, 2010.
- [2] N. Liu, M. Mesch, T. Weiss, M. Hentschel, and H. Giessen. Infrared Perfect Absorber and Its Application As Plasmonic Sensor. *Nano Lett.*, 10:2342–2348, 2010.
- [3] R. Ameling, L. Langguth, M. Hentschel, M. Mesch, P. V. Braun, and H. Giessen. Cavity-enhanced localized plasmon resonance sensing. *Appl. Phys. Lett.*, 97(253116):1–6, 2010.
- [4] P. Rapp, M. Mesch, and H. Giessen. Regression Methods for Ophthalmic Glucose Sensing Using Metamaterials. *J. Electr. Comput. Eng.*, 2011(953064):1–12, 2011.
- [5] L. Wollet, B. Frank, M. Mesch, S. Hein, and H. Giessen. Plasmon hybridization in stacked metallic nanocups. *Optical Materials Express*, 2(10):1384–1390, 2012.
- [6] M. Mesch, C. Zhang, P. V. Braun, and H. Giessen. Functionalized Hydrogel on Plasmonic Nanoantennas for Noninvasive Glucose Sensing. *ACS Photonics*, 2:475–480, 2015.
- [7] M. Mesch, B. Metzger, M. Hentschel, and H. Giessen. Non-linear Plasmonic Sensing. *Nano Lett.*, 16(5):3155–3159, 2016.
- [8] M. Mesch, T. Weiss, M. Schäferling, R. S. Hegde, M. Hentschel, and H. Giessen. Analysis of Complex Coupled Plasmonic Oscillators for Sensing Applications. in preparation, 2016.

- [9] T. Weiss, M. Mesch, M. Schäferling, H. Giessen, W. Langbein, and Muljarov E.A. From dark to bright: First-order perturbation theory with analytical mode normalization for plasmonic nanoantenna arrays applied to refractive index sensing. *Phys. Rev. Lett.*, 116:237401, 2016.

AT CONFERENCES

- [1] M. Mesch, C. Zhang, P. V. Braun, P. Rapp, C. Tarin, and H. Giessen. Noninvasive optical glucose monitoring at physiological levels using a functionalized plasmonic sensor. In *CLEO Europe*, Munich, Germany, 2013.
- [2] T. Teutsch, M. Mesch, H. Giessen, and C. Tarin. Dynamic modeling of the hydrogel molecular filter in a metamaterial biosensing system for glucose concentration estimation. In *36th Annual International Conference of the IEEE Engineering in Medicine and Biology Society*, Chicago, USA, 2014.
- [3] M. Mesch, P. Rapp, C. Tarin, and H. Giessen. Metamaterial glucose sensing. In *EMRS Spring Meeting*, Strasbourg, France, 2012.
- [4] M. Mesch, N. Liu, T. Weiss, C. Sönnichsen, and H. Giessen. Metamaterial sensor for glucose and molecular monolayers using the plasmonic analog of eit. In *DPG Spring Meeting (Deutsche Physikalische Gesellschaft)*, Regensburg, Germany, 2010.
- [5] M. Mesch, C. Zhang, P. V. Braun, and H. Giessen. Plasmonic glucose sensing with functionalized hydrogels. In *DPG Spring Meeting (Deutsche Physikalische Gesellschaft)*, Dresden, Germany, 2014.
- [6] M. Mesch, B. Metzger, M. Hentschel, and H. Giessen. Non-linear plasmonic sensing. In *DPG Spring Meeting (Deutsche Physikalische Gesellschaft)*, Regensburg, Germany, 2016.

CONTENTS

1	INTRODUCTION	1
2	BASIC EQUATIONS AND FUNDAMENTAL PRINCIPLES	5
2.1	Basics of Electrodynamics	5
2.1.1	Maxwell's Equations	5
2.1.2	The Lorentz Oscillator Model	7
2.1.3	Optical Properties of Noble Metals	9
2.2	Localized Surface Plasmon Resonances	11
2.3	Nonlinear Optics	12
2.3.1	Nonlinear Polarization and Susceptibility	12
2.3.2	Nonlinear Processes of Second Order	13
2.3.3	Nonlinear Processes of Third Order	15
3	METHODS	17
3.1	Simulation	17
3.2	Fabrication	18
3.2.1	Electron Beam Lithography	18
3.2.2	Optical Lithography	20
3.2.3	Silicone Casting	21
3.3	Measurement	22
3.3.1	Fourier Transform Infrared Spectroscopy	22
3.3.2	Centroid Evaluation of Spectral Resonance Features	24
3.3.3	Ultrashort Laser Pulses for Nonlinear Spectroscopy	26
4	THE MICROFLUIDIC SENSOR CELL	29
5	SENSING WITH COMPLEX COUPLED STRUCTURES	35
5.1	Perturbation Theory	37
5.2	Calculation of the Mode Volume	40
5.3	Characterization of an EIT-like Structure	42
5.4	Experimental Verification	48
5.5	Conclusion	50

6	FUNCTIONALIZED HYDROGEL ASSISTED PLASMONIC SENSING	53
6.1	The Boronic Acid Functionalized Hydrogel	56
6.2	Synthesis of Acrylamidophenylboronic Acid	57
6.3	Fabrication of the Hydrogel Layer	59
6.4	Characterization of the Sensor	63
6.4.1	Response of a Hydrogel Covered Nano- antenna Array	64
6.4.2	Investigation of Hydrogel Degradation . .	68
6.4.3	Other Influences on the Sensor	69
6.4.4	Filtering Capabilities of the Hydrogel . . .	71
6.5	Layer-by-layer Growth for Ultrathin Films	73
6.5.1	Synthesis	74
6.5.2	Layer-by-layer Growth	75
6.5.3	Characterization	77
6.6	Summary & Noninvasive Tear Glucose Sensing .	78
7	GLUCOSE SENSING WITH SEIRA	83
7.1	Measurement of High Concentrations	84
7.2	Estimation of the Signal Strength	87
7.3	Possible Approaches for Improvement	88
8	NONLINEAR PLASMONIC SENSING	91
8.1	The Anharmonic Oscillator Model	93
8.2	Modeling the Nonlinear Response	96
8.3	Nonlinear Spectroscopy	101
8.4	Nonlinear Sensing	103
8.5	Conclusions	106
9	SUMMARY & OUTLOOK	111
	BIBLIOGRAPHY	117

ACRONYMS

AAPBA	N-3-acrylamidophenylboronic acid
APBA	3-aminophenylboronic acid
BSA	bovine serum albumin
CHES	2-(cyclohexylamino) ethanesulfonic acid
DFG	difference frequency generation
EBL	electron beam lithography
EGDM	ethylene glycol dimethacrylate
EIT	electromagnetically induced transparency
FOM	figure of merit
FTIR	Fourier-transform infrared
FWHM	full width at half maximum
FWM	four wave mixing
HEMA	hydroxyethylmethacrylate
IR-651	Irgacure 651 photoinitiator
LbL	layer-by-layer
LSPR	localized surface plasmon resonance
MCT	mercury cadmium telluride
MPMS	methacryloxypropyltrimethoxysilane
NMR	nuclear magnetic resonance
ODT	octadecanethiol
P(AAm-AAPBA)	poly[acrylamide-co-3-(acrylamido)-phenylboronic acid]
PBA	phenylboronic acid
PBS	phosphate buffered saline
PDMS	poly(dimethylsiloxane)
PMMA	polymethylmethacrylate

PMT	photomultiplier tube
PVA	polyvinyl alcohol
RIU	refractive index unit
SEIRA	surface enhanced infrared absorption
SEM	scanning electron microscope
SFG	sum frequency generation
SHG	second harmonic generation
SNR	signal-to-noise ratio
THG	third harmonic generation

LIST OF FIGURES

Figure 2.1	Evolution of the refractive index in the Lorentz oscillator model	9
Figure 2.2	Drude model fit to experimental data . .	10
Figure 2.3	Schematic picture of second order nonlinear processes	14
Figure 2.4	Schematic picture of third order nonlinear processes	15
Figure 3.1	Lithography process with positive tone resist	19
Figure 3.2	Schematic of the FTIR spectrometer setup	23
Figure 3.3	Centroid evaluation for tracking small spectral shifts	25
Figure 4.1	Sensor cell assembled from glass slides. .	30
Figure 4.2	Three layer microfluidic cell.	31
Figure 4.3	Improved casting of the PDMS layer. . . .	32
Figure 5.1	Possible sensing schemes	36
Figure 5.2	Schematic of the investigated plasmonic structure	43
Figure 5.3	Simulated spectra of the coupled structure	44
Figure 5.4	Field plots of the coupled structure	45

Figure 5.5	Comparison of different sensitivity values	47
Figure 5.6	Experimental investigation of the structure	49
Figure 6.1	Specific detection of molecules by functionalization.	53
Figure 6.2	Schematic of the hydrogel assisted plasmonic sensor	55
Figure 6.3	Components of the functionalized hydrogel	56
Figure 6.4	Complex formation of phenylboronic acids with 1,2-cis-diols	57
Figure 6.5	Old hydrogel layer fabrication process . .	60
Figure 6.6	New hydrogel layer fabrication process .	61
Figure 6.7	Simulation of thin film interference in the hydrogel layer	62
Figure 6.8	Height profile of flat and roughened polymer surface	63
Figure 6.9	Temporal evolution of the hydrogel sensor signal	65
Figure 6.10	Wavelength shift and response time of the hydrogel sensor	66
Figure 6.11	Reversibility of the hydrogel sensor . . .	68
Figure 6.12	Influence of pH/ionic strength on the hydrogel	70
Figure 6.13	Filtering capabilities of the hydrogel . . .	72
Figure 6.14	Different layer-by-layer assembly systems	73
Figure 6.15	Setup for synthesis of P(AAm-AAPBA) .	75
Figure 6.16	Layer-by-layer assembly process	76
Figure 6.17	Layer-by-layer assembled hydrogel: Characterization	77
Figure 6.18	Picture of contact lens for glucose sensing	79
Figure 6.19	Simplified setup to demonstrate noninvasive glucose sensing	80
Figure 7.1	Illustration of signals in refractive index sensing and SEIRA	84
Figure 7.2	Transmittance spectrum of D-glucose in the infrared wavelength range	85
Figure 7.3	SEIRA measurement of a dry glucose film	85

Figure 7.4	SEIRA measurement of highly concentrated aqueous glucose solutions	86
Figure 7.5	Comparison of octadecanethiol and glucose molecules	87
Figure 7.6	Infrared transmittance spectrum of HEMA	89
Figure 8.1	Principle of linear and nonlinear plasmonic sensing	92
Figure 8.2	Anharmonic oscillator model: Absorbance	98
Figure 8.3	Anharmonic oscillator model: Transmittance	100
Figure 8.4	Setup for nonlinear spectroscopy and sensing	102
Figure 8.5	Linear and third harmonic spectra of nano-antenna arrays for two analyte solutions .	104
Figure 8.6	Calculated sensor signals from the measured spectra	105
Figure 8.7	Time traces of linear and nonlinear sensor signals	107

ABSTRACT

Plasmonic nanostructures are intensely investigated as sensors due to their high sensitivity to changes in their nearest dielectric environment. This thesis includes work regarding three main topics of plasmonic sensing, namely, the optimization of the plasmonic nanostructure, functionalization for a particular analyte, and the general detection scheme.

We present our approach of combining full wave simulations and perturbation theory to study complex coupled plasmonic nanostructures. In particular, we focus on the well studied structure of a dipole antenna coupled to an antenna pair supporting a quadrupolar mode, which exhibits a tunable Fano resonance. We derive the required expressions for the resonance shift, mode volume, and electromagnetic energy density and provide a comparison of simulation, theory, and experimental results. A key point is the calculation of the mode volume taking the leaky nature of the plasmonic resonators into account. Based on the simulated local field distributions, our technique allows to optimize the sensor with respect to different sensing tasks, such as bulk refractive index sensing or detection of a single molecular layer on the gold nanoantennas.

However, additional steps have to be taken to provide specificity for a particular analyte. In order to achieve this goal, gold nanoantennas are coated with a thin layer of a boronic acid functionalized hydrogel, which reversibly swells in the presence of glucose. This process is especially sensitive to low glucose concentrations and allows for measurement of values in the physiological millimolar range. The boronic acid is highly specific to glucose, and large molecules, such as proteins, which could cause possible disturbances to the measurements, are successfully blocked from the plasmonic sensing volume by the hydrogel film. Different systems are investigated to obtain ultrathin hydrogel films for a fast sensor response. Our concept is thus suited to detect physiological glucose levels in the

tear liquid under the presence of ambient proteins using functionalized plasmonic sensors on contact lenses at eyesafe wavelengths for optical readout. In an approach to avoid the often complex step of functionalization, we study the principle of surface enhanced infrared absorption with the same analyte system.

Finally, we introduce the concept of nonlinear plasmonic sensing, relying on third harmonic generation from simple plasmonic nanoantennas. Due to the nonlinear conversion process we observe a larger sensitivity to a local change in the refractive index as compared to the commonly used linear localized surface plasmon resonance sensing. We utilize an anharmonic oscillator model to describe the behavior of our system. In order to determine the spectral position of highest sensitivity, we perform linear and third harmonic spectroscopy on plasmonic nanoantenna arrays, which are the fundamental building blocks of our sensor. Furthermore, simultaneous detection of linear and nonlinear signals allows quantitative comparison of both methods, providing further insight into the working principle of our sensor. We find that nonlinear sensing gives about seven times higher relative signal changes, while the signal-to-noise ratio is comparable to linear plasmonic sensing.

ZUSAMMENFASSUNG

Die vorliegende Arbeit beschäftigt sich mit der Verwendung plasmonischer Nanostrukturen als Sensoren. Werden solche metallischen Strukturen mit Licht bestrahlt, werden kollektive Oszillationen der quasi-freien Leitungselektronen, sogenannte Plasmonen, angeregt. Das resonante Verhalten hängt, aufgrund der entstehenden lokalisierten elektromagnetischen Felder, sehr empfindlich von den dielektrischen Eigenschaften ihrer nächsten Umgebung ab. Daher sind solche einfachen plasmonischen Strukturen ideal als lokale Brechungsindexsensoren geeignet. Bei der Ausnutzung dieser Effekte spielen drei Gesichtspunkte eine wesentliche Rolle: Die Optimierung der verwendeten Struktur im Hinblick auf möglichst große Signale

bei gleichen Änderungen, die Beschränkung der grundsätzlich sehr allgemeinen Sensorantwort auf einen gewünschten Analyten, sowie die Art der Detektion. Diese Themen werden mit den folgenden Untersuchungen behandelt.

Auf der Suche nach dem optimalen plasmonischen Sensor wurden, unter Verwendung diverser Fertigungsmethoden, angefangen von der chemischen Synthese bis hin zur Elektronenstrahlolithographie, verschiedenste Arten und Formen von Nanostrukturen untersucht. Änderungen wurden dabei in den unterschiedlichen Experimenten beispielsweise über eine Verschiebung der plasmonischen Resonanz, oder aber über eine Differenz in der Transmission oder Absorption detektiert. Weiterhin wurden sowohl Änderungen im umgebenden Volumen als auch an der Oberfläche der Strukturen betrachtet. Motiviert und beeinflusst von den jeweiligen Experimenten und Anwendungsgebieten entstanden dabei verschiedene Definitionen für die Güte eines plasmonischen Sensors, also letztlich der kleinsten noch detektierbaren Änderung im Sensorvolumen. Zusätzliche Betrachtungen werden im Falle von gekoppelter plasmonischer Strukturen notwendig, da durch die Kopplung zusätzliche resonante Moden entstehen. Dies legt eine Untersuchung auf Basis der lokalisierten Felder nahe.

Im ersten Teil der Arbeit wurde daher eine Anordnung von gekoppelten Nanoantennen, im Hinblick auf die unterschiedlichen Anwendungsszenarien analysiert und ihre Sensitivität mit den Nahfeldern in Relation gesetzt. Dazu beschreiben wir die Änderungen in der Umgebung der Struktur zum einen mit Hilfe einer Störungstheorie und zum anderen der vollständigen numerischen Lösung der Maxwellgleichungen in Simulationen. Besonders zu beachten sind dabei die unendlich ausgedehnten Felder der entsprechenden Eigenmoden. Dabei stellen wir fest, dass die Sensitivität von der Energiedichte im plasmonischen Resonator abhängt. Die Theorie stimmt qualitativ mit den numerischen Simulationen überein und erlaubt die Optimierung der Struktur in Bezug auf die optimale Kopplungsstärke. Verschiebungen der Resonanzfrequenz als Sensorsignal sind demnach vorzugsweise anhand der energetisch höher liegenden Mode und bei schwacher Kopplung zu detek-

tieren. Intensitätsdifferenzen in Transmission profitieren hingegen von den besser modulierten Spektren und steileren Flanken im Bereich starker Kopplung. Das Verhalten im Falle von Änderungen im Bereich der Antennenoberflächen entspricht weitestgehend dem für entsprechend kleine Änderungen im Volumen. Außerdem ermöglicht die Theorie eine Vorhersage des Sensorsignals auf Basis einer einmaligen Berechnung der Eigenmoden. Die theoretisch betrachtete Struktur wurde außerdem in verschiedenen Konfigurationen mit Hilfe von Elektronenstrahlolithographie und einem Mehrlagenprozess hergestellt. Die Charakterisierung der Proben mittels Infrarotspektroskopie bestätigt qualitativ die theoretischen Vorhersagen.

Ebenso wie bei den Messungen im oben stehenden Abschnitt fokussieren wir uns auch in allen folgenden Messungen auf die Untersuchung von Analyten in Lösung. Die Handhabung der Flüssigkeiten in Kombination mit den optischen Komponenten der Messapparaturen und den hergestellten Nanostrukturen, sowie die Zuverlässigkeit und Reproduzierbarkeit der Messungen, stellen dabei hohe Anforderungen an die Sensorzelle. Die in mehreren Schritten entwickelte mikrofluidische Sensorzelle besteht dazu aus drei Komponenten mit jeweils spezifischer Funktionalität.

Von den im Deckel integrierten Anschlüssen für medizinisches Equipment wird die Flüssigkeit über gefräste Kanäle an der Unterseite zur nächsten Schicht geführt. Diese besteht aus einem etwa 3 mm dicken Silikonmaterial, welches die Zelle nach oben gegen den Deckel und nach unten gegen das Probensubstrat abdichtet. Dieses nicht toxische, chemisch inerte und transparente Material kann gegossen werden und formt bei der Aushärtung selbst mikroskopische Strukturen ab. So wurde auf der Unterseite ein 70 μm hoher Kanal erzeugt, der die über durchgehende Löcher von oben eingespeiste Flüssigkeit über die Probe leitet. Die Probe selbst sitzt dabei in einer passgenauen Aussparung in der Basisplatte. Diese erlaubt die Befestigung im Messaufbau und die Verschraubung mit den anderen Bestandteilen. Weitere konische Bohrungen in Deckel und Basisplatte stellen die ungestörte Transmission von Licht sicher.

Neben der einfachen und schnellen Montierbarkeit, der Wiederverwendbarkeit und der Dichtheit der Zelle, wird durch den mikrofluidischen Kanal auch die Absorption durch Wasser über der Probe minimiert und das geringe Volumen garantiert einen schnellen Austausch verschiedener Messlösungen. Außerdem reduziert die Verwendung des Probensubstrats als untere Abgrenzung der Zelle die Anzahl der Grenzflächen im optischen Weg.

Für Messungen mit Hydrogelen und biologischen Substanzen waren weitere Verbesserungen erforderlich. Dabei mussten insbesondere die rauen Oberflächen der gefrästen Kanäle vermieden werden. Zusätzlich sollte die Anzahl an Ecken und Hinterschneidungen soweit wie möglich verkleinert werden um Rückstände beim Wechsel der Messlösungen zu minimieren. Weiterhin war eine Reduzierung des Durchmessers der verwendeten Schläuche nötig um Verzögerungen beim Austausch des Analyten zu umgehen.

Bei der Herstellung der finalen Zelle wurden daher die Anschlusschläuche direkt in die Silikonkomponente eingegossen. Entscheidend ist dabei die Verwendung von Silikonschläuchen, die sich im Gegensatz zu den weit verbreiteten Schläuchen aus Polyethylen perfekt mit dem umgebenden Material verbinden. Die Schlauchenden wurden während des Gießens auf kurze Stücke einer Injektionsnadel gesteckt, welche zuvor auf die Enden der Negativform des mikrofluidischen Kanals geklebt wurden. Dadurch wurden sie sowohl abgedichtet als auch fixiert, und es ergab sich nach dem Abziehen des fertigen Silikonteils ein gleichmäßiger Übergang zwischen Schlauch und Kanal. Der Deckel hatte in diesem Fall lediglich die Aufgabe alle Komponenten mit leichtem gleichmäßigem Druck zusammen zu halten.

Der zweite Teil der Arbeit beschäftigt sich mit der Funktionalisierung plasmonischer Sensoren. Unabhängig von der verwendeten Struktur besteht die Herausforderung bei dieser Art der Sensorik oft darin, die sehr allgemeine Reaktion, nämlich jegliche Änderungen des Brechungsindex, auf einen vorzugsweise einzelnen gewünschten Analyten einzugrenzen. Eine gängige Methode besteht darin eine Hälfte eines Molekülpaars

mit starker Affinität auf der Oberfläche der Nanostrukturen zu immobilisieren. Befindet sich das zugehörige Molekül dann in der Messlösung, wird es durch die Reaktion mit seinem Gegenstück ebenfalls an die Sensoroberfläche gebunden. Nachdem alle übrigen Verunreinigungen weg gespült wurden, kann dann eine spezifische Änderung detektiert werden. Häufig ist die Bindung allerdings permanent, und der Sensor kann nur einmal verwendet werden.

Ein anderes Konzept von Sensoren wurde auf Basis von Hydrogelen entwickelt. Dabei handelt es sich um mit Wasser getränkte, hydrophile, vernetzte Polymere die in verschiedenen Bereichen, wie etwa als Material für Kontaktlinsen oder bei der kontrollierten Abgabe von pharmazeutischen Wirkstoffen, bereits Anwendung finden. Durch entsprechende Funktionalisierung lässt sich eine Reaktion des Hydrogels auf unterschiedliche Änderungen erreichen. Die Reaktion, zumeist eine reversible Volumenänderung des Gels, kann dann als Sensorsignal ausgelesen werden.

Unser Ansatz besteht nun darin die enorme Sensitivität plasmonischer Antennen mit den Vorteilen eines Hydrogels zu kombinieren. Demonstriert werden soll dieses System anhand eines auf Glucose reagierenden Sensors. Dazu wird die Gleichgewichtsreaktion von Glucose mit Phenylboronsäure ausgenutzt. Diese Säure bildet einen negativ geladenen Komplex mit 1,2-cis-Diolen, zu denen auch Glucose zählt. Ist die Säure kovalent an das Hydrogel gebunden, verteilt sich die Ladung auf das Polymer Netzwerk und erzeugt ein Donnan-Potential zwischen Hydrogel und der umgebenden Lösung. Die dadurch ausgelösten Diffusionsprozesse führen zum Anschwellen des Hydrogels durch einströmendes Wasser. Aufgrund der unterschiedlichen Brechungsindizes von Wasser und Polymer ändert sich dadurch auch der effektive Brechungsindex des Hydrogels. Die Auswirkungen lassen sich wiederum präzise durch die Verschiebung der plasmonischen Resonanz nachverfolgen.

Zur Einbindung der Säure in das Polymer musste diese mit einer entsprechenden funktionellen Gruppe versehen werden. Hierzu wurden zwei verschiedene Synthesewege getestet. Um möglichst schnell die Einstellung eines Gleichgewichtszustands

zu erreichen, muss eine dünne Hydrogelschicht auf die zuvor hergestellten Nanoantennen aufgebracht werden. Dazu wurde ein geeigneter Prozess auf Basis radikalischer Polymerisation entwickelt. Die mit einer $1\ \mu\text{m}$ dicken Polymerschicht bedeckten Proben wurden anschließend durch die Messung von Infrarotspektren charakterisiert. Um die spektrale Verschiebung der plasmonischen Resonanzen möglichst genau verfolgen zu können, wurde bei der Auswertung auf die Position eines Flächenschwerpunkts zurückgegriffen. Die Fläche wird hierbei durch das Resonanzspektrum und einen vorher festgelegten Grenzwert bestimmt. Im Gegensatz zur Position des Extremwertes, der empfindlich durch Rauschen und Intensitätsschwankungen beeinflusst wird, ermöglicht es diese Methode durch Einbeziehung der Informationen aus einem breiteren spektralen Bereich, die Verschiebung wesentlich genauer zu bestimmen.

Durch eine kontinuierliche Messung von Glucoselösungen mit wechselnden Konzentrationen zwischen 0 und 100 mmol/l wurde neben den Resonanzverschiebungen im Gleichgewichtszustand auch der zeitliche Verlauf aufgezeichnet. Unter gleichen Voraussetzungen wurde eine Kontrollmessung an Nanoantennen ohne Hydrogelbeschichtung durchgeführt. Die Analyse der Messungen offenbart eine deutlich erhöhte Resonanzverschiebung für die mit Hydrogel bedeckten Proben. Während ohne Hydrogel der Brechungsindexunterschied lediglich durch die zusätzlichen Glucosemoleküle hervorgerufen wird und kaum nachgewiesen werden kann, verursachen die zusätzlich in das Polymer einströmenden Wassermoleküle eine wesentlich ausgeprägtere Änderung. Der Effekt zeigt das durch die endliche Anzahl an Phenylboronsäuremolekülen im Polymer hervorgerufene Sättigungsverhalten.

Weiterhin ist festzustellen, dass die Einstellung eines Gleichgewichtszustands und somit die Antwortzeit des Sensors von der Glucosekonzentration abhängt. Für niedrige Konzentrationen ist auch der Wasseranteil im Polymer gering, woraus sich eine Einschränkung der Diffusionsrate von Glucosemolekülen in das Polymer und folglich eine langsamere Reaktion ergibt. Bei höheren Ausgangskonzentrationen ist der Wasseranteil höher und weitere Glucosemoleküle gelangen schneller in das

Hydrogel. Abhilfe kann hier die Nutzung eines vorgeschwol-
lenen Hydrogels bringen. Die Verbesserung der Reaktionszeit
bei kleinen Konzentrationen würde jedoch auf Kosten des ma-
ximalen Detektionsbereichs erfolgen. Da aus Simulationen be-
kannt ist, dass sich die Ausdehnung der überhöhten Felder auf
einen Bereich von wenigen hundert Nanometern um die An-
tennen beschränkt, könnte alternativ auch die Dicke der Hy-
drogelbeschichtung weiter verringert werden. Eine dazu nöti-
ge, abweichende Herstellungsmethode wird weiter unten dis-
kutiert.

Neben einer deutlichen Reaktion auf den entsprechenden
Analyten spielt auch der Einfluss anderer Substanzen in der
Messlösung eine große Rolle in der Sensorentwicklung. Idea-
lerweise ist die Sensorantwort auf den gewünschten Analyten
beschränkt. In der Realität müssen jedoch oft Kreuzsensitivitä-
ten und Umwelteinflüsse berücksichtigt werden. Dahingehen-
de Untersuchungen sollten natürlich möglichst unter Einbezie-
hung des erwarteten Anwendungsgebietes erfolgen. Da das
hier verwendete Sensorprinzip auf der Bildung eines geladen-
en Komplexes mit einer Säure in wässrigen Lösungen basiert,
ist insbesondere der Einfluss von pH-Wert und Ionenstärke re-
levant. Während der pH-Wert eine Verschiebung des Gleich-
gewichts hervorruft, führen hohe Ionenkonzentrationen zu ei-
nem verringerten Effekt durch die gebildeten geladenen Kom-
plexe. Aus den durchgeführten Messungen lassen sich die ent-
sprechenden Auswirkungen auf den Messbereich ableiten.

Vor allem in biologischen Systemen ist es zudem notwendig
mit Proteinen in der Messlösung umzugehen, weshalb beispiel-
haft Studien mit Albumin durchgeführt wurden. Die Konzen-
trationen entsprechen dabei Werten, wie sich auch im mensch-
lichen Organismus vorkommen. Auf Proben ohne Hydrogel
verursachen die klobigen Proteine die erwartete enorme Reso-
nanzverschiebung. Trotz wesentlich geringerer Konzentration
im Vergleich zu Glucose, übertrifft das Störsignal das Nutzsi-
gnal ohne Hydrogel bei Weitem. Dies ist auf das Massenver-
hältnis von ca. 370:1 zwischen Protein und Glucose zurückzu-
führen. Des Weiteren haften die Proteine an der Sensoroberflä-
che und verhindern auch nach dem Wechsel auf reine Lösun-

gen, dass das Signal seinen Ausgangswert erreicht. Die Hydrogelbeschichtung hingegen unterbindet erfolgreich das Eindringen der Proteine in den sensitiven Bereich der plasmonischen Antennen und erlaubt nach wie vor den Nachweis verschiedener Glucosekonzentrationen.

Die biologische Verträglichkeit von Hydrogel und Goldpartikeln begünstigt außerdem die künftige Anwendung in medizinischen Produkten. Speziell seien hier Kontaktlinsen zur nichtinvasiven Messung des Zuckerspiegels in der Tränenflüssigkeit genannt. Die bereits oft aus Hydrogelen hergestellten weichen Linsen würden um Nanoantennen und Funktionalisierung erweitert und so zu einem komplett passiven, optisch auslesbaren System. Die spektrale Verschiebung der Resonanz würde dann durch die Reflektivität bei einer festen Wellenlänge im Infrarotbereich überwacht. Hierzu wurde im Rahmen des vom Ministerium für Wissenschaft, Forschung und Kunst geförderten *Ideenwettbewerb Biotechnologie und Medizintechnik Baden-Württemberg* ein entsprechend vereinfachter Demonstrationsaufbau mit integrierter Elektronik und Signalübertragung per USB Anschluss angefertigt.

Wie zuvor angemerkt, würde sich eine dünnere Hydrogelschicht auf den Nanoantennen positiv auf die Reaktionszeit des Sensors auswirken. Deshalb wurde alternativ zur bereits beschriebenen Herstellungsmethode ein Verfahren zum Aufbau des Polymers aus monomolekularen Schichten (Layer-by-layer Verfahren) geprüft. Dabei handelt es sich um einen zyklischen Prozess in dem üblicherweise gegensätzlich geladene Polymere abwechseln auf dem Substrat adsorbiert werden. Die entsprechenden Polymerlösungen werden dabei durch Eintauchen, Aufschleudern oder Sprühen aufgebracht, während loses Material zwischen den einzelnen Schritten abgewaschen wird. Ein ähnliches System lässt sich auch mit Hilfe der reversiblen kovalenten Wechselwirkung zwischen der bereits bekannten Phenylboronsäure und den Hydroxidgruppen von Polyvinylalkohol konstruieren. Dazu wurde die Säure mit Acrylamid copolymerisiert und abwechselnd mit Polyvinylalkohol nach dem beschriebenen Verfahren auf die Nanoantennen aufgebracht. Ein Eindringen von Glucose verdrängt in diesem Fall die Bin-

dungen zum Polyvinylalkohol. Dadurch lockert sich die Verknüpfung der einzelnen Polymerschichten und erlaubt wiederum das Anschwellen des Hydrogels.

Um die einzelnen Schritte zu überwachen, wurde die Resonanz der Nanoantennen nach jeder Änderung vermessen. Eine sehr starke Verschiebung der Resonanz nach dem Aufwachsen der Polymerschichten legt einen erfolgreichen Herstellungsprozess nahe. Ebenso mit den Erwartungen vereinbar ist die anschließende Verschiebung zurück zu kürzeren Wellenlängen, wenn das Polymer im Wasser quillt. Dies ist auf den höheren Brechungsindex des trockenen Polymers im Vergleich zu Wasser zurückzuführen. Der Nachweis einer Reaktion auf Glucose geht aus den Messungen jedoch nicht hervor. Neben den allgemeinen Schwierigkeiten bei der Einführung eines chemischen Prozesses in einer neuen Umgebung, sind die Gründe unter Umständen auch in der Zusammensetzung dieses speziellen Hydrogels zu suchen. Untersuchungen anderer Gruppen mit ähnlichen Hydrogelen zeigen ein Anschwellen des Polymers um 165 % beim Eintauchen in Wasser. Dies hat zur Folge, dass das Polymer bereits im Ausgangszustand sehr verdünnt ist und ein weiteres Anschwellen bei Kontakt mit Glucose zu keiner nennenswerter Brechungsindexänderung mehr führt. Abhilfe schüfe hier die Entwicklung eines optimierten Hydrogels für den speziellen Einsatzzweck.

Wie in den vorangegangenen Experimenten deutlich wurde, ist die Funktionalisierung ein unverzichtbarer Bestandteil vieler Sensoren. Trotz der fundamentalen Notwendigkeit ist sie jedoch oft auch ein komplexes und aufwendiges Element. Daher wurde alternativ die Anwendbarkeit von oberflächenverstärkter Infrarotabsorptionsspektroskopie auf wässrige Glucoselösungen untersucht. Der Vorteil besteht dabei in der direkten Identifizierung der Substanzen über ihre Vibrationsspektren. Im Vergleich zu den bisherigen Untersuchungen setzt man hierbei nicht auf eine Verschiebung der plasmonischen Resonanz sondern ihre Überlagerung mit der molekularen Absorption.

Die durchgeführten Messungen offenbarten, dass der Nachweis ähnlicher Konzentrationen wie bisher verwendet nicht

möglich war. Um das zu erwartende Signal im Falle wässriger Glucoselösungen abschätzen zu können, haben wir daher einen Vergleich mit erfolgreichen Messungen anderer Stoffe angestellt. Dazu wurde das Volumen und die Anzahl an Molekülen einer selbstorganisierten Monolage Octadecanithiol auf der Oberfläche einer entsprechenden Nanoantenne abgeschätzt. Anschließend wurde die Anzahl von Glucosemolekülen in einer 100 mmol/l Lösung desselben Volumens berechnet. Unter Berücksichtigung der unterschiedlichen Bindungen lässt sich daraus ein etwa zwei Größenordnungen geringeres Signal ableiten. Als Ansatz zur Verbesserung des Systems bieten sich zwei Möglichkeiten an: Eine Funktionalisierung welche die Glucosemoleküle in den Bereichen mit der größten Feldüberhöhung akkumuliert, sowie eine Kombination mit Hydrogel.

Im letzten Teil der Arbeit wird das Konzept nichtlinearer plasmonischer Sensorik vorgestellt. Basierend auf der Erzeugung der dritten Harmonischen der einfallenden Wellenlänge. Durch den nichtlinearen Konversionsprozess beobachten wir eine höhere Sensitivität für lokale Änderungen des Brechungsindex in der Umgebung der Nanoantennen. In der linearen Sensorik fällt Licht der Frequenz ω auf die Nanoantennen und die transmittierte oder absorbierte Intensität bei eben dieser Frequenz dient als Sensorsignal. Verschiebt sich die plasmonische Resonanz der Antennen macht sich dies als Änderung der Intensität bemerkbar. In der nichtlinearen Sensorik wird ebenfalls Licht der Frequenz ω eingestrahlt. Als Sensorsignal jedoch wird die durch einen nichtlinearen Prozess erzeugte Intensität von Licht der dreifachen Frequenz detektiert.

Aufbauend auf dem Lorentz Oszillator Modell lässt sich dieser Prozess modellieren. Aufgrund der hohen elektromagnetischen Felder ist jedoch die Annahme eines harmonischen Potentials für die oszillierenden Elektronen nicht mehr gerechtfertigt. Deshalb erweitern wir die entsprechenden Gleichungen um eine kleine Störung dritter Ordnung. Daraus lassen sich Ausdrücke für die spektrale Form der Absorption der Nanoantennenfelder und die durch sie erzeugte Intensität bei der dritten Harmonischen des einfallenden Lichts ableiten. Die Analyse des Modells ergibt den von einem nichtlinearen Prozess

dritter Ordnung zu erwartenden Faktor 3 für die Verstärkung des Signals. Weiterhin erlaubt das Modell eine Vorhersage der Auswirkungen von Transmissionsmessungen anstelle von Absorptionsmessungen.

Um das Verhalten der Nanoantennenfelder im Hinblick auf Sensorik zu untersuchen, arbeiten wir mit linearer und nichtlinearer Spektroskopie. Im Falle Letzterer verwenden wir ultrakurze Laserpulse mit einer Dauer von 30 fs und einer durchstimmbaren Zentralwellenlänge zwischen 910 nm und 1120 nm. Unter Zuhilfenahme der entwickelten mikrofluidischen Sensorzelle wurden nach und nach Spektren für Messlösungen mit zwei verschiedenen Brechungsindizes aufgenommen. Die Auswertung der Spektren stimmt mit dem modellierten Verhalten überein und zeigt bereits die erhöhte Sensitivität im nichtlinearen Fall. Außerdem kann anhand der Spektren eine Wellenlänge mit maximaler Sensitivität für die lineare und nichtlineare Sensorkonfiguration bestimmt werden. An dieser spektralen Position werden anschließend beide Methoden in kontinuierlichen Messungen verschiedener Messlösungen verglichen. Im Sinne eines sorgfältigen Vergleichs werden dazu lineare und nichtlineare Signale simultan gemessen. Diese Messungen bestätigen die wesentlich höheren relativen Signaländerungen bei der Verwendung des nichtlinearen Messprinzips. Bei genauer Betrachtung lässt sich ein zum linearen Signal äquivalentes Signal-Rausch-Verhältnis feststellen. Folglich lassen sich lineare und nichtlineare Prozesse zwar gleichwertig verwenden, eine tatsächliche Verstärkung bleibt aber Systemen vorbehalten bei denen der Analyt einen fundamentalen Einfluss auf die nichtlinearen Effekte hat.

Zusammenfassend fällt vor allem die enorme Verstärkung des Signals durch das Hydrogel auf. Diese übertrifft die durch Verwendung der gekoppelten Struktur erzielbaren Effekte bei Weitem. Gemeinsam mit seiner Spezifität und dem zusätzlichen Vorteil Proteine zu filtern, ist es hervorragend für den Einsatz mit wässrigen Analyselösungen geeignet. Zukünftige Entwicklungen speziell für diesen Zweck optimierter Hydrogele können diese Vorteile noch verstärken. So lässt sich zum Beispiel durch den Einsatz von Polymeren mit hohem Brechungs-

index die detektierbare Differenz beim Anschwellen noch erhöhen.

Weiterhin geht aus den durchgeführten Untersuchungen hervor, dass die Kopplung in plasmonischen Systemen empfindlich vom Abstand und der Position der einzelnen Antennen abhängt. Gelingt es diese geometrischen Parameter durch das Anschwellen des Hydrogels zu beeinflussen, hat dies wesentliche Änderungen der optischen Eigenschaften solcher Systeme zur Folge. Daraus ergibt sich eine interessante Perspektive zur weiteren Optimierung der in dieser Arbeit untersuchten Sensorkonzepte.

INTRODUCTION

From an everyday perspective, the interaction of light with noble metals may at a first glance not seem to provide much more than a nice and shiny surface. Taking a closer look can yet reveal a variety of interesting phenomena. Many of them are related to collective oscillations of the quasi-free conduction electron plasma with respect to the fixed ionic background – called plasmons – excited by the impinging electromagnetic waves. In particular if the size of the metallic particle is smaller than the wavelength of the incident light. Already back in 1857 Michael Faraday published his results of a thorough experimental investigation of the relation of gold and other metals to light [1]. Besides beaten gold-leaves he studied films and particles of gold reduced from its solution and the arising colorful effects. Another important observation was made by Robert Wood in 1902. When investigating visible light reflected from metallic gratings, he found anomalous intensity drops in the spectra [2]. Theoretical work on the description of the grating effects was contributed a few years later by Lord Rayleigh [3]. At about the same time, J. C. Maxwell Garnett studied the working principle of nanoparticle doped colored glasses [4]. Only a few years later, Gustav Mie improved the description with his analytical solutions for light scattering from small spherical particles of arbitrary materials [5]. It was later generalized for elliptical particles by R. Gans [6]. Experiments at the time involved, e. g., the investigation of the color change when drying mixtures of gold colloids and gelatine, conducted by R. Zsigmondy [7].

Today a range of modern techniques for nanofabrication, simulation and spectroscopy is available, allowing to manufacture and investigate nanostructures with shapes and spatial configurations at will. Those nearly limitless possibilities have inspired people to extensively research phenomena related to the interaction of light with objects on the nanometer scale,

which has led to the development of a variety of applications. Most of them exploiting the strong confinement of energy to sub-wavelength volumes by such particles.

One area of interest is based on the ability to consciously manipulate the optical properties of materials. Careful design of the structures can lead to characteristics that do naturally not even occur. The most familiar example is a material with a negative refractive index. Effects of simultaneously negative values of the dielectric permittivity and magnetic permeability have been described theoretically by Veselago in 1964 [8]. Experimental realizations were first successful in the microwave regime and later also in the optical wavelength range [9, 10]. The availability of such materials, can have impact on the guidance of light with lenses and ultrahigh resolution, or enable the fascinating technique of optical cloaking [11–15].

In contrast to the effective material approach, plasmonic particles are also used to locally influence propagation of light on the nanoscale. Coupled to either molecular emitters or quantum dots, they can enhance as well as direct the light propagating into the far field [16–18]. Additionally, tunable beam steering and plasmonic waveguides are investigated to operate e.g., as optical interconnects [19–22]. Further research is done on the interplay between chiral light and arrangements of coupled particles [23–25].

The strong fields involved with plasmonics have also led to studies in the realm of nonlinear optics, where high intensities are necessary to enable the observation of nonlinear effects. Here, plasmonic structures are used to enhance or enable the creation of light at higher harmonic frequencies [26–30]. In a very recent example, plasmonic particles are employed to enhance the conversion efficiency of solar cells [31–34].

Besides the number of applications listed above, one of the most prominent areas for the use of plasmonic effects is related to sensor systems. Already prior to using localized surface plasmon resonances (LSPRs) of nanoparticles, electron oscillations on metal dielectric interfaces – called surface plasmon resonances – have been extensively studied and entered laboratories around the world. On the one hand, appropri-

ately designed structures can lead to improved signals in surface enhanced infrared absorption (SEIRA) or surface enhanced Raman scattering [35,36]. On the other hand they can act as highly sensitive transducers themselves. This allows to reach the ultimate limit of detecting a single protein without the need of previous labeling, such as, e.g., in fluorescence based approaches [37,38].

Typically LSPR sensors rely on a spectral shift of the resonance upon a change in the refractive index of the surrounding medium. The high sensitivity to those changes originates from the strong field confinement, and many different structures have been investigated seeking for an optimal geometry. However, the response on refractive index variations, without the ability to distinguish between different sources of such a change, leads to the necessity to functionalize the sensors to detect a particular desired analyte. The research presented in this thesis will cover the part of the plasmonic structure, the functionalization, as well as the novel concept of nonlinear plasmonic sensing.

In chapter 2 we will introduce the fundamental concepts and equations needed to discuss the interaction of electromagnetic waves with metallic nanoparticles. Additionally, the basic principles of nonlinear optics will be explained. Chapter 3 will briefly summarize the methods used for the realization of the experiments. Those include electron beam lithography (EBL), optical lithography, and silicone casting for fabrication of nanostructures and microfluidic cells. The experimental setup for Fourier-transform infrared (FTIR) spectroscopy and nonlinear spectroscopy is described as well as the techniques used for simulations. As we focus on liquid analyte solutions, chapter 4 is devoted to the microfluidic sensor cell used in all our experiments. The general requirements, as well as issues which arose during the experiments and influenced the development of the final cell will be discussed. Chapter 5 will focus on the analysis of a complex coupled plasmonic structure in order to understand the fundamental origin of the sensitivity of a plasmonic nanostructure in sensing applications. Full wave simulations and perturbation theory are used to relate the local

field around the structure to its sensitivity in different sensing schemes, and allows us to determine the optimal geometry for a particular case. Subsequently, Chapter 6 will deal with functionalization of LSPR sensors. As mentioned above, functionalization for a specific analyte is a crucial point in plasmonic sensing. This chapter discusses in detail the approach to coat gold nanoantennas with a thin layer of a boronic acid functionalized hydrogel, which reversibly swells in the presence of glucose. It will cover the fabrication of the sensor, the response to glucose concentrations in the physiological range, influences of other substances and the filtering capabilities of the hydrogel for proteins in the analyte solution. In addition, a layer-by-layer technique will be tested to obtain ultrathin hydrogel films. Seeking for a possibility to entirely avoid the often complex step of functionalization, a sensor system based on SEIRA will be explored in chapter 7. Chapter 8 finally introduces the concept of nonlinear plasmonic sensing, relying on third harmonic generation from plasmonic nanoantennas. An anharmonic oscillator model is developed to describe the behavior of the system, which is subsequently verified by nonlinear spectroscopy. Simultaneous detection of linear and nonlinear signal allows quantitative comparison of both methods and will provide further insight into the working principle.



BASIC EQUATIONS AND FUNDAMENTAL PRINCIPLES

2.1 BASICS OF ELECTRODYNAMICS

2.1.1 *Maxwell's Equations*

The classical description of electromagnetic phenomena, including optics, is founded on Maxwell's equations. Those equations are derived by combining the work of Gauss, Faraday, and Ampère with Maxwell's extension: the displacement current. The macroscopic equations in their differential form are expressed as [39]

$$\nabla \cdot \mathbf{D} = \rho \quad (2.1)$$

$$\nabla \times \mathbf{E} + \frac{\partial}{\partial t} \mathbf{B} = 0 \quad (2.2)$$

$$\nabla \cdot \mathbf{B} = 0 \quad (2.3)$$

$$\nabla \times \mathbf{H} - \frac{\partial}{\partial t} \mathbf{D} = \mathbf{J} \quad (2.4)$$

with the four vector fields \mathbf{E} , \mathbf{H} , \mathbf{D} , and \mathbf{B} denoting the electric and magnetic field, the dielectric displacement, and the magnetic flux density, respectively. \mathbf{J} is the current density and ρ the electric charge density. Material properties enter through additional equations which link the above fields via polarization \mathbf{P} and magnetization \mathbf{M} :

$$\begin{aligned} \mathbf{D} &= \varepsilon_0 \mathbf{E} + \mathbf{P} \\ \mathbf{B} &= \mu_0 (\mathbf{H} + \mathbf{M}) \end{aligned} \quad (2.5)$$

with the electric permittivity ε_0 and the magnetic permeability μ_0 of the vacuum. In linear, isotropic media those can be written as [40]

$$\begin{aligned}\mathbf{D} &= \varepsilon_0 \varepsilon \mathbf{E} \\ \mathbf{B} &= \mu_0 \mu \mathbf{H}\end{aligned}\tag{2.6}$$

with scalar values for the dielectric constant or relative permittivity ε and the relative permeability μ . For the materials and frequency ranges treated in the following \mathbf{M} can be neglected and $\mu = 1$. The linear relationship between \mathbf{E} and \mathbf{D} can also be expressed by

$$\mathbf{P}(\mathbf{r}, \omega) = \varepsilon_0 \chi_e(\mathbf{r}, \omega) \mathbf{E}(\mathbf{r}, \omega)\tag{2.7}$$

introducing the electric susceptibility $\chi_e(\mathbf{r}, \omega)$. By combining eqs. 2.5 to 2.7 under the assumption of homogeneous media χ can be related to the relative permittivity

$$\varepsilon(\omega) = 1 + \chi_e(\omega).\tag{2.8}$$

To describe the propagation of electromagnetic waves in media, a rotation is applied to eq. 2.2. Assuming $\mathbf{J} = 0$ and $\rho = 0$ together with eq. 2.1, eq. 2.4 and eq. 2.6 the wave equation for insulating, uncharged media is obtained:¹

$$\Delta \mathbf{E} = \varepsilon_0 \mu_0 \varepsilon \mu \frac{\partial^2 \mathbf{E}}{\partial t^2} = \frac{\tilde{n}^2}{c^2} \frac{\partial^2 \mathbf{E}}{\partial t^2}\tag{2.9}$$

with the speed of light in vacuum

$$c = \frac{1}{\sqrt{\varepsilon_0 \mu_0}}\tag{2.10}$$

and the refractive index

$$\tilde{n} = \sqrt{\varepsilon \mu}.\tag{2.11}$$

An important solution of eq. 2.9 is the plane wave

$$\mathbf{E}(z, t) = \mathbf{E}_0 e^{i(kz - \omega t)},\tag{2.12}$$

¹ exploiting $\nabla \times \nabla \times \mathbf{E} = \nabla(\nabla \cdot \mathbf{E}) - \Delta \mathbf{E}$

propagating in z -direction here, with the wavenumber k

$$k = \frac{\tilde{n}\omega}{c}. \quad (2.13)$$

It is worth to note that $\tilde{n} = n + i\kappa$ can, in general, be a complex value and frequency dependent. Furthermore, the phase velocity in the medium is given by $v = c/n$.

2.1.2 The Lorentz Oscillator Model

To understand the interaction of electromagnetic waves with matter, it is essential to particularly describe the interaction of the fields with the electrons of the medium. Although this relation can be arbitrarily complex in reality, many phenomena can be successfully explained by a rather simple, yet universal, classical model. Here, the electrons are bound to the core by a harmonic potential

$$V(x) = \frac{1}{2}m_e\omega_0^2x^2 \quad (2.14)$$

and are forced to oscillate by the external field. The displacement of an electron from the equilibrium position $\mathbf{x}(t)$ can therefore be captured in the differential equation

$$\ddot{\mathbf{x}}(t) + 2\gamma\dot{\mathbf{x}}(t) + \omega_0^2\mathbf{x}(t) = -\frac{e}{m_e}\mathbf{E}(t) \quad (2.15)$$

with the damping constant γ , the resonance frequency ω_0 , the effective mass of the electron m_e , the elementary charge e and the external electric field $\mathbf{E}(t)$.

The solution of eq. 2.15 can be obtained in the frequency domain:

$$\mathbf{x}(\omega) = \frac{e}{m_e} \frac{1}{\omega^2 - \omega_0^2 + 2i\gamma\omega} \mathbf{E}(\omega) \quad (2.16)$$

The displacement of the electron results in an electric dipole moment $\mathbf{p} = -e\mathbf{x}$. Assuming the single dipole moments are independent, they sum up to a macroscopic polarization $\mathbf{P} =$

$-en_e\mathbf{x}$, where n_e is the density of the contributing electrons. Using eq. 2.7 yields for the electric susceptibility $\chi_e(\omega)$:

$$\chi_e(\omega) = -\frac{e^2 n_e}{\epsilon_0 m_e} \frac{1}{\omega^2 - \omega_0^2 + 2i\gamma\omega} \quad (2.17)$$

As the complex refractive index \tilde{n} is related to the electric susceptibility via the electric permittivity

$$\begin{aligned} \tilde{n}(\omega) &= n + ik = \sqrt{\epsilon(\omega)} \\ &= \sqrt{1 + \chi_e(\omega)} \approx 1 + \frac{1}{2}\chi_e(\omega), \end{aligned} \quad (2.18)$$

its real part $n(\omega)$ and imaginary part $\kappa(\omega)$ can be derived from eq. 2.17 to be [41]:

$$n(\omega) = 1 - \frac{1}{2} \frac{e^2 n_e}{\epsilon_0 m_e} \frac{\omega^2 - \omega_0^2}{(\omega^2 - \omega_0^2)^2 + 4\gamma^2 \omega^2} \quad (2.19)$$

$$\kappa(\omega) = \frac{e^2 n_e}{\epsilon_0 m_e} \frac{\gamma\omega}{(\omega^2 - \omega_0^2)^2 + 4\gamma^2 \omega^2} \quad (2.20)$$

The evolution of n and κ in the vicinity of a resonance is depicted in Fig. 2.1. A deeper understanding can be gained by again considering a plane wave in a medium (eqs. 2.12 and 2.13), here in the stationary case:

$$\mathbf{E}(z) = \mathbf{E}_0 e^{ikz} = \mathbf{E}_0 e^{i\left(\frac{\tilde{n}\omega}{c}z\right)} = \mathbf{E}_0 e^{i\frac{\omega}{c/n}z} e^{-\frac{\kappa\omega}{c}z} \quad (2.21)$$

From this equation it can be seen that the increasing imaginary part of the refractive index $\kappa(\omega)$ at the resonance leads to an attenuation of the amplitude. The real part $n(\omega)$ of the refractive index, in contrast, changes the phase velocity $v = c/n$. It additionally introduces a frequency dependence to the phase velocity, which leads to the phenomenon of dispersion. For frequencies below and above the resonance n increases with the frequency and hence v decreases (region I and III in Fig. 2.1). This is the common case in many materials at optical frequencies and is thus named normal dispersion. Around the resonance, however, the trend is inverse and the behavior is called anomalous dispersion (region II).

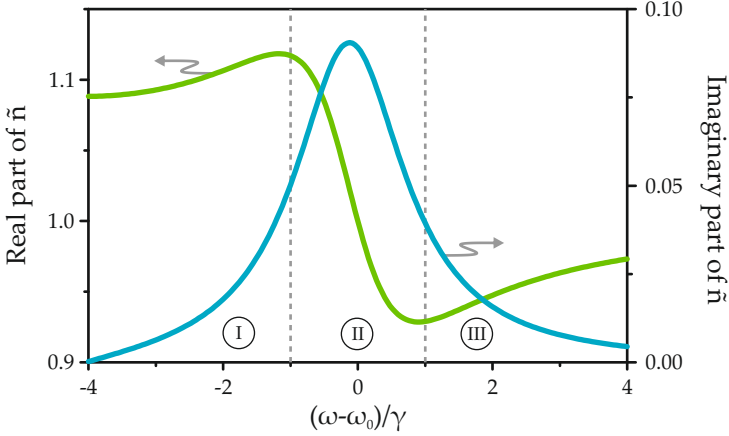


FIGURE 2.1: Real and imaginary part of the complex refractive index derived from the Lorentz oscillator model. The increasing imaginary part leads to an attenuation of the amplitude at the resonance. The real part is related to the phase velocity and leads to the phenomenon of anomalous dispersion around the resonance (region II).

2.1.3 Optical Properties of Noble Metals

The optical properties of noble metals are dominated by the quasi-free electrons in the conduction band. The behavior of those electrons can be described in analogy to the Lorentz oscillator model by a differential equation similar to eq. 2.15. They oscillate when excited by an external electromagnetic wave and are damped because of collisions occurring at a phenomenological damping frequency γ_D . Yet, as no restoring force is present in this case (corresponding to $\omega_0 = 0$ in eq. 2.15), the equation simplifies to [40]

$$\ddot{\mathbf{x}}(t) + \gamma_D \dot{\mathbf{x}}(t) = -\frac{e}{m_e} \mathbf{E}(t) \quad (2.22)$$

Solving the modified equation leads to the electric susceptibility

$$\chi_e(\omega) = -\frac{\omega_p^2}{\omega^2 - i\gamma_D\omega} \quad (2.23)$$

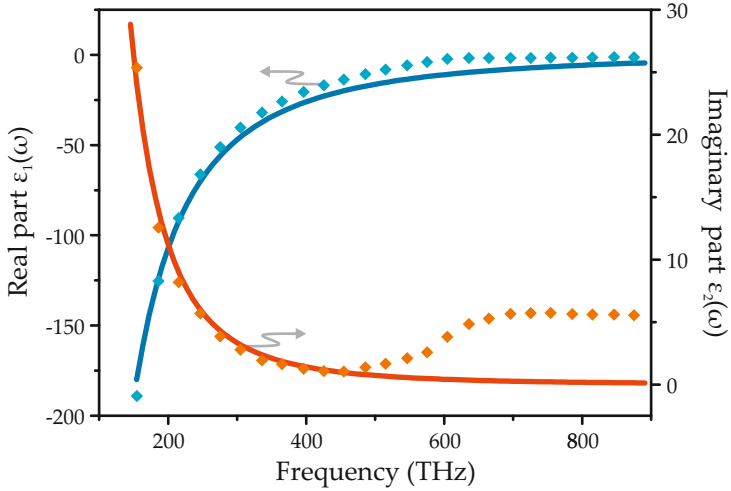


FIGURE 2.2: Experimental data (diamonds) for the dielectric permittivity of gold measured by Johnson and Christy [42]. Solid lines correspond to a fit with $\omega_p = 2079$ THz and $\gamma_D = 21$ THz of the Drude model.

where the plasma frequency ω_p has been introduced as

$$\omega_p = \sqrt{\frac{e^2 n_e}{\epsilon_0 m_e}}. \quad (2.24)$$

Again, the real and imaginary part of the refractive index or the dielectric permittivity, respectively, can be deduced from eq. 2.23:

$$\epsilon(\omega) = \epsilon_1(\omega) + i\epsilon_2(\omega) = 1 - \frac{\omega_p^2}{\omega^2 + \gamma_D^2} + i \frac{\gamma_D \omega_p^2}{\omega^3 + \gamma_D^2 \omega}. \quad (2.25)$$

The fit of the Drude model to experimental data obtained for gold by Johnson and Christy [42] yields $\omega_p = 2079$ THz and $\gamma_D = 21$ THz. Fig. 2.2 shows that the model can describe the behavior of the metal quite well. At least in the near-infrared regime. Yet, there is an obvious discrepancy for higher frequencies. This can be attributed to the occurrence of inter-

band transitions in gold, which are not considered in the model at all.

For $\omega \gg \gamma_D$ and $\omega < \omega_p$, which is the case for gold in the visible range of the spectrum, the real part of the dielectric permittivity ε_1 is negative, while the imaginary part ε_2 is comparably small. Therefore, the refractive index according to eq. 2.18 will be mainly imaginary. This allows no propagation of electromagnetic waves in the medium, and an incident plane wave will be reflected at the metal surface. This is the origin of the typical metallic gloss.

Taking a look at frequencies $\omega > \omega_p$, the real part of ε gets positive and the metal behaves like a lossy dielectric. However, this is the region where interband transitions alter the behavior of the realistic material.

2.2 LOCALIZED SURFACE PLASMON RESONANCES

After discussing the properties of bulk noble metals in the previous section, we now want to take a closer look on the behavior of nanoparticles, as the finite dimensions strongly affect their properties. In the most simple approach, we can treat the interaction of a spheric particle with an electromagnetic field in a quasi-static approximation, if its radius a is much smaller than the wavelength of the incident light. This implies that the field can be regarded as constant over the particle volume and the time dependence can be added after a solution for the field distribution is obtained. The task is now to solve the Laplace equation

$$\nabla^2 \Phi = 0 \quad (2.26)$$

for the homogeneous, isotropic particle described by its dielectric function $\varepsilon_1(\omega)$ and a surrounding likewise isotropic, non-absorptive medium with $\varepsilon_2(\omega)$ in a static electric field along z -direction $\mathbf{E} = E_0 \hat{\mathbf{z}}$. This leads to [39, 40]

$$\begin{aligned} \Phi_{\text{in}} &= -\frac{3\varepsilon_2}{\varepsilon_1 + 2\varepsilon_2} E_0 r \cos \Theta \quad \text{and} \\ \Phi_{\text{out}} &= -E_0 r \cos \Theta + \frac{\varepsilon_1 - \varepsilon_2}{\varepsilon_1 + 2\varepsilon_2} E_0 a^3 \frac{\cos \Theta}{r^2}. \end{aligned} \quad (2.27)$$

Here, Φ_{in} and Φ_{out} represent the potentials inside and outside the particle, with Θ being the angle with respect to the electric field. Φ_{out} can be interpreted as a superposition of the applied field with the field of a dipole at the center of the sphere with a dipole moment

$$\mathbf{p} = 4\pi\epsilon_0\epsilon_2a^3 \frac{\epsilon_1 - \epsilon_2}{\epsilon_1 + 2\epsilon_2} \mathbf{E}. \quad (2.28)$$

With $\mathbf{p} = \epsilon_0\epsilon_2\alpha\mathbf{E}$ the polarizability α of the sphere can then be written as

$$\alpha = 4\pi a^3 \frac{\epsilon_1 - \epsilon_2}{\epsilon_1 + 2\epsilon_2}. \quad (2.29)$$

Apparently the polarizability exhibits a resonant behavior if in the denominator $|\epsilon_1 + 2\epsilon_2|$ exhibits a minimum. For the case of small or slowly varying $\Im(\epsilon_1)$ the condition simplifies to

$$\Re(\epsilon_1) = -2\epsilon_2. \quad (2.30)$$

It is called the Fröhlich condition and can be fulfilled for metallic particles. The resonance, arising due to a collective excitation of electron oscillations inside the particle, is named a localized surface plasmon resonance (LSPR) and goes along with enhanced fields inside and in close proximity of the particle [40]. Equation 2.30 also discloses the strong influence of the surrounding medium, which is the basis for the sensing applications discussed in the remaining chapters.

2.3 NONLINEAR OPTICS

2.3.1 *Nonlinear Polarization and Susceptibility*

One of the fundamental assumptions that was made at the beginning of this chapter is the linear relation between the polarization \mathbf{P} and the electric field \mathbf{E} (cf. eq. 2.7). However, when optical electromagnetic waves with high intensities are applied to a material, new phenomena occur where the material response depends in a nonlinear manner on the incident intensity. These

effects can often be described by expressing the polarization as a power series in the field strength [43]:

$$\mathbf{P}(t) = \underbrace{\varepsilon_0\chi^{(1)}\mathbf{E}(t)}_{\mathbf{P}_L(t)} + \underbrace{\varepsilon_0\chi^{(2)}\mathbf{E}(t)^2 + \varepsilon_0\chi^{(3)}\mathbf{E}(t)^3 + \dots}_{\mathbf{P}_{NL}(t)} \quad (2.31)$$

where \mathbf{P}_L corresponds to the linear polarization and describes the linear optical effects discussed before. All other terms that are of higher order in \mathbf{E} are summarized in the nonlinear polarization \mathbf{P}_{NL} with the respective n^{th} order susceptibilities $\chi^{(n)}$. Expressing the polarization in the time domain instead of frequency domain in the given manner is valid for an instantaneous response of the medium to the electric field, which also implies that the medium is lossless and dispersionless.

2.3.2 Nonlinear Processes of Second Order

To discuss nonlinear optical processes arising from the nonlinear polarization of second order

$$\mathbf{P}^{(2)}(t) = \varepsilon_0\chi^{(2)}\mathbf{E}(t)^2 \quad (2.32)$$

an optical field consisting of two frequency components ω_1 and ω_2 is considered:

$$\mathbf{E}(t) = \mathbf{E}_1e^{-i\omega_1t} + \mathbf{E}_2e^{-i\omega_2t} + \text{c.c.} \quad (2.33)$$

Calculating $\mathbf{E}(t)^2$ leads to

$$\begin{aligned} \mathbf{E}(t)^2 &= 2(\mathbf{E}_1\mathbf{E}_1^* + \mathbf{E}_2\mathbf{E}_2^*) && \text{(OR)} \\ &+ \mathbf{E}_1^2e^{-2i\omega_1t} + \mathbf{E}_2^2e^{-2i\omega_2t} && \text{(SHG)} \\ &+ 2\mathbf{E}_1\mathbf{E}_2e^{-i(\omega_1+\omega_2)t} && \text{(SFG)} \\ &+ 2\mathbf{E}_1\mathbf{E}_2^*e^{-i(\omega_1-\omega_2)t} && \text{(DFG)} \\ &+ \text{c.c.} && \end{aligned} \quad (2.34)$$

It can be seen that $\mathbf{E}(t)^2$ consists of several terms oscillating at different frequencies. The first term leads to a process known as optical rectification (OR), which creates a static electric field

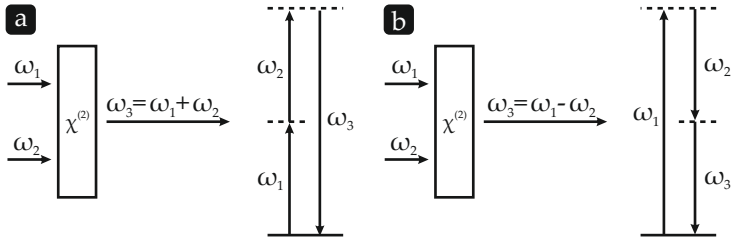


FIGURE 2.3: Schematic picture of second order nonlinear processes. (a) Two photons are destroyed and a photon with their combined energy is created. (b) One photon is destroyed and two photons with lower energies are created.

across the nonlinear medium. The second term contributes radiation at the second-harmonic frequencies $2\omega_1$ and $2\omega_2$. The corresponding process is therefore known as second harmonic generation (SHG). A common use of SHG is the conversion of fixed-frequency lasers to a different spectral region [43].

The process of sum frequency generation (SFG) is similar to that of SHG, except for the fact that two different frequencies are involved, and generates radiation at $\omega_1 + \omega_2$. The last contribution in eq. 2.34 relates to difference frequency generation (DFG), which corresponds to light at frequency $\omega_1 - \omega_2$.

Those effects can be visualized in the picture of photons being destroyed or created in the nonlinear medium in a single quantum-mechanical process. For SHG and SFG respectively, two photons of the same frequency or one photon of both involved frequencies are destroyed and a photon with their combined energy is created. Even though DFG appears to be a very similar process, there is an important difference. As a photon at the difference frequency $\omega_1 - \omega_2$ corresponds to a lower energy, conservation of energy requires an additional photon at frequency ω_2 to be created. Therefore, the low frequency field is amplified and the process is also known as optical parametric amplification [43].

Up to now, only the electric field entering eq. 2.32 has been investigated. Closer examination of $\chi^{(2)}$ yet reveals that non-

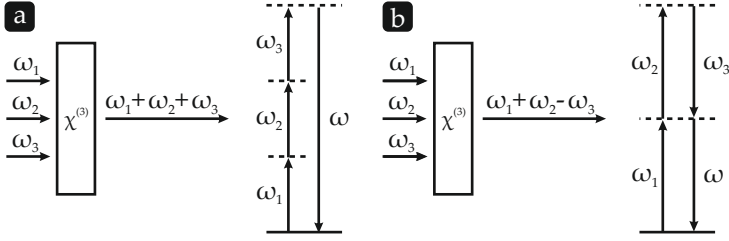


FIGURE 2.4: Schematic picture of third order nonlinear processes. (a) Three photons are destroyed to create one photon with their combined energy. (b) Various combinations involving four photons are possible and lead to different nonlinear effects.

linear processes of second order do only occur in media that possess a lacking inversion symmetry [43].

2.3.3 Nonlinear Processes of Third Order

As a last point in this section, the general effects of the nonlinear polarization of third order

$$\mathbf{P}^{(3)}(t) = \varepsilon_0 \chi^{(3)} \mathbf{E}(t)^3 \quad (2.35)$$

are considered. In the general case of third order nonlinear effects, four photons with up to four different frequencies are involved and the corresponding processes are called four wave mixing (FWM). Calculating $E(t)^3$ under those circumstances is quite complicated as there will be contributions from all possible combinations of the incident frequencies according to $\omega_4 = \pm\omega_1 \pm \omega_2 \pm \omega_3$. Therefore, the simple case of a monochromatic field $E(t) = E_1 e^{-i\omega_1 t}$ will be given in the following:

$$\mathbf{E}(t)^3 = \frac{1}{4} \mathbf{E}_1^3 e^{-i3\omega_1 t} + \frac{3}{4} |\mathbf{E}_1|^2 \mathbf{E}_1 e^{-i\omega_1 t} + \text{c.c.} \quad (2.36)$$

The first term in this equation is related to a contribution at the frequency 3ω and the process is hence named third harmonic generation (THG). In the microscopic visualization introduced above, it corresponds to three photons at frequency ω being

destroyed and, in exchange, one photon of frequency 3ω being created.

The second term in eq. 2.36 oscillates at the frequency of the incident field. It can be interpreted as an intensity dependent contribution to the refractive index at frequency ω . In consequence, interesting phenomena like spatial self focusing or self phase modulation can occur [43]. The latter can, for example, lead to significant spectral broadening of ultrashort laser pulses [44].



METHODS

3.1 SIMULATION

Simulations of the investigated nanostructures rely on numerically solving Maxwell's equations and were performed with two different tools. The first one, CST Microwave Studio, is a commercially available software package for electromagnetic analysis in the high frequency range [45]. The other one is an in-house implementation of a scattering matrix approach.

In CST Microwave Studio, the structures are modeled in a graphical front end and are subsequently subject to automated mesh generation by the program. The mesh is adaptively refined, as simulation accuracy depends strongly on the resolution and type of the mesh. A set of different solvers is available for various applications. While time domain solvers provide the highest flexibility, use of other solvers may be more efficient in a particular case. The time domain solver uses a hexahedral mesh and is based on the finite integration technique to solve Maxwell's equations in their integral form. The frequency domain solver is especially suited for structures that are much smaller than the shortest wavelength of interest and enables the use of a tetrahedral mesh, which can be beneficial to resolve small geometric details. Results, such as transmittance, reflectance, and absorption spectra, as well as electromagnetic field distributions, can afterwards be analyzed via the graphical interface or may be exported for further analysis.

The Fourier modal method is particularly suited for stacked layers with a periodic arrangement of structures. For the use of this method, a three-dimensional structure is separated into several layers, each homogeneous along its normal direction. Maxwell's equations are then rigorously solved for every layer by decomposing into Floquet-Bloch modes. The single layers are afterwards combined, considering the respective boundary

conditions, and a scattering matrix formalism is used to obtain the optical properties of the structure [46]. Inaccuracies in numerical calculations merely arise from the truncation of the number of involved modes. For large steps in the permittivity or permeability of the employed materials, these inaccuracies lead to poor convergence. To overcome those issues without dramatically increasing computation times, optimizations such as matched coordinates and adaptive spatial resolution have been introduced. [47,48]. Although finding the correct coordinate transformations for those techniques to be used with a given structure might in general be a time consuming task, they are well known for simple antenna geometries used in the following studies [49].

3.2 FABRICATION

3.2.1 *Electron Beam Lithography*

Working with plasmonic nanostructures requires to creation of structures with feature sizes down to several nanometers. Ideally, short processing time and complete freedom regarding materials, shape, or dimensions and arrangement of arrays are desirable, but might not always be compatible. A tool that satisfies most of these requirements is electron beam lithography (EBL). Here, a focused electron beam is scanned across a surface with a spot size of less than 10 nm. The beam can be blanked to restrict the electron exposure to desired areas. A structure is defined by coating the surface with an electron sensitive resist. The modifications induced in the resist by the electron exposure lead to a selective solubility in the subsequent development step. Consequently, a resist pattern is formed which can be transferred to the substrate or other materials by etching or deposition processes. Hence, this technique allows flexible and reproducible fabrication of almost arbitrary nanostructures. However, if large areas are to be processed, fabrication time becomes an issue as every single structure has to be written by the electron beam sequentially.

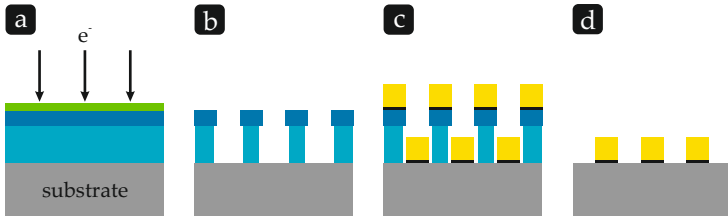


FIGURE 3.1: Electron beam lithography procedure with a positive tone resist. (a) Spin-coating of resist (blue) and, in case of non-conductive substrates, a conductive polymer (green) and subsequent electron beam exposure. (b) Development with a slight undercut. (c) Evaporation of a thin Cr adhesion layer and gold film. (d) Lift-off of residual resist and unnecessary gold.

Apart from the precise control over the electron beam, development of suitable resists and dedicated developers is a crucial point. In general two different types of resists are available. They are classified as positive tone when the exposure causes the resist to be removed, and negative tone when the exposed areas remain after development. Both usually consist of a resin dissolved in a solvent and, depending on the type of resist, a sensitizer. In positive resists, electron exposure splits long polymer chains and thus enables the removal by the developer. For negative resists, the electron exposure initiates a polymerization, leading to a stable compound that withstands the developer. Thus, they commonly provide better adhesion to the substrate, yet at the cost of the achievable resolution.

Samples for all our investigations were prepared using polymethylmethacrylate (PMMA) as a positive resist. Depending on the intended spectral range, either glass or CaF_2 slides with a size of $10\text{ mm} \times 10\text{ mm}$ and a thickness of 0.5 mm or 1 mm served as substrates. After cleaning with acetone and isopropanol in an ultrasonic bath for at least 15 min , PMMA with a molecular weight of 200 kDa was spin-coated followed by a soft bake. In a second spin-coating step, a thin layer of 950 kDa PMMA was applied and baked under the same conditions. Finally, the resist was covered by spin-coating a conductive polymer (cf. Fig. 3.1a). The structure was then defined through elec-

tron exposure, the conductive layer was removed and the pattern was developed using methyl isobutyl ketone. Because of different development rates, the two PMMA layers now exhibit a slight undercut, as illustrated in Fig. 3.1b, which is advantageous when later removing the resist. A 2 nm Cr adhesion layer was evaporated before the gold film in the intended thickness of the structures. A subsequent lift-off procedure in acetone or N-methylpyrrolidone removed the unexposed resist and thus the gold in the areas around the structures (Fig. 3.1c-d). To remove any residual PMMA, the samples were treated with oxygen plasma for several minutes and finally rinsed with acetone and isopropanol.

Multiple stacked layers of structures were achieved by spin-coating a polymer (PC-403) layer, to yield the desired vertical spacing, after the previous layer was completed. The polymer is highly cross-linked by heating and is not affected by the further processing steps. Merely the oxygen plasma cleaning step is omitted in this case. Proper alignment of the layers is ensured by fabricating markers together with the first layer that allow the EBL system to orientate its coordinate system for the new exposure, which is again carried out following the above recipe.

3.2.2 *Optical Lithography*

Conventional optical lithography utilizes UV light to expose a light-sensitive photoresist on a substrate, e. g., a silicon wafer. In contrast to EBL, where the pattern is created by raster scanning an electron beam across the surface, a whole pattern is defined at once by illumination through a previously created mask. Therefore, optical lithography allows for high throughput and large scale production. The mask is reusable and is commonly defined by EBL or laser lithography in a thin chromium layer on a quartz glass substrate. In the simplest case, the mask is brought in contact or close proximity to the substrate for exposure. However, direct contact increases the probability to damage either the mask or the substrate, while a gap between mask and substrate decreases the resolution sig-

nificantly. In production environments a practical alternative is to project an image of the mask onto the substrate. This method allows to expose even larger areas with the same pattern in so-called stepper systems, by stepwise moving the substrate and repeating the exposure. Invention of novel light sources and technologies such as immersion lithography enable fabrication of structures well below 100 nm [50]. The photoresist again changes its solubility in the respective developer upon exposure and enables transfer of the pattern through subsequent etching or deposition processes (cf. section 3.2.1).

The process used in this work is carried out with a mask aligner equipped with a mercury short-arc lamp and a microscope with infrared illumination. Depending on the required thickness, photoresists from the MicroChem SU-8 series were spin-coated on a 2 inch silicon wafer with varying speed. After removing the edge bead, a pre-bake was conducted according to the manual, allowing the substrate to cool down before continuing with the exposure. The mask and wafer were mounted in the mask aligner and brought into direct contact. Exposure was initiated (19.5 s for 5.5 μm resist thickness), and after completion and disassembly of mask and substrate, a post-exposure bake finished the chemical process. The structure was then developed in mr-Dev 600, rinsed, and dried. Optionally the durability of the structure was increased by a hard bake step at elevated temperatures.

3.2.3 *Silicone Casting*

Poly(dimethylsiloxane) (PDMS) is a versatile silicon-based organic polymer. It is optically transparent, chemically inert, non-toxic and non-flammable. Areas of application include food industry, medicine, cosmetics, and research. Depending on the exact compound, it can, for example, act as an anti-foaming agent, lubricant or elastomer [51–53]. The formulation used here, namely Sylgard[®]184 silicone elastomer kit, was originally developed to encapsulate electronic devices. It can be poured over arbitrary structures to form a rubber-like silicone material after hardening completely.

The procedure is started by mixing the base with a curing agent in a ratio of 10:1 to initiate the polymerization. For optical applications it can be essential to subsequently degas the mixture to avoid small air bubbles in the final product. For this purpose it can either be placed in a vacuum or alternatively in an ultrasonic bath for several minutes. To obtain a defined structure, the viscous compound is afterwards cast onto a previously fabricated mold. Curing can take place at room temperature for 48 h, but can be considerably accelerated by heating. For most of the structures 3 h at 70 °C was used. The elastomer is peeled off from the mold and further shaped by cutting or punching if necessary.

Critical applications may require the fabricated replica to be heated again to higher temperatures or to be soaked with an appropriate solvent. This step ensures no unpolymerized residue remains in the final product. Furthermore, despite its general chemical inertness, the PDMS elastomer responds to various solvents with a noticeable, yet reversible, swelling [54]. Exploiting this technique, several nanometer sized features have been demonstrated when fabricating stamps and molds for soft lithography [55,56].

3.3 MEASUREMENT

3.3.1 *Fourier Transform Infrared Spectroscopy*

An important aspect of the presented work is the determination and exploitation of optical properties of artificially fabricated materials. One of the main instruments used for spectroscopy is a Fourier-transform infrared (FTIR) spectrometer (Bruker VERTEX 80), extended by an infrared microscope (Bruker Hyperion 2000). Fourier spectroscopy is based on two beam interferometry using a Michelson interferometer. Light emitted by a source is collimated and subsequently split by a beam splitter. The two different beams are reflected on one fixed and one moving mirror and are afterwards recombined and guided to a detector. For a mirror moving with constant velocity, the difference of the two optical paths is now a linear function of the

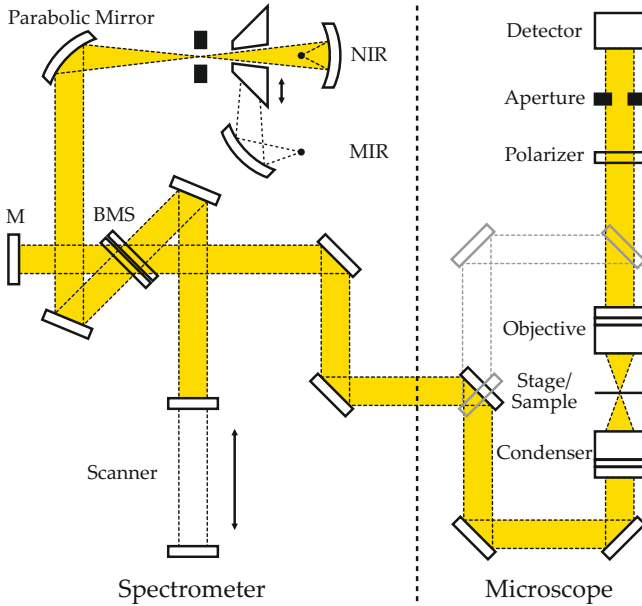


FIGURE 3.2: Schematic illustration of the Fourier-transform infrared spectrometer setup. The main part of the spectrometer is an interferometer consisting of an exchangeable beam splitter (BMS), a fixed mirror (M), and a mirror mounted on a linear scanner. Furthermore, it contains two switchable light sources (NIR/MIR) for different spectral regions. The beam is guided to a microscope for transmittance and reflectance measurements on small sample areas.

time. The intensity recorded at the detector over time leads to an interferogram that contains all information about the spectrum of the incident light. The spectrum itself can be obtained from the interferogram by a Fourier transformation [57].

Using FTIR spectroscopy has a variety of advantages. Besides a high spectral resolution the excellent signal-to-noise ratio and/or fast measurements are key points of this method. Furthermore, it is applicable in a wide spectral range by just adapting light source, beam splitter and detector.

In our setup, which is illustrated in Fig. 3.2 two light sources cover a range from 600 nm to 25 μm . Namely a tungsten lamp for the visible and near infrared region, and a silicon carbide Globar for the mid-infrared region. A scanner mirror with an air bearing allows to achieve a spectral resolution better than 0.07 cm^{-1} . Several detectors are available, including a silicon photodiode (400 nm to 1100 nm) and a liquid nitrogen cooled mercury cadmium telluride (MCT) detector (0.8 μm to 12 μm). They can be combined with two CaF_2 beam splitters (0.2 μm -2.5 μm and 0.7 μm -8.3 μm) and one KBr beamsplitter (2.5 μm -25 μm) with overlapping wavelength ranges. Other available optics are polarizers for all wavelength ranges as well as an assortment of quarter-wave and half-wave plates.

The microscope attached to the spectrometer is equipped with two identical 15 \times Cassegrain objectives for reflectance and transmittance measurements. Focusing and alignment is done with visible light and an attached CCD camera. Two knife-edge apertures in the beam path allow to limit the measurement to a rectangular area. A computer controlled x-y stage can be used for precise alignment and automation of measurement series.

3.3.2 *Centroid Evaluation of Spectral Resonance Features*

In many applications, including sensing with localized surface plasmon resonances (LSPRs), it is necessary to track even minute changes of spectral features. For simple Gaussian or Lorentzian shaped profiles, fitting of the respective analytical function and subsequent parameter extraction is a common and suitable method. If the shapes, however, deviate from those well known profiles because of, for example, experimental conditions, other algorithms could be more appropriate. Just relying on the position of a local extremum is not an option, as this is severely susceptible to noise and fluctuations.

To evaluate the shifts in our transmittance T spectra, we therefore use an algorithm similar to the method of Dahlin et al. [58]. Instead of just tracking the minimum T_{min} of the resonance, information from a larger spectral range is included by

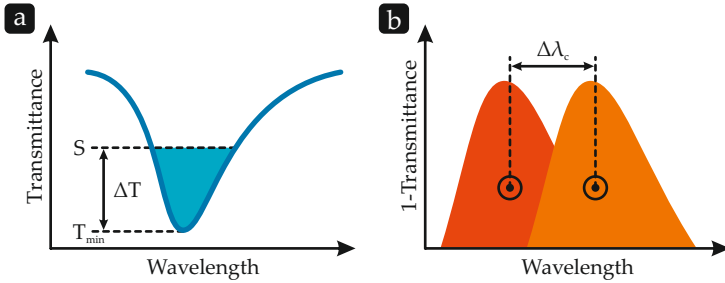


FIGURE 3.3: (a) For tracking small resonance shifts, the centroid of the blue area is calculated. It is defined by the curve and a threshold value S . (b) For the numerical evaluation, the spectra are cropped at the threshold value and inverted prior to calculation of the centroid.

calculating the centroid of an area enclosed by the resonance curve and a horizontal threshold S (cf. Fig. 3.3a). For this purpose we use $T' = 1 - T + S$, neglect all negative values and numerically evaluate the expression

$$\lambda_c = \frac{\int \lambda \cdot T' d\lambda}{\int T' d\lambda} \quad (3.1)$$

as illustrated in Fig. 3.3b. For asymmetric spectra, the centroid value does not coincide with the position of the maximum, yet both exhibit nearly perfect proportionality [58]. The threshold value S is set once per measurement series in a way that $\Delta T = S - T_{\min} \approx 0.1$ in absolute transmittance units. If the spectral feature does not only shift but also change its intensity, it may be appropriate to automatically calculate S for every single spectrum.

For noisier spectra, the method can be extended by fitting a high order (~ 20) polynomial to the spectrum prior to calculating the centroid, which additionally allows for analytical evaluation. Instead of the threshold value S , a wavelength span can also be used.

3.3.3 *Ultrashort Laser Pulses for Nonlinear Spectroscopy*

The study of nonlinear optical effects requires intense electromagnetic fields. Those are best realized in the form of ultrashort laser pulses. In this case, the enormous intensities are only reached for a very short time, yet enable measurements of nonlinear optical properties, while a still reasonable average power avoids excessive heating of the investigated samples.

The laser system used for the experiments in chapter 8 was explicitly built for nonlinear spectroscopy of plasmonic nanostructures by B. Metzger and allows for generation of widely tunable sub-20 fs Gaussian laser pulses [59].

A solid-state diode pumped solitary mode-locked Yb:KKG oscillator serves as the pump source [60]. It is able to emit 175 fs laser pulses at a wavelength of 1027 nm with a repetition rate of 44 MHz and an average output power of 2.4 W.

Subsequently, 10 cm of a photonic crystal fiber (LMA-8) are used to broaden the spectrum. In a standard fused silica step index fiber, the light is guided in a cylindrical fiber core with a slightly higher refractive index than the surrounding fiber cladding by total internal reflection. For high light intensities coupled into the fiber, various nonlinear effects can occur during the transmission [61]. This is particularly supported because of the strong confinement of the light to a small area in the fiber core and the long possible interaction length. The efficiency can be boosted by exploiting the possibility of precisely tailored optical properties in photonic crystal fibers [62]. Further enhancement could be achieved if the diameter of the fiber is tapered, increasing the confinement of the light to an even smaller area [63, 64]. Employing this particular photonic crystal fiber a broadband spectrum spanning 300 nm is generated.

Two equilateral SF₁₀ prisms are used to precompress the fiber output, yielding 21 fs pulses and a total power of 1.15 W. To eliminate higher orders of dispersion and to spectrally shape the pulses as desired, they are finally sent through a 4f pulse shaper.

As shaping of ultrashort laser pulses in the time domain is strongly limited, the modification is done in frequency domain. Therefore, the pulses are spectrally split in space using a grating, and the beam is collimated by a parabolic mirror. This leads to a beam with all different frequency components of the pulse traveling in parallel, which is guided onto two consecutive 640 pixel liquid crystal arrays. On transmission, those allow to independently modulate the amplitude and phase of the different frequency components. Different algorithms are available to obtain, for example, the phase that has to be applied to achieve Fourier-limited pulses. Afterwards, the pulses are transformed back by an arrangement of parabolic mirror and grating symmetric to the input stage.

The complete setup allows to generate nearly arbitrary spectra in the wavelength range between 900 nm and 1150 nm. Particularly, the realization of widely tunable Gaussian shaped ultrashort laser pulses is of great interest for nonlinear spectroscopy applications.



THE MICROFLUIDIC SENSOR CELL

Throughout the remaining chapters of this thesis we will study sensor systems based on plasmonic nanostructures. The focus will thereby lie on the investigation of aqueous analyte solutions. Therefore, a well designed system for handling liquids in combinations with our nanostructures and the optical components of our setups is of great importance and will place high demands especially on the sensor cell.

Prior to and at the beginning of this work, sensors cells at this institute were built around the $10\text{ mm} \times 10\text{ mm}$ glass substrates of the samples from microscope slides. Pieces of glass were put beneath and above the sample with various kinds of spacer and/or sealing material in between. Including, for example, additional glass slides, nickel foil or laboratory sealing film. The single slides were glued together with silicone glue or nail polish and injection needles were embedded, serving as inlet and outlet for the liquid. A picture of such a cell can be seen in Fig. 4.1. Even though this kind of cell can be sufficient for proof of principle measurements in some situations, it has a variety of disadvantages. The cell has to be built completely new for every sample and every measurement, as it has to be destroyed to retrieve the sample e. g., for cleaning. This is a very time consuming process and is not practical for frequent and extensive studies. Furthermore, the sample is insufficiently fixed in the cell, which leads to problems with repeatability and automated measurements. The liquid level above the sample is hard to define accurately and varies between measurements. Moreover, it is challenging to seal the cell tightly and with the top and bottom glass slides, the light has to pass four additional, partially reflecting, interfaces.

A promising approach to overcome those disadvantages was the introduction of poly(dimethylsiloxane) (PDMS) in the construction process of the sensor cell. This nontoxic silicone can

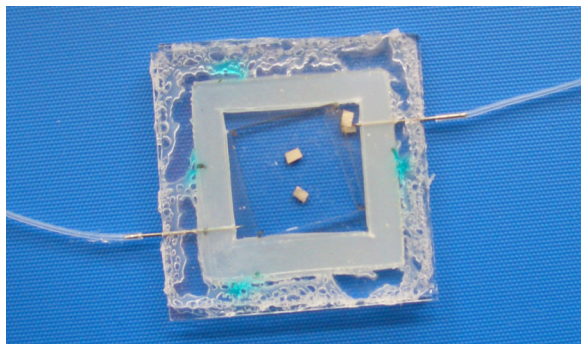


FIGURE 4.1: Picture of a sensor cell at an early stage. The cell is built around the sample using pieces of microscope slides. Apart from being leaky, it has several other disadvantages such as a poorly fixed sample and a vaguely defined analyte layer thickness.

be cast and hardened as described in section 3.2 to form structures with microscopic features. In its final state it is chemically inert and transparent from the visible spectral range up to a wavelength of about $2.5\ \mu\text{m}$. In microfluidic applications it is prevalently used and often bound to glass or silicon substrates by the help of oxygen plasma [65,66]. As the binding is, however, irreversible we do not consider this technique further but exploit the anyway good sealing capabilities of the rubber-like material. Another popular method, namely the fabrication of microfluidics from shrinking thermoplastic sheets, did mainly fail because of optical drawbacks and a missing possibility to include our samples [67–69].

The new design of the sensor cell is illustrated in Fig. 4.2. It consists of three layers, each with its specific functionality. The cover holds the integrated fluid connectors, glued into vertically centered horizontal holes on both sides, and directs the liquid through small, milled channels in its bottom surface to the center of the cell. The approximately 3 mm thick PDMS layer seals the cell at the interface to the cover on the top, as well as at the interface to the sample at the bottom. This layer was cast featuring a $70\ \mu\text{m}$ high channel on its bottom surface. The respective mold was fabricated through optical

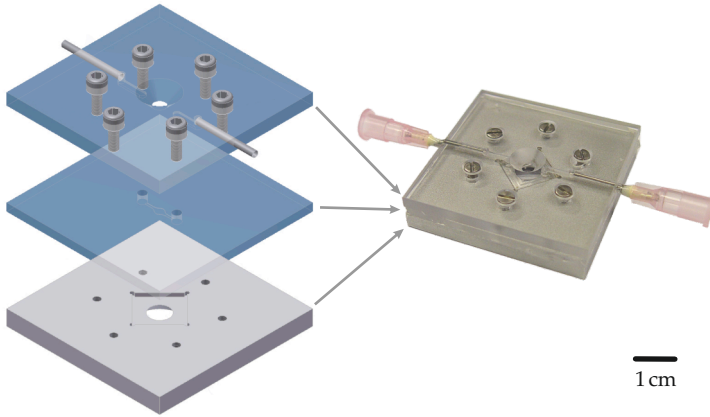


FIGURE 4.2: Schematic and picture of the three layer microfluidic cell. Sealing and definition of the microfluidic channel is provided by a transparent silicone material. The cover layer with integrated liquid connectors allows quick assembly and reutilization of the cell. Together with the base plate all components are fixed tightly and can be mounted in the measurement setup.

lithography in MicroChem SU-8 2025 resist on a silicon wafer. Afterwards, small holes were punched into the layer, guiding the liquid from the channels in the cover through the PDMS into the microfluidic channel aligned with the sample. The sample itself rests in a tightly fitting indent in the base plate, which is equipped with threads on the bottom to be perfectly fixed in the measurement setup. Uniform pressure can be applied by six screws to aid the sealing and to prevent movement of the individual components. Conical holes in the cover and base plate avoid obstruction of the light path.

The main advantages of this cell include its short assembly time, its reusability, and good sealing properties. Furthermore, the microfluidic channel allowed to minimize absorption of the water as well as a fast exchange of the small analyte volume above the nanostructures. By using the substrate as the bottom of the cell, we also eliminated two of the additional interfaces in the beam path.

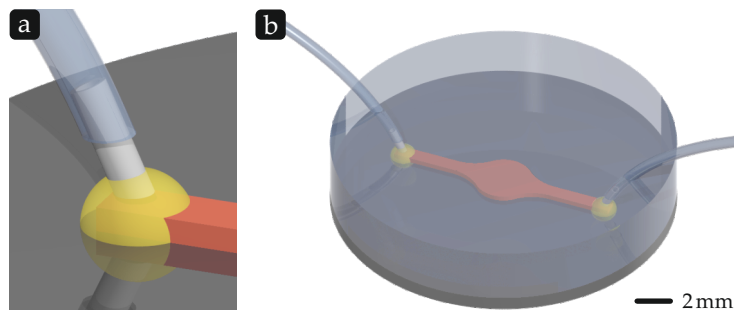


FIGURE 4.3: (a) Detail of the mold fabrication for casting the tubing directly into the silicone layer. The tubing is fixed and sealed during the process by a short piece of injection needle. The needle is glued to the end of the microfluidic channel defined in resin by optical lithography. (b) Overview of the fabricated structure after casting.

Nevertheless, particularly the measurements with hydrogel covered nanostructures and biological substances in chapter 6 required further improvements. As it turned out, the rough surface of the milled channels in the cover facilitates the formation of air bubbles from the analyte solutions. Those bubbles predominantly accumulated on the hydrogel film and got stuck in the microfluidic channel, rendering complete measurement series unusable. Another shortcoming was the number of edges and corners in the liquid flow, leading to residual amounts of old analyte solution after a change, and hence unclear separation of the different analyte solutions. Additionally, reducing the inner diameter of the used tubing appeared reasonable. Although the standard medical tubing allowed easy setup of the equipment, the volume was too large compared to the microfluidic channel, resulting in long delay times when changing the analyte solutions.

Based on the existing cell, we again decreased the number of separate components and paid special attention to smooth surfaces and connections. In the final microfluidic cell, the inlet and outlet tubing with an inner diameter of 0.3 mm are therefore directly cast into the PDMS layer. As illustrated in Fig. 4.3 a short piece of an injection needle with an outer diameter of

0.3 mm is glued on the fabricated mold for the microfluidic channel. The tubing is mounted on the needle, which seals it and keeps it in place during the subsequent casting process. When the layer is detached from the mold the needles are removed, leaving a continuous transition from the tubing to the channel. The key point here is the utilization of silicone tubing that, in contrast to standard polyethylene tubing, perfectly merges with the ambient material. The cover is provided with extra holes for the tubing and is still necessary to tightly kept the components together.



SENSING WITH COMPLEX COUPLED PLASMONIC STRUCTURES

Localized surface plasmon resonance (LSPR) spectroscopy of metallic nanostructures has become a highly promising platform for chemical and biological sensing experiments [70,71]. The high field enhancement near the LSPR causes its far-field spectrum to be highly sensitive to changes in its local nanoscale dielectric environment. Ultimately, real time detection of the binding and unbinding of single molecules to an individual resonator may be possible [71]. Many authors have considered the problem of optimizing the performance of plasmonic sensors. Besides a variety of chemically synthesized and lithographically fabricated nanostructures, also different sensing scenarios were used. Those include detection of resonance shifts or transmittance/reflectance changes (cf. Fig. 5.1a,b), in combination with changes of the analyte in the bulk volume or restricted to the surface of the structures (Fig. 5.1c,d). Sherry et al. first defined the so called figure of merit (FOM) for a plasmonic sensor as the ratio of the bulk sensitivity to the full width at half maximum of the resonance under question [72]. This definition allowed the comparison of different nanoparticles for sensing the bulk refractive index change. Employing a quasi-static approximation and linearizing the dispersive permittivity of the metal, Miller and Lazarides developed an analytical theory for the determination of bulk sensitivity. They show that the sensitivity is a linear function of the sensing wavelength (see Fig. 6 in [73]). Otte et al. performed a theoretical and experimental analysis of both bulk and surface sensing schemes based on plasmonic nanoparticles and concluded that the optimal spectral position is at the point of maximum ratio between the real and the imaginary part of the permittivity of the metal [74]. For the case of surface molecule sensing, Nusz et al. developed an analytical formulation that predicts a nanorod sensor's perfor-

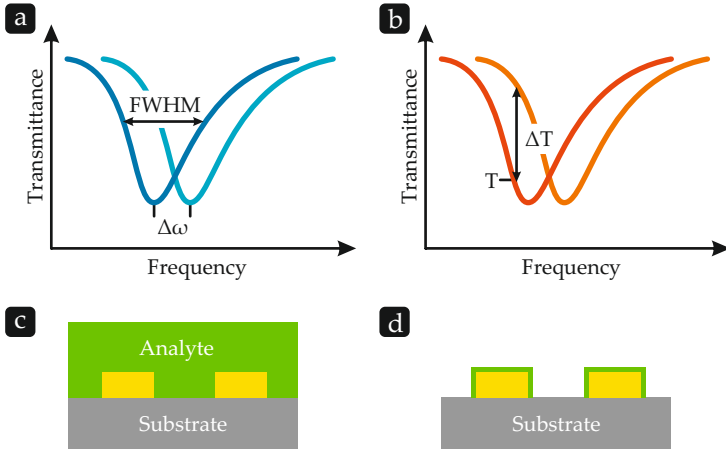


FIGURE 5.1: Possible refractive index sensing schemes. (a) The shift of a plasmonic resonance is used as the sensor signal. (b) Alternatively an intensity change ΔT at a fixed spectral position can be used. (c) Furthermore, either the refractive index of the entire cover layer is altered, corresponding to the bulk sensing case. (d) Or only a thin layer around the structure changes its refractive index, simulating for example a molecular monolayer.

mance for its use in sensing a small number of molecules [75]. Unger et al. have considered sensing systems in different noise regimes and derive suitable figure of merit definitions in each regime [76]. Employing a quasi-static perturbation theory, they have first described a determination of the principles of a sensor's performance. Becker et al. consider a variety of FOM quantities and study the optimization of the geometry of a gold nanorod in this context [77].

Obviously, there is a variety of different definitions for the FOM of a plasmonic sensor. The particular definitions are, however, usually motivated and influenced by the measured quantity, e. g., resonance shifts or transmittance/reflectance changes, as well as experimental details such as the noise of the setup. Furthermore, some of the definitions were made for systems exhibiting a single Lorentzian-shaped resonance and are hard to apply to more complicated spectra of, for example, coupled

plasmonic structures. This suggests the need to analyze and compare plasmonic sensors on a more fundamental level.

In the following, we present our method to analyze plasmonic structures with respect to their application as sensors. While single plasmonic nanoparticles can exhibit high field enhancement, their dipole like radiation characteristics produce a broad line width resonance. Fano resonances, instead, combine a narrow line width with an ultrasmall mode volume and hence are the ideal candidates for label free sensing with extremely high sensitivities and very small analyte volumes [78].

One nanoplasmonic metamaterial with an electromagnetically induced transparency (EIT)-like spectrum exhibiting a particularly deeply modulated narrow line width Fano resonance has been reported by Liu et al. [79]. By treating the system as an open electromagnetic resonator, its sensitivity to refractive index changes, in the bulk volume as well as just in a thin layer on its surface, is related to its effective mode volume and quality factor. This allows an intuitive insight of sensor performance on the nanostructure geometry.

5.1 PERTURBATION THEORY

In a sensing configuration employing an optical resonator, we have the sensing element (e. g., an antibody), the optical resonator and a readout mechanism that monitors changes in the optical spectrum of the resonator [80]. The resonator is in close proximity to an analyte of a certain spatial distribution and refractive index characteristic. The generalized sensor optimization problem is thus to find a suitable geometry and the frequency of the incident light ω_{inc} such that a refractive index change Δn_a for a given analyte volume yields a spectral signal with a high figure of merit. Here, we consider the shift of the resonance position and the difference in reflectance/transmittance as the two spectral measures of interest. The intensity sensitivity can be easily related to the frequency sensitivity via $\frac{\Delta T}{\Delta n_a} = \frac{\partial T}{\partial \omega} \frac{\Delta \omega_{\text{res}}}{\Delta n_a}$ when the intensity changes are monitored in a mostly linear part of the spectrum. We thus focus on the frequency sensitivity $\Delta \omega / \Delta n_a$ as an important determinant.

Here, we consider an arbitrary arrangement of plasmonic resonators and an analyte of arbitrary shape in its vicinity. The analyte volume can be the entire infinite half space (which is the limit of bulk sensing), a layered setup [81] (which is a surface sensing limit), or even a single molecule (modeled as a small sphere as in [76]). An incident monochromatic plane wave of temporal frequency ω_{inc} excites the system and the resulting scattered field is monitored in the sensing configuration. Upon a change in the dielectric properties of the analyte, the scattered field configuration changes. We are now interested in measuring the change in resonance of the resonator by considering the change in the dielectric properties of the analyte as a small perturbation $\Delta\varepsilon(\mathbf{r})$. The mode $\mathbf{E}^u(\mathbf{r})$ of the unperturbed resonator with spatially changing and dispersive complex dielectric function $\varepsilon_u(\mathbf{r}, \omega)$ and the mode $\mathbf{E}^p(\mathbf{r}) = \mathbf{E}^u(\mathbf{r}) + \Delta\mathbf{E}(\mathbf{r})$ of the perturbed resonator with its dielectric environment $\varepsilon_p(\mathbf{r}, \omega)$ both satisfy the wave equation:

$$\nabla \times (\nabla \times \mathbf{E}^u(\mathbf{r})) = \omega_u^2 \varepsilon_u(\mathbf{r}, \omega) \mathbf{E}^u(\mathbf{r}), \quad (5.1)$$

$$\nabla \times (\nabla \times \mathbf{E}^p(\mathbf{r})) = (\omega_u + \Delta\omega)^2 \varepsilon_p(\mathbf{r}, \omega) \mathbf{E}^p(\mathbf{r}). \quad (5.2)$$

We assume that the perturbation is small, such that $\varepsilon_p(\mathbf{r}, \omega) = \varepsilon_u(\mathbf{r}, \omega) + \Delta\varepsilon(\mathbf{r}) + \Delta\omega \frac{\partial \varepsilon_u(\mathbf{r}, \omega)}{\partial \omega}$, where we have accounted for the change in permittivity due to dispersion. Assuming that the incremental quantities are small, we ignore the higher order terms. Subtracting eq. 5.1 from eq. 5.2 yields

$$\begin{aligned} \nabla \times [\nabla \times \Delta\mathbf{E}(\mathbf{r})] - \omega_u^2 \varepsilon_u(\mathbf{r}, \omega) \Delta\mathbf{E}(\mathbf{r}) = \\ \left[\omega_u^2 \Delta\varepsilon(\mathbf{r}) + 2\omega_u \Delta\omega \varepsilon_u(\mathbf{r}, \omega) + \omega_u^2 \Delta\omega \frac{\partial \varepsilon_u(\mathbf{r}, \omega)}{\partial \omega} \right] \mathbf{E}^u(\mathbf{r}). \end{aligned} \quad (5.3)$$

Both sides of eq. 5.3 are multiplied by $\mathbf{E}^u(\mathbf{r})$ and a volume integration is carried out over Λ (a spherical volume of radius

R around the resonator, much greater than the size of the resonator and the incident wavelength) to yield

$$\begin{aligned} & \int_{\Lambda} dV \mathbf{E}^u(\mathbf{r}) \cdot \left[\nabla \times (\nabla \times \Delta \mathbf{E}(\mathbf{r})) - \omega_u^2 \varepsilon_u(\mathbf{r}, \omega) \Delta \mathbf{E}(\mathbf{r}) \right] = \\ & \int_{\Lambda} dV \omega_u^2 \Delta \varepsilon(\mathbf{r}) \mathbf{E}^u(\mathbf{r}) \cdot \mathbf{E}^u(\mathbf{r}) + \\ & \int_{\Lambda} dV \left[2\omega_u \Delta \omega \varepsilon_u(\mathbf{r}, \omega) + \omega_u^2 \Delta \omega \frac{\partial \varepsilon_u(\mathbf{r}, \omega)}{\partial \omega} \right] \mathbf{E}^u(\mathbf{r}) \cdot \mathbf{E}^u(\mathbf{r}). \end{aligned} \quad (5.4)$$

If the fields of a resonator are finitely extended in space, giving a finitely integrable energy density, we have a closed system and the integrals in eq. 5.4 are easily evaluated. In an open system, however, the fields are not strictly confined but instead energy leaks to its surrounding. A plasmonic resonator used as a sensor is thus an open or “leaky” cavity. The resonant modes of the leaky cavity have complex frequency eigenvalues with the imaginary component describing the rate of leakage. More importantly, their eigenfields are infinite in extent, making it difficult to evaluate normalization integrals. In general, the plasmonic resonator is non-hermitian. While for a hermitian system, the left hand side of eq. 5.4 would vanish, a non-hermitian system has circulating surface currents on the boundary. For a sufficiently far enough boundary surface, the electric field is essentially of plane wave nature. These approximations help to eliminate $\Delta \mathbf{E}(\mathbf{r})$ from eq. 5.4 (see [82]). By approximating $\Delta \varepsilon = 2\varepsilon_a \Delta n_a / n_a$ the expression for the sensitivity becomes

$$\frac{\Delta \omega}{\Delta n_a} \approx \frac{\omega_u}{n_a} \frac{\int_S dV \varepsilon_u(\mathbf{r}, \omega) [\mathbf{E}^u(\mathbf{r})]^2}{\int_{\Lambda} dV \frac{1}{2} \tilde{\varepsilon}_u [\mathbf{E}^u(\mathbf{r})]^2 + \frac{inc}{2\omega_u} \int_R dA [\mathbf{E}^u(\mathbf{r})]^2}, \quad (5.5)$$

where the integral in the numerator is carried out over the analyte volume S and

$$\tilde{\varepsilon}_u(\mathbf{r}, \omega) = \varepsilon_u(\mathbf{r}, \omega) + \frac{\partial (\varepsilon_u(\mathbf{r}, \omega) \omega)}{\partial \omega}. \quad (5.6)$$

In a medium with dispersive permittivity, with the imaginary part of the relative permittivity being smaller than the real part, the electromagnetic energy density is given by

$$W(\mathbf{r}) = \frac{\epsilon_0}{4} \tilde{\epsilon}_u(\mathbf{r}, \omega) [\mathbf{E}^u(\mathbf{r})]^2. \quad (5.7)$$

Hence, the sensitivity is related to the energy storage in the analyte volume compared to the overall energy storage of the resonator. This gives an intuitive view for the sensitivity as the relative frequency shift equals the relative refractive index contrast multiplied by the fraction of the total energy contained within the analyte volume [76]. Assuming a Drude like dispersion relation for the metal's relative permittivity ($\epsilon(\omega) = 1 - \omega_p^2 / [\omega^2 + i\gamma\omega]$) and no magnetic dispersion, the electromagnetic energy density is given by (see eqn. 16 in [83])

$$W_e(\mathbf{r}) = \frac{\epsilon_0}{2} \left\{ \Re[\epsilon(\omega)] + \frac{\omega \Im[\epsilon(\omega)]}{\gamma} \right\} [\mathbf{E}^u(\mathbf{r})]^2, \quad (5.8)$$

where γ is the damping parameter of the Drude model.

5.2 CALCULATION OF THE MODE VOLUME

Resonant optical cavities are typically characterized by their quality factor Q and effective mode volume V_{eff} . The quality factor Q quantifies the temporal confinement of the electromagnetic energy and is defined as

$$Q = \frac{U(t)}{-\frac{1}{\omega_0} \frac{\partial U(t)}{\partial t}} = \frac{\omega_u}{\Delta\omega_{\text{FWHM}}}, \quad (5.9)$$

where $U(t)$ is the total energy of the confined electromagnetic field, $-\partial U(t)/\partial t / \omega_0$ is proportional to the energy that is lost for each electromagnetic oscillation and $\Delta\omega_{\text{FWHM}}$ is the line width of the unperturbed resonator [80]. The effective mode Volume V_{eff} quantifies the spatial distribution of the electric field of a resonant mode and was extended to the case of plas-

monic resonators by Maier by integrating the electromagnetic energy density given in eq. 5.7 as

$$V_{\text{eff}} = \frac{\int dV \tilde{\epsilon}_u(\mathbf{r}, \omega) [\mathbf{E}^u(\mathbf{r})]^2}{\max \left\{ \tilde{\epsilon}_u(\mathbf{r}, \omega) [\mathbf{E}^u(\mathbf{r})]^2 \right\}}, \quad (5.10)$$

where the integration is supposed to be over all space [84].

However, for a finite Q , the fields necessarily start to diverge at large distances [85]. The calculation of the mode volume for a plasmonic cavity is thus non-trivial. A detailed analysis of the applicability of this definition of mode volume to a plasmonic resonator was given by Koenderink, where the case of a plasmonic sphere was considered and it was concluded that the Purcell factor calculated with this method is inadequate [86]. The integration of the energy density was seen to diverge and the mode volume was simply defined to not include any divergent contribution. In [76], fields below a certain cut-off were not considered to achieve convergence. From eq. 5.5 we can thus adopt the following definition (see [85]) of the mode volume:

$$\frac{1}{V_{\text{eff}}} = \Re \left(\frac{\max \left\{ \tilde{\epsilon}_u [\mathbf{E}^u(\mathbf{r})]^2 \right\}}{\int_{\Lambda} dV \tilde{\epsilon}_u [\mathbf{E}^u(\mathbf{r})]^2 + \frac{inc}{2\omega_u} \int_R dA [\mathbf{E}^u(\mathbf{r})]^2} \right). \quad (5.11)$$

The figure of merit can then be written as

$$\text{FOM} = \frac{1}{\Delta\omega_{\text{FWHM}}} \frac{\Delta\omega}{\Delta n_a} = \frac{Q}{V_{\text{eff}}} V_{\text{eff}}^{\text{analyte}}. \quad (5.12)$$

To derive other figures of merit the definition of $V_{\text{eff}}^{\text{analyte}}$ can be suitably modified. This expression for the figure of merit enables the comparison of a wide variety of optical resonator based sensors. And the effective analyte volume can be defined as

$$V_{\text{eff}}^{\text{analyte}} = \frac{\int_S dV \epsilon_u(r, \omega) [\mathbf{E}^u(\mathbf{r})]^2}{\max \left\{ \tilde{\epsilon}_u(\mathbf{r}, \omega) [\mathbf{E}^u(\mathbf{r})]^2 \right\}}. \quad (5.13)$$

The Q factor and the effective mode volume have to be evaluated only once per structure. Subsequently, an optimal analyte

configuration can be found by using the simulated field values. This permits a full systematic optimization.

5.3 CHARACTERIZATION OF AN EIT-LIKE STRUCTURE

A sensing scheme using the EIT-like plasmonic resonator depicted in Fig. 5.2 is investigated below. The underlying plasmonic resonator consists of two functional layers. The bottom dipole layer acts as the broad line width antenna that couples to free space propagating plane waves. The top functional layer, consisting of two parallel bars of equal length, supports a spectrally narrower quadrupole resonance. The design of the layers ensures that the quadrupole resonance lies within the broad line width of the dipole, ensuring efficient coupling between the two layers. Moving the dipole antenna away from its symmetrical position allows to tune the coupling strength. The sensing function is performed by altering the local environment of the quadrupole bars. In the following, two sensing schemes are considered. Bulk sensing, where the changes affect the entire half space surrounding the quadrupole bars and a surface sensing approach, where just a thin layer around the gold wires is changed.

The simulation of the structure was carried out in the commercial finite element frequency domain electromagnetic solver CST Microwave Studio (cf. chapter 3)¹. The entire structure is periodic in both the x and y directions with a periodicity of 700 nm. Unit cell boundary conditions were used in the periodic dimensions and Floquet ports were used on the z dimension with an overall size of $3.2\ \mu\text{m}$. The polymer spacer layer is 70 nm thick. The dipole bar is 290 nm long and 95 nm wide. The quadrupole bars are 285 nm long and 80 nm wide and are separated from each other by 220 nm from the inner surface to inner surface. All bars are 40 nm thick. The substrate glass has a refractive index of $n_{\text{glass}} = 1.5$, the dipole driving bar is covered in a polymer with a refractive index $n_{\text{poly}} = 1.55$ and the quadrupole bars are assumed to be covered in water ($n_{\text{H}_2\text{O}} =$

¹ Final simulations by R. Hegde, A*STAR Institute of High Performance Computing, Singapore

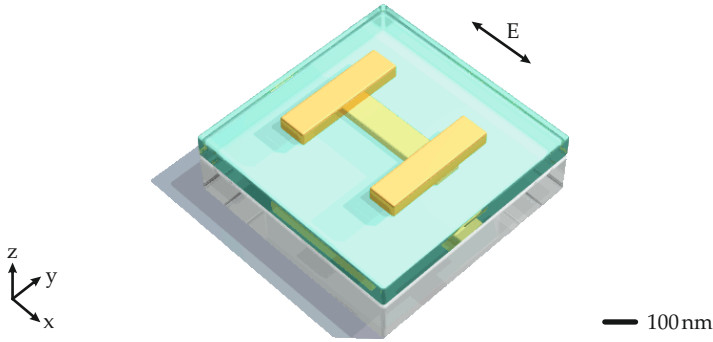


FIGURE 5.2: Schematic of a plasmonic structure providing an EIT-like resonance. A dipolar nanoantenna in the bottom layer is coupled to two parallel nanoantennas in the top layer, which support a quadrupolar mode. The coupling strength can be tuned by displacing the antenna in the bottom layer from the symmetric position.

1.33). The gold dipole and quadrupole bars are modeled as a Drude metal with plasma frequency $\omega_p = 1.37 \times 10^{16}$ rad/s and damping frequency $\gamma = 1.94 \times 10^{13}$ Hz. The meshing results in approximately 350 000 tetrahedral meshcells. A total field/scattered field formulation is used to obtain the scattered fields of the resonator at any particular frequency. As a reference, a similar simulation without the gold structures, but maintaining the same mesh, has been performed.

The evolution of the transmission spectrum and the sensing performance for the EIT-like sensor with varying displacement S is depicted in Fig. 5.3. It can be seen that a transmission window opens up in the broad absorption window of the driving dipole resonator. The details of the spectral evolution in Fig. 5.3a are similar to the spectral evolution of the plasmonic EIT prototype system discussed in [79]. A deeper modulation and steeper slopes emerge with increasing coupling. For the corresponding displacements S , the dielectric environment of the quadrupole bars was changed in the full half space (see Fig. 5.2b) and in a surface layer (see Fig. 5.2c), respectively. The relative changes in the transmission occur predominantly at two points in the spectrum. Furthermore, with increasing

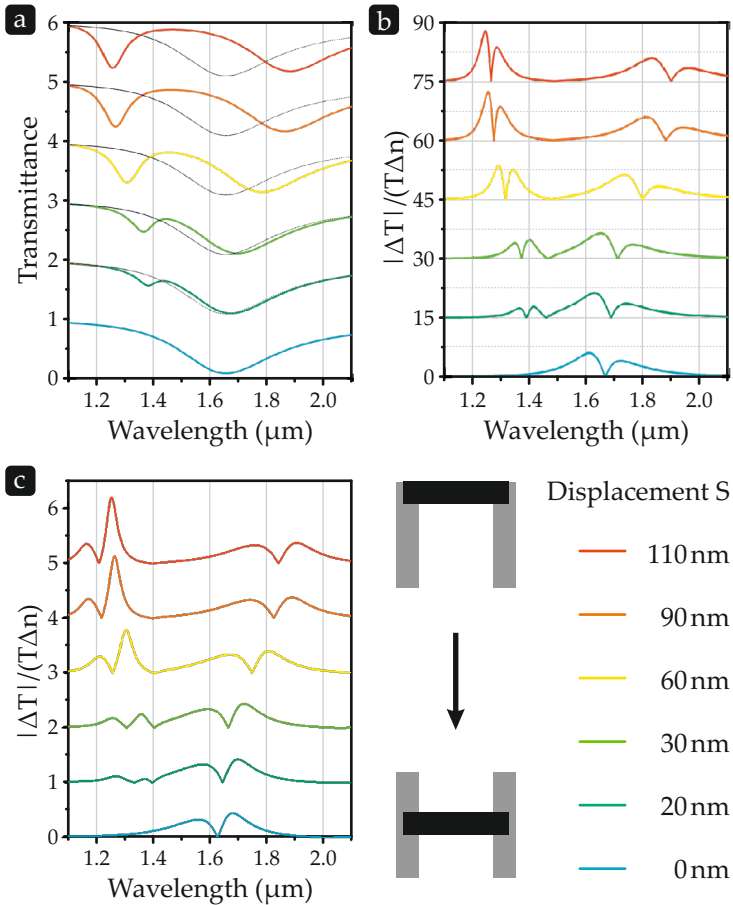


FIGURE 5.3: (a) Transmission spectra for varying coupling strength caused by shifting the dipole bar. (b) Relative transmittance change if the refractive index of the entire half space above the quadrupole bars is altered by 10%. (c) Relative transmittance change if the change in the refractive index is restricted to a 10 nm layer above the quadrupole bars.

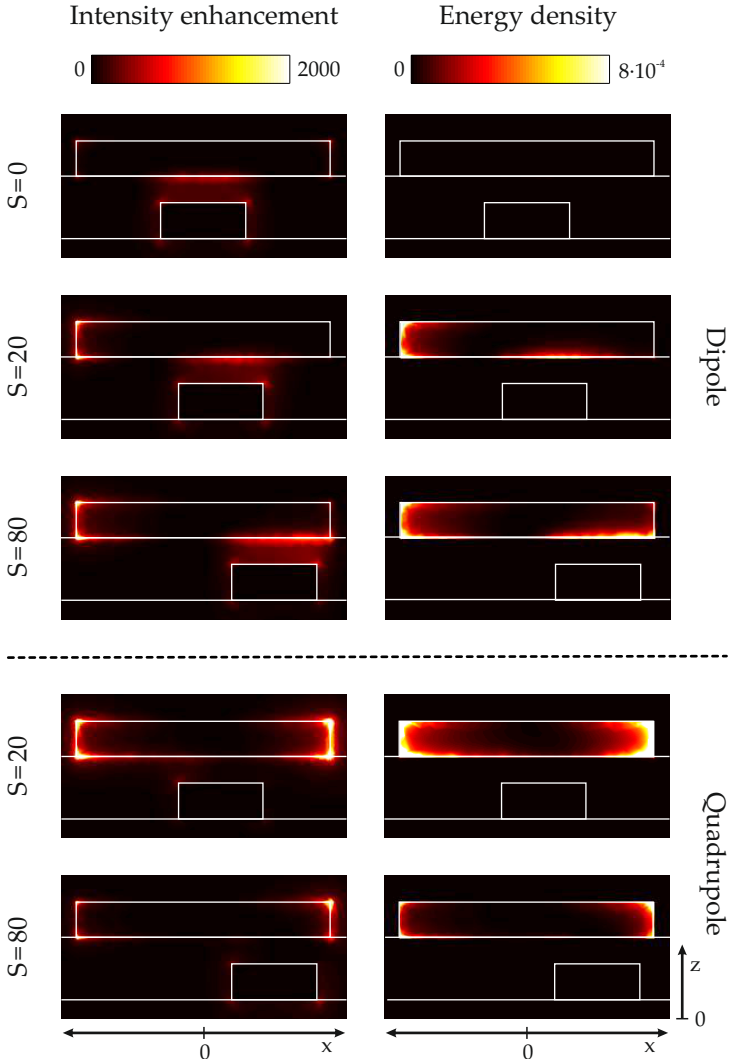


FIGURE 5.4: Cross sectional plots of the intensity enhancement and energy density at the frequencies of the dipole and quadrupole mode: The $x - z$ plane is located along the inner sidewalls of the quadrupole bars. The dipole bar is placed at $S = 0$ nm, 20 nm, and 80 nm, respectively. The incident electric field is polarized along the y axis.

S , one of these regions is seen to redshift and the other to blueshift, as a dielectric perturbation will result in the spectral displacement of both hybrid modes. However, because of the shape of the spectrum, the low energy mode is best detected in terms of frequency change, whereas the high energy mode is best detected via a change in the transmitted/reflected intensity at a fixed frequency. Near the Fano resonance, the slope is almost linear. Therefore, we can relate the intensity sensitivity to frequency sensitivity and we will focus on frequency sensitivity in the following.

Gallinet et al. have reported a rigorous ab initio theory of Fano resonances in plasmonic nanostructures and metamaterials using the Feshbach formalism [87]. A Fano resonance occurs in the resonator from the interference between the continuum of radiative waves from the driving dipole bar and the non-radiative quadrupole mode from the top bars. The reflectance of the entire system is given by the product of the Lorentzian reflectance spectrum of the dipole modulated by the quadrupole resonance [88,89]. Using their expression to fit our simulated spectra, the frequencies of the dipole and quadrupole modes can be obtained.

Reference simulations (where the gold bars were removed) and the full simulations were performed at the frequencies of the dipole and quadrupole modes. These calculations leads to the scattered electric field for the two modes. A mesh convergence test was carried out to ensure that the resulting field integrals converge. The variation in the energy density and electric field intensity enhancement is shown in Fig. 5.4. We observe the strongest field enhancement near the quadrupole bars for both resonant modes. Therefore, the inverted configuration of the EIT resonator is ideal for sensing, as it exposes the quadrupole bars to the sensing volume. The low energy mode has a stronger field enhancement in the region between the rods. We also see that $S = 20$ nm is the optimal bar position for generating the highest field enhancement at the quadrupole bars. While larger values of S increase the coupling between the dipole to the quadrupole, they also cause an impedance mismatch between the plane wave and the res-

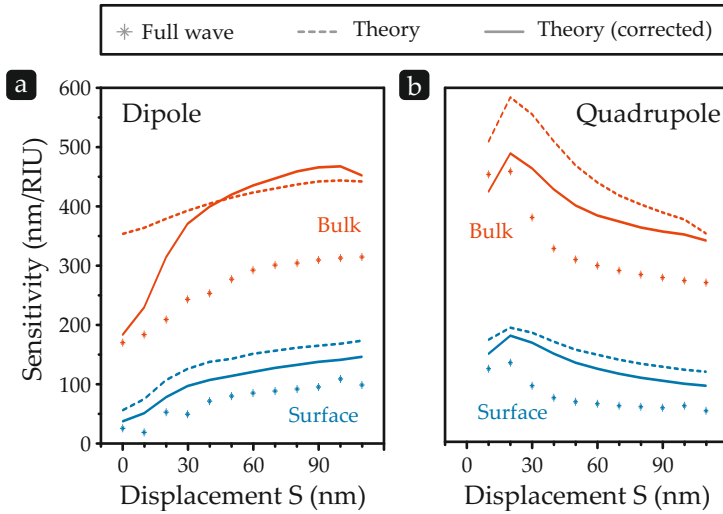


FIGURE 5.5: Comparison of sensitivities for varying coupling strength S obtained by different methods: Both bulk and surface sensitivities are obtained from simulated spectra for (a) the dipole mode and (b) the quadrupole mode. Values calculated using the perturbation theory are evaluated with a thresholding and a second surface integral corrected method.

onator. Hence, stronger coupling does not improve the field enhancement [87–89].

We have already established the relationship between far field spectral sensitivity to the near field integrals of energy density (cf. eq. 5.8). The evaluation of mode volumes and the sensitivity both involve integrating the energy density. In case of an open resonator these integrals do not converge. In particular, for the EIT resonator, a linear divergence was observed for all the energy integrals with increasing volume. We adopted two solutions to deal with this divergence. First, the divergence was simply dropped by taking the intercept, similar to Koenkerink [86]. Another correction was introduced based on our derivation. The exact expression is cumbersome to evaluate, as it requires a surface integral to be performed at a far enough distance to the resonator. A corrected approximation to the

integral was obtained by performing the volume integration over a box of a height approximately equal to one wavelength and subtracting a surface integral on the faces of the box (see Fig. 5.5). Strictly speaking, the perturbation theory is only valid for small changes in permittivity in small regions around the resonator. However, for a 10% change in refractive index, even in the bulk case, the qualitative agreement between the theory and full wave simulations is notable. The peak sensitivity is observed for $S = 20$ nm. This finding is consistent with our previous results as the energy stored in the near-fields reaches its maximum. A similar behaviour has been observed by Gallinet et al. for a displacement of $S = 20$ nm.

5.4 EXPERIMENTAL VERIFICATION

The coupled plasmonic nanostructure discussed above has also been realized experimentally. For that purpose, a multilayer electron beam lithography (EBL) process was used to fabricate the gold nanoantennas (see chapter 3). Five $90\ \mu\text{m} \times 90\ \mu\text{m}$ arrays of structures with nominal dimensions corresponding to the simulations and varying displacements S of the lower antenna from its symmetric position were fabricated. The displacements on the different arrays cover the whole range from the uncoupled system to the case of strong coupling, corresponding to values of S ranging from 0 nm to 110 nm. The sample was placed in the custom-made microfluidic cell introduced in chapter 4 with a $70\ \mu\text{m}$ high channel guiding the analyte solutions over the nanostructures. To obtain a refractive index difference $\Delta n \approx 0.05$, deionized water and a mixture of water with ethylene glycol was used. Transmittance spectra were recorded using a Fourier-transform infrared (FTIR) spectrometer and an attached infrared microscope as described in chapter 3. Reference measurements were taken next to the nanostructures, through cell, analyte and substrate.

The scanning electron microscope images in Fig. 5.6c depict a single element of the fabricated arrays, respectively. In accordance with the simulation, the high energy resonance evolves with increasing displacement S . The experiment also confirms

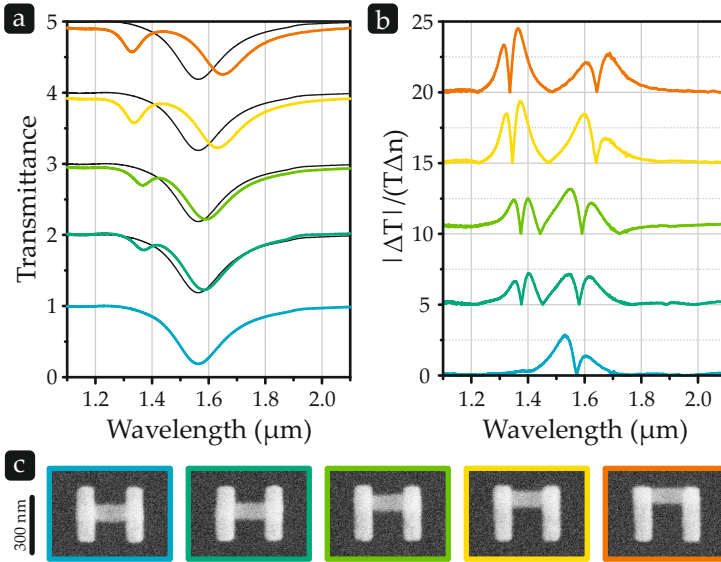


FIGURE 5.6: Experimental investigation of the coupled structure. (a) Increasing displacement of the bottom antenna intensifies the coupling and leads to the formation of two hybrid modes. (b) Changing the refractive index above the structure causes a relative transmittance difference, which is highest in the strong coupling case. (c) SEM images depicting the fabricated structures corresponding to the particular measurements.

the redshift of the low energy resonance and the blueshift of the high energy resonance for growing coupling strength (see Fig. 5.6a). Both effects are, however, less pronounced than in the simulation. This can in part be attributed to less efficient near-field coupling in the experiment, which might result from experimental imperfections, such as deviations in the polymer layer thickness. This thickness, which defines the vertical distance of the gold nanoantennas, has a crucial impact on the coupling strength. The relative transmittance changes (Fig. 5.6b) additionally confirm the trend in the simulation, indicating that the sensitivity of the high energy resonance exceeds the one of the low energy resonance for strongly coupled struc-

tures. The experimentally obtained shifts of the resonance position are between 540 nm and 480 nm for the high energy resonance and exhibit a decreasing tendency. For the low energy resonance, the shifts follow an increasing trend between 135 nm and 205 nm. Both are in good agreement with the calculated values depicted in Fig. 5.5.

5.5 CONCLUSION

In this chapter, we presented our method based on perturbation theory to describe the performance of complex coupled plasmonic nanostructures for refractive index sensing. The theory relates the far field spectral changes to the near field energy density distribution of the resonator. We have seen that the shift of the resonant modes is directly related to the energy storage in the analyte volume. The determination of the mode volume of the resonator for has been discussed. Our perturbation theory shows good qualitative agreement with full wave simulations. The advantage of the method lies in the ability to optimize the sensor for a particular sensing task, e. g., bulk or surface layer sensing, based on a single calculation of the resonant modes. Both scenarios were investigated using the resonance shift as well as an intensity difference at the slope of the resonance as the sensor signal. While resonance shifts are maximal at the high energy mode in the case of weak coupling, intensity differences are best detected in the strong coupling regime. Here, the distinct resonances and steep slopes lead to enhanced signals. We could additionally verify that our calculations reproduce the experimental behaviour of the investigated system.

In the recent years a lot of effort has been put into the theoretical description of such complex coupled plasmonic structures and considerable progress has been made. Newer versions of the in-house implementation of the S-matrix approach (cf. chapter 3) allow to obtain the eigenmodes of arbitrary structures directly by searching for solutions of Maxwell's equation that can oscillate in time without an external excitation. Furthermore, an analytical normalization of those eigenmodes,

particularly for the case of periodic structures, is possible without the need for surface integrals far away from the plasmonic structure [90]. In the next steps other complex coupled plasmonic structures might be analyzed in a similar fashion to gather insight in their sensing performance for a detailed comparison.



FUNCTIONALIZED HYDROGEL ASSISTED
PLASMONIC SENSING

Apart from our studies in the previous chapter, a variety of plasmonic metal nanostructures has been investigated with respect to application as sensors based on localized surface plasmon resonances (LSPRs). Many groups studied holes in metal films, nanoantennas, and arrangements of particles, exhibiting Fano-resonances or chiral properties to exploit the large sensitivity, small sensing volumes and high integration density provided by such systems [71,91–100]. Others focused on fabrication methods to generate high quality, large area arrays, e. g., nanosphere lithography, nanoimprint lithography, or nanostencil lithography [101–103]. Additional parameters, such as efficient delivery of analytes to the sensor, have also been subject to optimization [104]. As known from experiments, simulation and theory (cf. chapters 2 and 5) the exact optical properties, such as the resonance positions, depend strongly on the dielectric vicinity of the metal structures. Since the dielectric function is, however, influenced by almost any change in the surrounding material, an additional component is needed to provide selectivity.

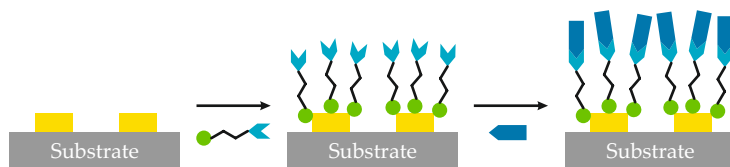


FIGURE 6.1: Molecule pairs with strong affinity to bind to each other are commonly used for functionalization of sensors. Provided that a suitable system is known, the desired analyte, as one part or the pair, will specifically bind to its counterpart immobilized on the sensor surface.

Independent of the structure in use, it is always a challenge to limit the otherwise very general response, which includes all changes in the effective refractive index of the environment, to a preferably single desired analyte. One established method is to directly attach selected molecules to the metal, e. g., to gold via a thiol group, which will in turn bind the desired analyte molecules and cause the change in the environment of the antennas (Fig. 6.1). In experiments, the analyte solution is guided to the sensitive area and allowed to react for a specific duration, before flushing the sample with a clean solution to wash away everything that is not bound to the gold structures. Subsequently, the resonance shift caused by the few additional molecules can be detected. The fact that this is a very diminutive refractive index change can to some extent be overcome as it is confined to the region with the highest field enhancement. Depending on the molecules, the analyte binding process may be permanent and hence, the sensor can be used only once. In the realm of biological sensing, immobilized antibodies are a widely used technique to bind the respective antigens to the sensor surface for detection [105]. For more general chemical sensing, direct functionalization, self-assembled monolayers with functional end groups, or embedding plasmonic structures in thin layers of chemically reactive materials are applicable methods [106–111]. Moreover, the vibrational signals of molecules in the infrared fingerprint region can be used by surface enhanced infrared absorption (SEIRA) spectroscopy to identify a broad range of substances, while still taking advantage of the enhanced electromagnetic fields of plasmonic nanoantennas [35]. Similarly, Raman spectroscopy can benefit from plasmonically enhanced surfaces and also allow for specific detection of analytes [112].

Among the many possible sensor designs, one class of non-plasmonic sensor concepts that has been significantly developed is based on hydrogels, which are hydrophilic cross-linked polymer networks soaked with water. Hydrogels are used in applications ranging from contact lenses to drug delivery and biosensing. They can be functionalized to respond to changes in temperature, pH, ionic strength, metal ions, antigens and

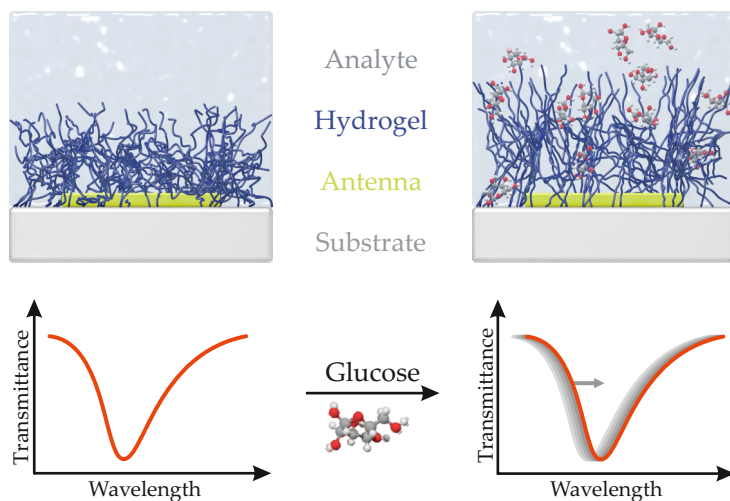


FIGURE 6.2: Schematic of the sensor concept. A plasmonic nanoantenna, exhibiting a resonance in the infrared spectral range, is covered by a functionalized hydrogel. In the presence of glucose the hydrogel swells, leading to a change in its effective refractive index. The impact on the nanoantennas can in turn be monitored through a shift of their resonance position.

the presence of a number of biomolecules [113–120]. The response, typically a reversible volume change of the gel, can then be read out as the sensor signal.

In our approach, we combine the high sensitivity of plasmonic nanoantennas with the advantages provided by a functionalization layer of a hydrogel, as illustrated in Fig. 6.2. This combination provides specificity for glucose, even in the presence of large proteins, and its response to glucose is reversible. However, it is important to note that our sensor concept is not limited to glucose, but can be adapted without any restrictions to many different analytes by choosing the appropriate hydrogel.

The following sections will enlarge upon the properties of the particular hydrogel used in our study, its application to

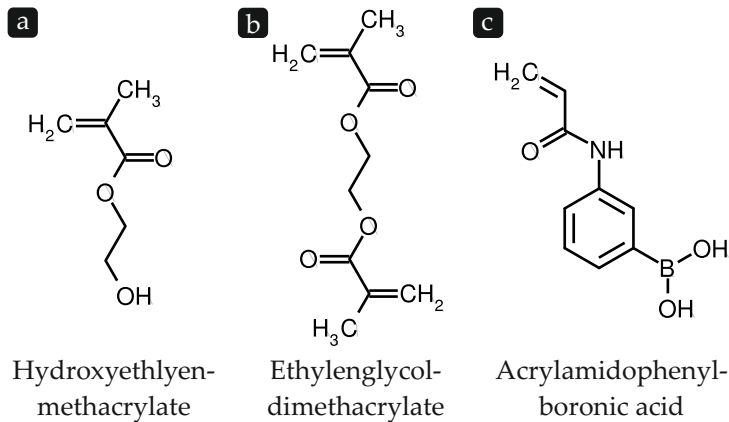


FIGURE 6.3: The hydrogel is a hydrophilic cross-linked polymer network soaked with water. It consists of (a) the monomer, (b) a cross-linker and (c) the glucose responsive functionalization.

arrays of plasmonic nanoantennas, and the detailed characterization of the combined system.

6.1 THE BORONIC ACID FUNCTIONALIZED HYDROGEL

The hydrogel in our experiments is used to coat the plasmonic nanoantenna arrays and provides a selective response to glucose molecules in the analyte solution. Hydrogels in general are hydrophilic cross-linked polymers. If immersed in water, the polymer gets soaked with liquid and exhibits its gel-like consistency. The polymer in this case has three components, that are depicted in Fig. 6.3. It mainly consists of the monomer hydroxyethylmethacrylate (HEMA), which can compose long polymer chains by free radical polymerization. Here, in simple words, the C=C double bond in the molecule is broken up by a free radical, using one of the two electrons to form a new bond to the former radical, leaving the combined molecule as a new radical to continue the process [121]. To get a three dimensional, more rigid structure, ethylene glycol dimethacrylate (EGDM) is added as a cross-linker. Because of the two avail-

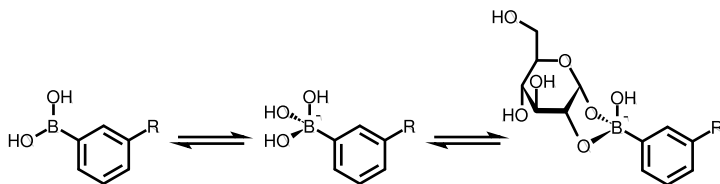


FIGURE 6.4: Phenylboronic acids can form a negatively charged complex with 1,2-cis-diols such as e. g., glucose. When covalently bound to a hydrogel, this leads to an influx of water.

able double bonds in this molecule, it is able to interconnect two chains and a cross-linked polymer network develops. The exact properties of the polymer can be adjusted by the ratio of monomer to cross-linker.

In order to make the hydrogel responsive to glucose, the reaction between glucose and a phenylboronic acid (PBA) is exploited. This Lewis acid interacts with 1,2-cis-diols such as glucose by forming a negatively charged complex (Fig. 6.4) [122]. If the PBA is covalently attached to a hydrogel the charged complex state increases the degree of ionization on the hydrogel and builds up a Donnan potential between the hydrogel phase and the bulk solution phase [123, 124]. The subsequent influx of ions and water leads to a swelling of the hydrogel. Owing to the different refractive indices of water ($n_{\text{water}} \approx 1.33$) and the polymer ($n_{\text{poly}} \approx 1.48$) the altered ratio of polymer to water also changes the gel's effective refractive index. This change can then in turn be observed through the plasmonic resonance of the nanoantenna arrays.

For incorporation into the polymer network, the PBA also needs an acrylic acid functional group. If present, it can simply be dissolved in the monomer and will occupy several sites in the final polymer, according to its share in the initial mixture.

6.2 SYNTHESIS OF ACRYLAMIDOPHENYLBRONIC ACID

For obtaining a stable functionalized hydrogel the PBA reacting with the glucose molecules has to be covalently bound

to the polymer backbone. This can be achieved by introducing acrylic acid moieties to 3-aminophenylboronic acid (APBA), which allows for integration into the polymer chains during their formation. As this particular molecule was at that time commercially unavailable, a procedure for its synthesis had to be established.

A first batch of N-3-acrylamidophenylboronic acid (AAPBA) was synthesized according to the procedure utilized by Lee et al. [125]. For this purpose, 3-aminophenylboronic acid hemisulfate (1.862 g, 10 mmol) was dissolved in 30 ml of deionized water in a round bottom flask. The pH value of the solution was adjusted to 4.8 by adding 2 mmol/l sodium hydroxide solution. The flask was stirred in an ice bath, and after temperature equilibration 1-ethyl-3-(3-dimethylaminopropyl)-carbodiimide hydrochloride (2.301 g, 12 mmol) was added, with subsequent pH adjustment to 4.8. In another container, acrylic acid (0.868 g, 12 mmol) was dissolved in 10 ml of water, and the pH value was adjusted to 4.8 as well. The solution was then slowly added to the main flask, which was capped with a rubber septum and allowed to stir for an additional hour. Afterwards, the flask was removed from the ice bath and left at room temperature over night. The reaction mixture was extracted four times with ethyl ether and the solvent was removed with a rotary evaporator. The resulting solid was analyzed by ^1H and ^{13}C nuclear magnetic resonance (NMR) spectroscopy, which confirmed the successful synthesis of AAPBA.

Because the yield of the previous method was as low as 30% and the appearance of a pinkish color during the process could not be explained, we decided to migrate to the procedure by Roy et al. [126]. Here, 1.0 g (7.3 mmol) APBA was dissolved in a round bottom flask containing a 1:1 mixture of tetrahydrofuran (13 ml) and water (13 ml). The solution was cooled in an ice bath (0-5 °C) and sodium hydrogen carbonate (1.226 g, 14.6 mmol) was added. Acryloyl chloride (1.19 ml, 14.7 mmol) was added dropwise and the reaction mixture stirred for 4 h. The solvent was subsequently evaporated and the obtained solid was stirred in ethyl acetate for 2 h. After filtering the solids, the organic layer was washed with water (15 ml), sat-

urated sodium bicarbonate (15 ml), water (15 ml), and brine (15 ml). The ethyl acetate was removed in a rotary evaporator, which yielded 1.115 g (80 %) of white solid. Recrystallization in water lead to a purified product in the form of needle-like crystals. Again, the process was verified by ^1H and ^{13}C NMR spectroscopy as well as mass spectroscopy.

With the availability of AAPBA we can in the following section now include the glucose responsive component into the hydrogel.

6.3 FABRICATION OF THE HYDROGEL LAYER

To allow for fast diffusion of glucose into the hydrogel, a thin layer has to be fabricated on top of previously manufactured arrays of nano antennas. As mentioned before, free radical polymerization is used to create the copolymer from the monomer mixture. Therefore, a small amount of Irgacure 651 photoinitiator (IR-651) is added to the mixture. This substance can be split into two free radicals on exposure with UV light and hence starts the polymerization.

The exact recipe used consists of HEMA (458 mg, 3.52 mmol), EGDM (7.5 mg, 37.8 μmol), AAPBA (45.35 mg, 237 μmol), and IR-651 (19.7 mg, 75.7 μmol) and is based on the publication of Lee et al. [125]. A mixture was prepared in a small centrifuge tube and slightly shaken until all ingredients were fully dissolved. Afterwards it was wrapped with aluminum foil to prevent polymerization by ambient light prior to use.

The polymerization process is illustrated in Fig. 6.5. Samples were prepared on 10 mm \times 10 mm \times 0.5 mm glass slides. Substrates containing several 100 μm \times 100 μm arrays of nanostructures fabricated by electron beam lithography (EBL) were submerged in 2 mmol/l methacryloxypropyltrimethoxysilane (MPMS) in toluene overnight, to introduce acrylate groups to the surface and hence later pin the hydrogel to the substrate. A mold featuring a 500 μm wide and 20 μm high channel with reservoirs on both sides was made by optical lithography and poly(dimethylsiloxane) (PDMS) casting (see chapter 3 for details). It was carefully placed on the substrate with the channel

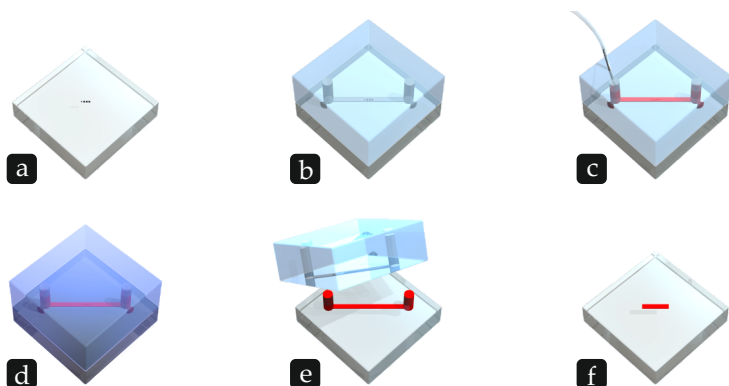


FIGURE 6.5: Fabrication of the hydrogel layer: (a) Substrates with nanostructures are functionalized with acrylate groups, (b) a mold with a $20\ \mu\text{m}$ high channel is aligned with the structures, (c) the monomer mixture is injected, (d) UV exposure starts the polymerization, (e) the mold is removed, and (f) the polymer is shaped.

aligned on the nanostructure arrays. The monomer mixture was injected and exposed to UV light during the following 15 min until the polymerization was reliably finished. Subsequently, the mold was removed and the hardened polymer could be shaped with a knife.

However, experiments quickly revealed that, although there was a response to glucose, it took several hours until an equilibrium was reached for a given concentration. Thus, development of an alternative process for thinner layers was necessary. Attempts were made to use spin-coating of the monomer solution, which is a standard technique for obtaining layer thicknesses down to tens of nanometers, e. g., in lithography. Despite functionalized surfaces, we were unable to accomplish an evenly wetted substrate with our particular monomer mixture. Furthermore, the polymerization in this case was quite challenging, as oxygen from the air hampers the creation of free radicals. Even maintaining a nitrogen atmosphere during the whole process did not yield satisfactory results.

The method that finally allowed to reliably fabricate layers with a thickness of $1\ \mu\text{m}$ is described in Fig. 6.6. Again, sub-

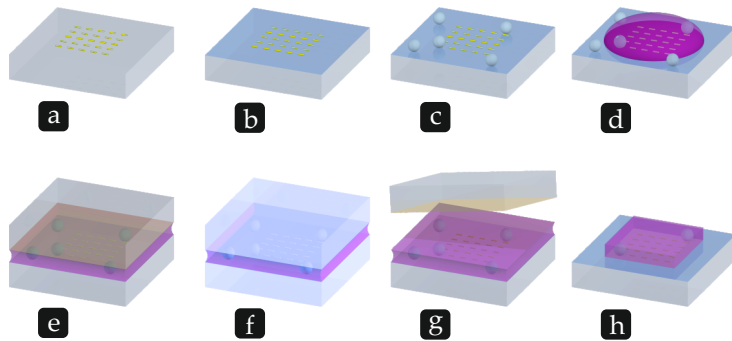


FIGURE 6.6: New fabrication of the hydrogel layer: (a) Nanostructures are fabricated, (b) the substrate is functionalized with acrylate groups, (c) PS beads are spin-coated as a spacer, (d) the monomer mixture is applied, (e) a functionalized cover is clamped to the substrate, (f) UV exposure starts the polymerization, (g) the cover is removed, and (h) the polymer is shaped.

strates with already fabricated gold antennas on top were submerged in 2 mmol/l MPMS in toluene overnight, to introduce acrylate groups to the surface. Another set of identical glass slides was during the same time treated in a 2 mmol/l solution of (tridecafluoro-1,1,2,2-tetrahydrooctyl) dimethylchlorosilane in chloroform to render them hydrophobic for their subsequent application as covers in the polymerization process. All slides were rinsed with isopropanol afterwards. A 2.6% (w/v) aqueous suspension of Polysciences Polybead[®] Microspheres with a diameter of 1.025 μm was diluted with ethanol. The polystyrene beads were spin-coated onto the samples at 2000 rpm to serve as a spacer. Afterwards, a small drop of the monomer solution was pipetted to the center of the substrate and covered with one of the top slides. Gentle movement of the cover under light pressure using the finger tip made the excess liquid to leak from the sides. Two clamps sustained the pressure and kept everything in place while the polymerization was initiated and allowed to continue for 15 min under UV light. The cover was then demounted, and the cured polymer was removed everywhere, except from a 1.5 mm \times 0.5 mm area above the gold

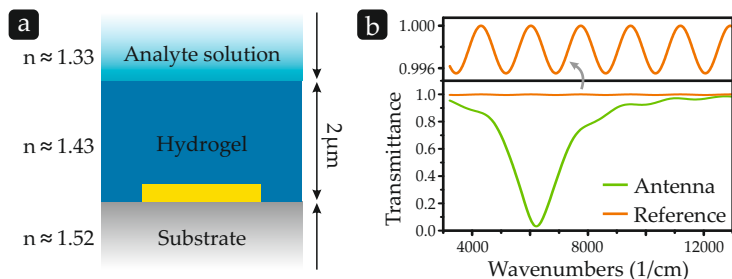


FIGURE 6.7: (a) Typical situation in the measurement: gold nanoantennas on a substrate coated with hydrogel and covered with analyte solution. (b) S-matrix simulations confirm modulations for the reference spectrum (without antenna) and antenna resonance spectrum.

nanoantennas. This had to be done manually with the help of a razor blade and microscope. Finally, the glass regions of the sample were again cleaned with isopropanol.

A last improvement of the fabrication process took place when we discovered that some of our measurements suffered from thin film interferences in the hydrogel layer. Fig. 6.7a illustrates the typical situation during an experiment with the hydrogel coated antenna on a substrate covered by an analyte solution. An S-matrix simulation confirms the occurrence of modulations for a reference spectrum (without the antenna) as well as for the resonant antenna spectrum. The effect is enhanced near the antenna resonance due to the increased reflectance of the bottom surface in this spectral region (Fig. 6.7b). The perturbation of the system can be (partially) suppressed by a slightly wedged hydrogel layer or a roughened surface of the hydrogel layer. The latter was realized by treating the slides used as top covers in the fabrication process with fine grinding powder. Profilometric measurements of the dry polymer layer after fabrication indicated a huge impact of the modified covers (Fig. 6.8) and also positively affected the experiments.

The introduced fabrication process enables us to coat our plasmonic nanoantennas with a thin glucose responsive hydrogel layer and allows to experimentally characterize or sensor in the following.

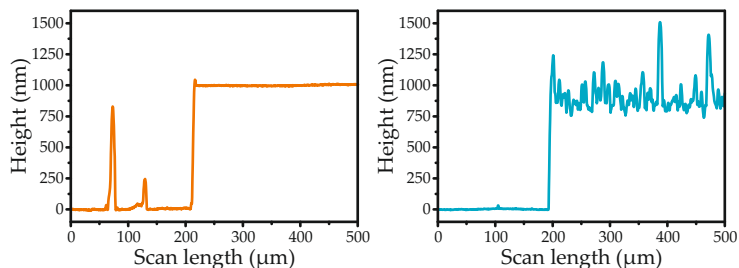


FIGURE 6.8: Height profile of a flat polymer layer and the roughened polymer layer. The rough surface helps to suppress perturbations of the measurement by thin film interference effects.

6.4 CHARACTERIZATION OF THE SENSOR

After an extensive discussion of the hydrogel properties and its fabrication, we will focus on the experiments conducted to determine the properties of our sensor. Therefore, we record transmittance spectra of our samples using Fourier-transform infrared (FTIR) spectrometry and track the resonance position for varying analyte solutions.

For those studies, we fabricated three $100\ \mu\text{m} \times 100\ \mu\text{m}$ arrays of gold nanoantennas on a $10\ \text{mm} \times 10\ \text{mm} \times 0.5\ \text{mm}$ glass substrate. The structures with a length of $310\ \text{nm}$, a width of $60\ \text{nm}$, a height of $40\ \text{nm}$, and a periodicity of $700\ \text{nm}$ in each direction, were written at the center of the substrate by standard EBL (see chapter 3 for details). They exhibit a resonance in the near-infrared spectral region and were coated with a $1\ \mu\text{m}$ thin layer of the hydrogel. The simple nanostructure was chosen due to its easy tunability with respect to resonance wavelength and resonance strength and its reliable, reproducible and fast fabrication. The dimensions arise from a design intended to exhibit a resonance in an "eye-safe" wavelength regime, but not further to the infrared to avoid stronger absorption by the water film. For future experiments, EIT-type or Fano resonances with narrow spectral line width and even higher sensitivity, yet more complex shapes, could also be considered [127].

Liquids in the measurements were handled by the custom-made microfluidic cell introduced in chapter 4. Buffer solution for all measurements was prepared by mixing 2-(cyclohexylamino) ethanesulfonic acid (CHES) (1.555 g, 7.5 mmol) and NaCl (0.707 g, 12 mmol) in 75 ml of DI water. Monitoring the changes with a pH-meter, 1 mol/l NaOH was added until it reached pH 9.0 and the solution was filled up to 100 ml. In case of the studies with proteins, bovine serum albumin (BSA) (3.3 g, 0.05 mmol) was added to the buffer solution.

For the analyte solutions, 180.16 mg of D(+)-glucose was dissolved in 5 ml of buffer solution, subsequently extending it to 10 ml to form a 100 mmol/l glucose solution. All other concentrations, namely 50, 25, 10, 5, 2.5, and 1 mmol/l, were obtained by serial dilution.

Fresh and dry samples were installed into the microfluidic cell and flushed overnight with the first analyte solution to be measured. A constant flow of about 30 $\mu\text{l}/\text{min}$ was ensured by placing a reservoir ~ 20 cm above and the outlet in a beaker 20 cm below the cell.

Appropriate for the spectral region, we choose a CaF_2 beam-splitter and a liquid-nitrogen-cooled mercury cadmium telluride (MCT) detector in the spectrometer setup (cf. chapter 3). Additionally, an infrared polarizer set the polarization of the incident light, and an aperture confined the beam to an area of $\sim 120 \mu\text{m} \times 120 \mu\text{m}$. Reference measurements for normalization were taken prior to every single sample measurement at a point next to the gold nanoantennas, i. e., through cell, hydrogel film, and substrate.

6.4.1 *Response of a Hydrogel Covered Nanoantenna Array*

To investigate not just the total resonance shift, but also its temporal behavior, a spectrum was taken every 30 s during a measurement series with glucose concentrations from 0 mmol/l to 100 mmol/l. The resonance position, evaluated by a centroid detection method (cf. chapter 3), exhibits distinct shifts for every concentration step up to 50 mmol/l, when plotted over time (Fig. 6.9).

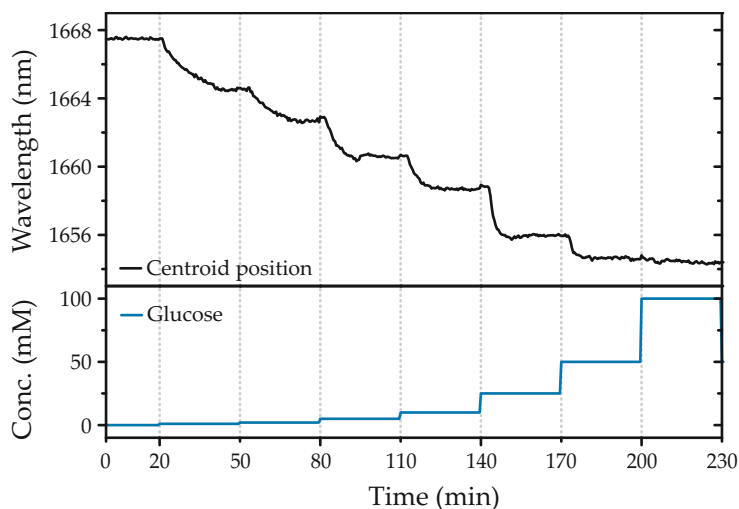


FIGURE 6.9: Temporal evolution of the resonance position (determined by its centroid wavelength) for varying glucose concentrations from 0 mmol/l to 100 mmol/l in the analyte solution.

Extracting the equilibrium positions of the centroid wavelength for all concentrations from the time trace in Fig. 6.9 yields the expected saturation behavior (Fig. 6.10a), as the majority of the boronic acid functionalities in the hydrogel become bound to glucose. When compared to the same glucose concentrations measured on a plasmonic substrate without the hydrogel film, the hydrogel clearly exhibits a much better response to low concentrations. On the bare gold antennas, the refractive index is changed by just the additional glucose molecules in the solution, which leads to only a small signal. In the case of the hydrogel covered antennas, the increasing water content and the relatively high difference of the refractive indices of water and the polymer induce a much more pronounced change. The large shifts for low glucose concentrations, including the physiological range, support the possible application of the sensor for human blood glucose levels. For optimization purposes or other applications, the sensing range can be adapted by smart engineering of the polymer [128].

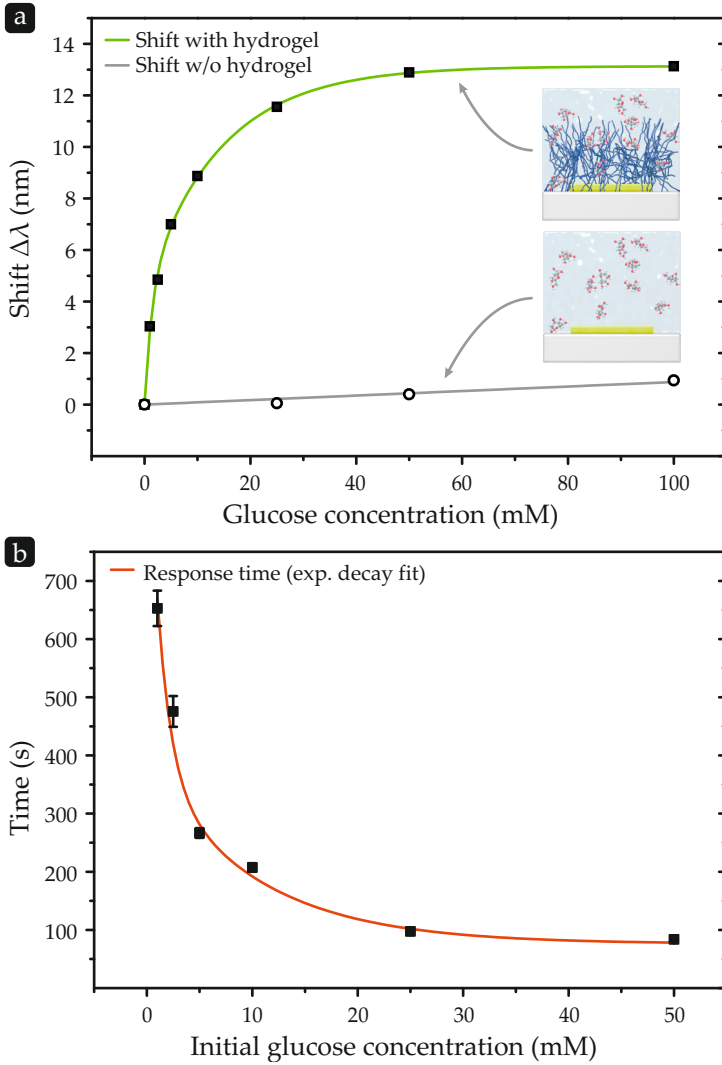


FIGURE 6.10: (a) The centroid wavelength shift $\Delta\lambda$ displays the expected saturation as all functionalized sites in the hydrogel become occupied by glucose molecules. (b) Response times, as obtained from exponential fits to Figure Fig. 6.9, are high for low concentrations, and decrease when more water in the polymer allows for faster diffusion processes at high concentrations.

Fig. 6.9 already indicates that the sensor response time differs for varying concentrations. Therefore, exponential decay curves were fitted to the particular sections of the time trace corresponding to every single glucose concentration. The sudden offset of 0.24 nm after 95 min, attributed to an external disturbance, was compensated for the fit. Fig. 6.10b shows the resulting half-life values, which exhibit a trend inverse to the shift. This can be explained by considering the hydrogel water content in the equilibrium state for varying glucose concentrations. For low values, the polymer contains just a small amount of water, limiting the rate of diffusion of glucose molecules into the film. If there already is some glucose, and hence water, present in the polymer, the transport of new glucose molecules can take place much faster.

To overcome this issue, a pre-swollen hydrogel could be used to particularly favor the important range of small concentration values – yet at the expense of the detectable maximum range. Another possibility is a further reduction of the hydrogel layer thickness. From chapter 5 we know that the enhanced near-fields of gold nanoantennas are confined to a few hundred nanometers around the structures. To still effectively exploit those fields, but at the same time allow for fast diffusion processes and thus for reasonable response times, the polymer layer might be fabricated even thinner. As this is challenging with our current fabrication process, an alternative approach will be discussed in section 6.5.

Because one is generally able to detect shifts when they exceed the noise of the measurement, the detection limit of our sensor can be estimated. Calculating the mean absolute deviation of the measurement data from the exponential fits to Fig. 6.9 gives a noise level for the spectral shift as low as 0.1 nm. Linear extrapolation of the values for 2.5 mmol/l and 1 mmol/l glucose relates to a concentration of 0.05 mmol/l at 0.1 nm shift. Hence, the approximated limit of detection is a concentration of 50 μ mol/l.

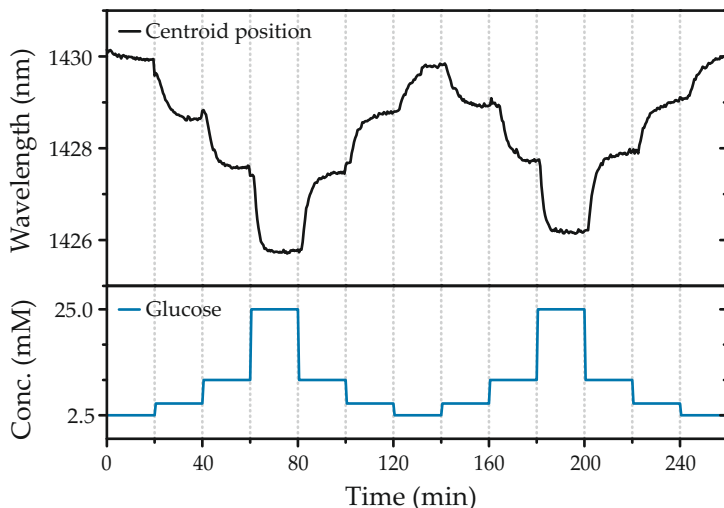


FIGURE 6.11: All involved processes are reversible and allow for continuous measurements, without any flushing or regeneration between different concentrations. After two cycles with varying glucose concentrations between 2.5 mmol/l and 25 mmol/l the centroid position shifts back to its initial value.

6.4.2 Investigation of Hydrogel Degradation

Another advantage of this chemistry is the reversibility of all the sensing processes. Since the reaction between glucose and the phenylboronic acid quickly reaches a dynamic equilibrium, and water can get in and out of the hydrogel freely, changes in the glucose concentration in the overlying fluid quickly result in changes in the water content of the hydrogel. The polymer itself is tightly bound to the substrate, and the gold antennas are not part of any chemical processes, and so the sensors are stable. Hence, the plasmonic resonance wavelength reversibly shifts back to the original value (Fig. 6.11).

In the measurement, two full cycles with glucose concentrations ranging between 2.5 mmol/l and 25 mmol/l could be achieved, without any flushing or regeneration steps needed in-between. The still visible slight redshift in the second cycle

has to be included in investigations regarding long-term stability of the sensor. As a redshift of the resonance corresponds to an increasing refractive index, disintegration or delamination of the polymer layer can already be excluded at this point.

6.4.3 *Other Influences on the Sensor*

A distinct and clear response of a sensor to a desired analyte, as we have demonstrated above, is the basis of a good sensor. Anyhow, also the influence of other substances is a key point in sensor development. Ideally the sensor response is solely limited to one specific analyte, while in reality very often cross sensitivities play a crucial role and require special attention. In principle, such investigations always have to be carried out with regard to a particular application and the substances present in this context. Even though the border is blurred in the realm of biological sensing we will distinguish between environmental influences and other possible analyte molecules.

Environmental influences are, for example, temperature, humidity and pressure. While humidity can be neglected when working with aqueous analyte solutions, additional parameters like pH and ionic strength of the solution might get important. As our sensor is based on the formation of a charged complex with an acid, both dependences are crucial in this case and have therefore been measured.

For this study, analyte solutions with a fixed glucose concentration of 10 mmol/l were prepared with varying pH and ionic strength (represented by NaCl concentration). In Fig. 6.12 the centroid wavelength shift for pH values between 7.4 and 9.5 is plotted (blue line). The lower limit of 7.4 has been chosen as it is very common in physiological processes. Obviously, the pH value confirms its expected strong influence on the hydrogel swelling. Because a resonance redshift corresponds to a more dense hydrogel, it can be concluded that for lower pH values the response to glucose decreases. This can be explained with the help of the reaction equation between glucose and the PBA (cf. Fig. 6.4). For low pH values the equilibrium is shifted to the left side, favoring the undissociated state of the PBA. Despite

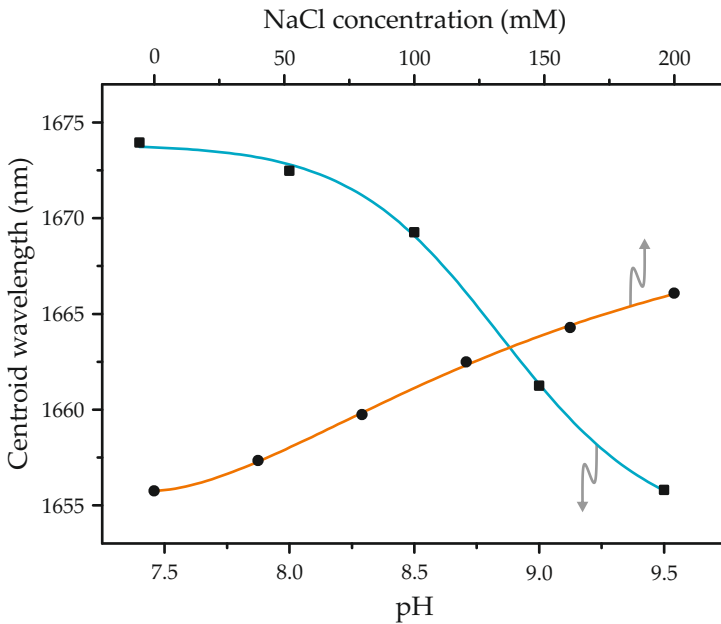


FIGURE 6.12: Dependence of the hydrogel response on pH value (blue) and ionic strength (orange) of the analyte solution. For lower pH values the undissociated state of the PBA is more favorable, the swelling for a given glucose concentration decreases, and consequently leads to a redshifted centroid wavelength. At lower ionic strength values the impact of the ionized PBA/glucose complex on the Donnan potential is higher. Hence the swelling for a given glucose concentration increases, leading to a blueshift of the centroid wavelength.

the presence of glucose, there is no reason for the hydrogel to swell. If the equilibrium is, in contrast, shifted to the right side by high pH values, the PBA will become deprotonated even without the presence of glucose. Hence, the hydrogel will be already swollen, hampering further swelling on glucose exposure. Consequently there is an optimal pH range around pH 9.0. It is related to the acid dissociation constant and can be adjusted by using different PBA species.

The data points for different NaCl concentrations depicted in Fig. 6.12 (orange line) reveal a blueshift, and hence a more

pronounced swelling, for lower values. This can be attributed to the higher impact of the ionization of the PBA on the Donnan potential in an environment with less overall ionic strength. In the next section we will explore the capability of the hydrogel to filter large proteins.

6.4.4 *Filtering Capabilities of the Hydrogel*

In more application related environments, proteins are one of the main issues a sensor of this type will need to deal with. To simulate such a less clean sensing environment, we intentionally contaminated our analyte solutions with 0.5 mmol/l albumin. This protein has a molecular weight of approximately 66 kDa, and is also present in the human organism at similar concentrations. For safety reasons, BSA was used in the experiments. To demonstrate the specificity of the hydrogel layer, measurements were carried out on two otherwise identical samples, with just one of them coated with the hydrogel film. Because of the small glucose signal on the bare gold antennas (see Fig. 6.10a), the glucose concentrations in the analyte solutions were increased by a factor of four for the experiment on the respective sample, so that clear visibility of the single steps is maintained.

Without the hydrogel layer, the bulky protein molecules, as expected, produce a large shift of the signal (Fig. 6.13a). Although the concentration of BSA is much lower than that of glucose (0.5 mmol/l compared to 10 mmol/l to 100 mmol/l), the signal induced by the protein exceeds the shift caused by glucose because of the ratio of about 370:1 of their molecular weights. Furthermore, the sticky protein covers the plasmonic structures and prevents the resonance from returning to its initial position when changing back to pristine solutions without BSA. The hydrogel, in contrast, prevents the macromolecules from entering the sensitive area around the gold antennas, and is still able to expand and contract as the glucose concentration changes to allow for clear readings of the injected glucose concentrations.

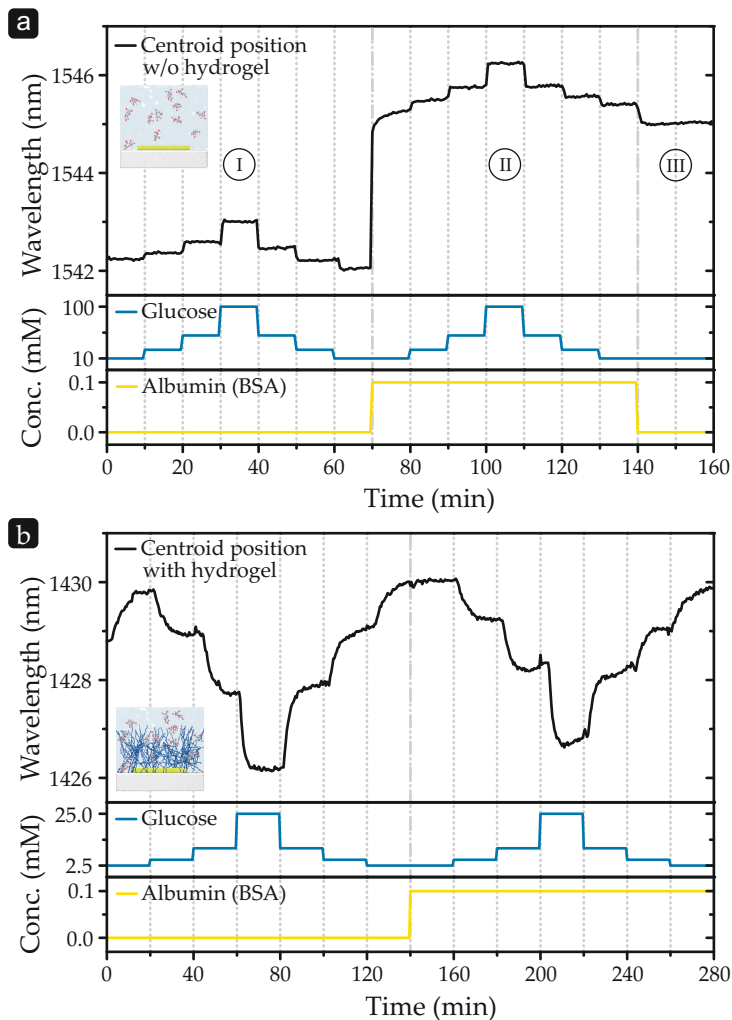


FIGURE 6.13: (a) Without the hydrogel film, the large and sticky (BSA) proteins cause a large shift (transition region I to II), which does not recover when returning to clean glucose solutions (region III). (b) By adding a 1 μm thick layer of hydrogel on top of the gold nanoantennas, the proteins can be kept out of the sensitive region around the plasmonic structures and glucose concentrations can be detected without major disturbances.

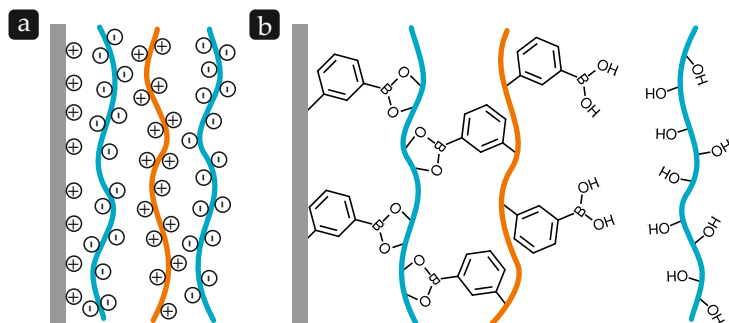


FIGURE 6.14: Different layer-by-layer assembly systems. (a) Two oppositely charged polymers are alternately adsorbed on a substrate. Linking is established by electrostatic attraction. (b) The two polymers are linked by reversible covalent bonds between hydroxide moieties and a phenylboronic acid.

6.5 LAYER-BY-LAYER GROWTH FOR ULTRATHIN FILMS

During the characterization of our hydrogel coated plasmonic nanoantenna arrays in the last section we have seen that a hydrogel layer thickness of $1\ \mu\text{m}$ still leads to slow response times, particularly for low glucose concentrations. From the extent of the localized electric fields discussed in chapter 5 it can be deduced that even thinner layers could be used without losing much signal. We therefore explore the technique of layer-by-layer (LbL) assembly of polymers to fabricate glucose responsive hydrogel films with possible thicknesses ranging from a few nanometers to several hundreds of nanometers [129, 130].

The LbL approach is usually based on a cyclic process where two oppositely charged polymers are alternately adsorbed on a substrate. In a simple model, each layer is bound to the previous layer by electrostatic attraction and, at the same time, changes the surface charge to allow for adsorption of the next layer (see Fig. 6.14a). In between the steps, residual material is removed by washing. The samples can be sequentially ex-

posed to the different materials by various methods, such as immersion, spin-coating or spraying [131].

A similar system, schematically depicted in Fig. 6.14b, can be built exploiting the covalent reversible interaction of a PBA with the hydroxide groups of polyvinyl alcohol (PVA). For that purpose, the PBA is incorporated into polyacrylamide (PAAm) to form poly[acrylamide-co-3-(acrylamido)-phenylboronic acid], which we will hereafter refer to as P(AAm-AAPBA). Subsequently, a multilayer system can be assembled by linking P(AAm-AAPBA) layers with PVA via their PBA functionalized sites. If glucose diffuses into the system it interacts with the PBA, breaking some of the bonds to PVA. Hence, the linking between the layers is loosened and the hydrogel swells (cf. Fig. 6.4).

The synthesis of the copolymer, fabrication of the LbL structure and its experimental characterization will be part of this section.

6.5.1 *Synthesis*

As PVA is commercially available with almost arbitrary molecular weight, only P(AAm-AAPBA) has to be taken care of. Besides the introduction of an acrylic acid moiety to APBA, formation of the copolymer is necessary.

In this case, we used an alternative process to synthesize AAPBA, which allows to avoid the use of tetrahydrofuran as a solvent [132]. APBA (5 g, 36.5 mmol) was dissolved in NaOH solution (73 ml, 2 mol/l) in a round bottom flask. The mixture was cooled in an ice bath and cold acryloyl chloride (5.9 ml, 73 mmol) was added dropwise to the vigorously stirred mixture over 15 min. HCl solution (1 mol/l) was slowly added until the pH reached 1.0. A white solid precipitated and was washed with cold water. The filtrate was extracted with ethyl acetate three times. Afterwards, the organic phase was washed with brine and the solvent was removed by rotary evaporation. The resulting white solid was combined with the previously filtered material and recrystallized in H₂O for purification. Again, ¹H NMR spectroscopy was used to verify the synthesized product.

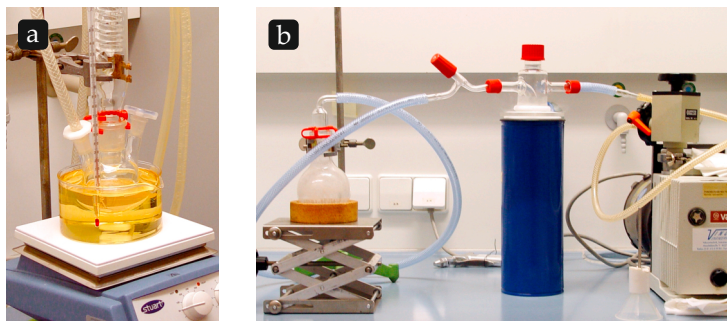


FIGURE 6.15: (a) Polymerization is carried out in a heated round bottom flask, equipped with a condenser and a nozzle for nitrogen purging. (b) The product is dried under vacuum conditions with the solvent being collected in a cold trap.

P(AAm-AAPBA) was synthesized by free radical polymerization [133]. For this purpose, acrylamide (1.352 g, 19.0 mmol), AAPBA (0.19 g, 1.0 mmol), and 2,2'-azo-bis-isobutyronitrile free radical initiator (10.0 mg, 61 μmol) were dissolved in dimethylformamide (40 ml). The reaction was carried out in a round bottom flask equipped with a condenser and a nozzle for continuous nitrogen purging (see Fig. 6.15a). After 30 min of nitrogen bubbling to remove dissolved oxygen, the mixture was heated to 70 $^{\circ}\text{C}$ to start the polymerization. It was allowed to continue for 24 h and the product was precipitated in acetone, filtered, and washed three times with acetone. Afterwards it was dried under vacuum conditions, while the solvent was collected in a cold trap (see Fig. 6.15b).

6.5.2 Layer-by-layer Growth

Following the synthesis of the necessary polymer constituents, 10 mm \times 10 mm \times 0.5 mm glass slides were prepared for the LbL assembly process. Therefore, several 100 μm \times 100 μm arrays of gold nanoantennas were fabricated using EBL. The substrate surface was modified with amino groups by immersing them in a 1 wt% solution of (3-Aminopropyl)triethoxysilane in

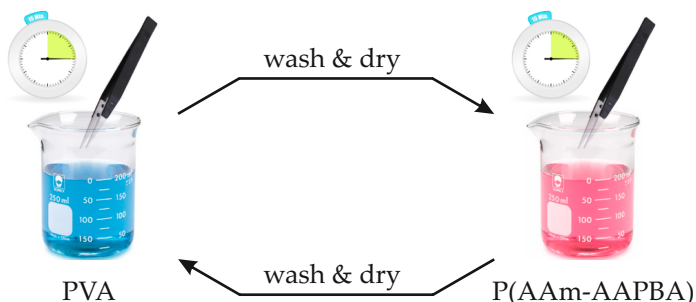


FIGURE 6.16: Immersion process for layer-by-layer fabrication of ultrathin films. The sample is alternately submerged in a solution of PVA and P(AAm-AAPBA) for 15 min to assemble a layer of the respective polymer. In between, loosely bound components are removed by washing and drying the sample. The process is repeated until the desired number of bilayers is reached.

toluene over night with subsequent washing with toluene and drying. A precursor layer of polyacrylic acid was introduced by soaking the samples in a 0.1 wt% aqueous solution at pH 3.0 for 10 min and washing them with water. PBA groups were then added in an aqueous solutions of APBA (7.5 mmol/l) and 1-(3-dimethylaminopropyl)-3-ethylcarbodiimide hydrochloride (12.5 mmol/l) for 4 h.

For the cyclic assembly process of the single layers, two solutions containing 0.1 wt% of PVA (molecular weight M_w between 13 000 and 23 000) and P(AAm-AAPBA), respectively, were prepared in 50 mmol/l phosphate buffered saline (PBS) at pH 8.5. Starting with PVA, the sample was alternately submerged in the solutions for 15 min, withdrawn, rinsed in fresh PBS to remove loosely bound polymer, and dried in air [133]. The process is illustrated in Fig. 6.16 and is repeated until the desired number of bilayers has formed.

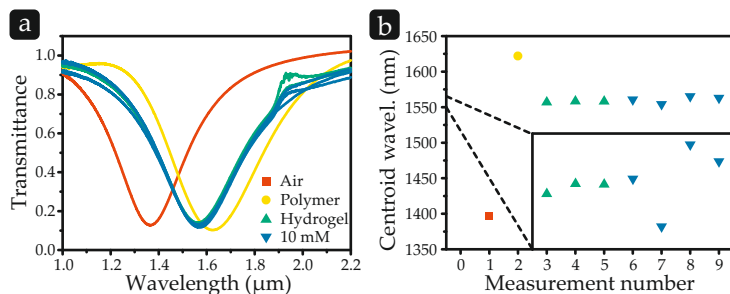


FIGURE 6.17: (a) Infrared spectra of the plasmonic resonance after fabrication (air), polymer multilayer assembly (polymer), immersion in buffer solution (hydrogel), and on exposure to 10 mmol/l glucose solution. (b) The evaluated shifts are consistent with the expected behavior, and suggest successful growth of the hydrogel layer. Apart from that, no response to glucose can be observed.

6.5.3 Characterization

The technique of LbL assembly of ultrathin layers was used to produce two samples, which will be characterized by FTIR measurements in the following. Therefore, plasmonic gold nanoantennas were fabricated by EBL, with the identical procedure and dimensions as used for the bulk hydrogel experiments in section 6.4. A nominal length of 310 nm, a width of 60 nm, a height of 40 nm, and a periodicity of 700 nm in each direction, again yielded a well modulated resonance in the near infrared spectral region. Each substrate was treated complying with the recipe specified above until 20 bilayers were reached. Again, the microfluidic cell introduced in chapter 4 was used to guide the liquids to the nanostructured area. The polymer was removed around the nanostructures to render reliable sealing between substrate and the silicone pieces of the cell possible. An analyte solution was prepared based on 50 mmol/l PBS at pH 8.5, containing 10 mmol/l of glucose. Because of the same spectral region, also the spectrometer setup was adopted from the previous experiments.

To monitor the single steps, spectra were taken after all major changes. The obtained spectra are plotted in Fig. 6.17a. A first measurement was conducted on the just fabricated nanostructures surrounded by air. The large spectral shift going along with the subsequent polymer assembly suggests a successful growth process, considering the refractive index of the polymer ($n_{\text{polymer}} > n_{\text{water}} > n_{\text{air}}$). Likewise consistent with the expected behavior is the resonance shift back to shorter wavelengths as the polymer gets soaked with water and becomes a hydrogel. However, a shift for the 10 mmol/l glucose solution can not be detected. Although analysis by means of the centroid evaluation method does allow to track small variations of the resonance position, a clear trend can not be observed. Furthermore, the fluctuations of the resonance shift here are much higher than with the bulk hydrogel at the beginning of this chapter. Anyway, as the response of such systems to glucose has been demonstrated [133], further chemical modifications are expected to resolve this issue. Besides the general challenge of establishing a chemical process in a new environment, the reasons might also be found in the exact composition of the particular hydrogel. As reported by Zhang et al., a similar polymer, containing more PBA functionalities, swells by 165% upon immersion in water [134]. This indicates that the polymer is already quite dilute in the initial state. While it is still able to swell further on glucose exposure, the process does not entail a notable refractive index change. A possibility to overcome this limit, might be found in careful chemical engineering, which results in the development of a polymer system particularly suited for this type of sensors.

6.6 SUMMARY & NONINVASIVE TEAR GLUCOSE SENSING

A layer of functionalized hydrogel has been used to coat an array of gold nanoantennas to provide a plasmonic sensor for glucose molecules. The hydrogel polymer contains a phenylboronic acid, which reacts with the glucose molecules and leads to an effective refractive index change of the hydrogel, due to the resultant increase in the water content of the hydrogel.

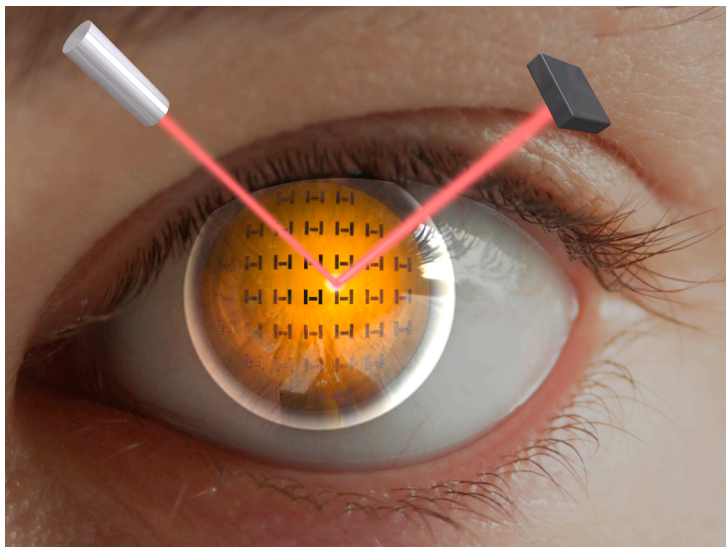


FIGURE 6.18: Artistic picture of a contact lens used for noninvasive glucose sensing. The changes in the optical spectrum of a functionalized hydrogel coated plasmonic structure upon exposure to different glucose concentrations is monitored by the reflected intensity of a laser beam. Image: S. Hein

When detecting the changes via investigation of the plasmon resonance shift, a clear signal is revealed in comparison to the changes induced by the glucose molecules alone. This allows for concentrations in the physiological range to be measured. Furthermore, the temporal behavior of the system was analyzed as well as the reversibility of the process. The influence of proteins on the measurement was studied with the results suggesting the polymer is able to suppress negative effects.

Similar types of experiments have been carried out using other techniques, for example, surface plasmon resonance spectroscopy (SPR) or quartz crystal microbalances (QCM) [135–137]. While the examined sensing ranges are mostly comparable, our concept provides the additional benefit of a simple contactless optical setup, a sensing area down to the single particle level, and the inherent filtering properties of the hydrogel.



FIGURE 6.19: Simplified setup for the demonstration of the noninvasive glucose sensing approach. The transmitted/reflected intensity of a low power near-infrared laser is recorded by silicon photodiodes, electronically processed and can be read out via USB to be displayed on a tablet computer.

The biocompatibility of the hydrogel and gold nanostructures also encourages a future application in medical devices, such as purely passive contact lenses (which are often hydrogel-based) for non-invasive glucose sensing in the tear liquid. The idea is schematically illustrated in Fig. 6.18. A low power infrared laser is used to monitor the spectral changes in the reflectance of a functionalized hydrogel coated plasmonic nanostructure. For this purpose, a phenylboronic acid even more specifically reacting with glucose at physiological pH values, such as presented by Alexeev et al., could be used [138].

To facilitate this application, our research was partly funded through the project *Noninvasive measurement and analysis of glucose levels of diabetes patients using metamaterials*, in the *Ideenwettbewerb Biotechnologie und Medizintechnik* of the Ministerium für Wissenschaft, Forschung und Kunst Baden-Württemberg. In

this context, we developed a simplified setup to demonstrate the concept (see Fig. 6.19), including liquid handling as well as optical readout and electronic signal processing. Instead of taking a whole spectrum and determining the resonance shift, only the change in the reflected/transmitted intensity in the narrow spectral range of a laser is tracked. The signal is recorded by standard silicon photodiodes and processed by integrated electronics. A USB connection provides power to the system and can be used to display the signal on a workstation or tablet computer.

In summary, the combination of plasmonic structures with functionalized hydrogels appears to provide an interesting paradigm for biosensing and extends the pool of options to adapt plasmonic sensors to the needs of different applications.



GLUCOSE SENSING WITH SEIRA

In the previous chapter we have seen that chemical functionalization is an essential part of many kinds of sensors for recognition of a specific analyte. Though substantial, it is often one of the most complex elements of a system as it involves selective, preferably reversible, biomolecular binding reactions between an analyte and an immobilized molecule on the sensor surface. Another possibility is to directly identify analytes by their physical properties. One particularly suited property are molecular vibrations. Those vibrations occur when the atoms in a molecule move periodically with respect to each other and can be excited with electromagnetic waves in the infrared range [57]. As the exact frequencies of different vibrations depend crucially on the constituent atoms and their configuration, their knowledge can help to distinguish different substances by their infrared absorption spectra. This technique is widely used in various fields of research, industry and applications like, for example, structural investigation of chemical compounds, monitoring of processes, and identification of substances in the areas of health, safety, food and forensic science [139, 140].

The absorption cross-section of this process is, however, rather small and long optical paths are necessary. Anyhow, it has been shown that it can be enhanced by the strong localized electric fields in the vicinity of resonantly excited plasmonic nanoantennas by more than five orders of magnitude, introducing the concept of surface enhanced infrared absorption (SEIRA) [35, 141, 142].

In the following we investigate this method applied to the detection of glucose. Compared to chapter 6 where we relied on the shift of a plasmonic resonance in the presence of glucose, we now expect an additional feature, related to the absorption of the molecules, on top of the plasmonic resonance

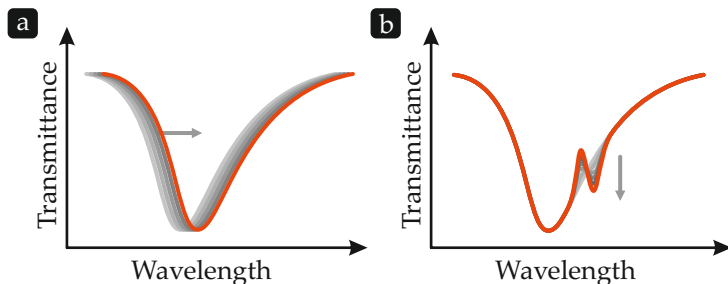


FIGURE 7.1: (a) In plasmonic refractive index sensing the signal is based on a shift of the plasmonic resonance. (b) In surface enhanced infrared absorption the signal arises as an additional feature on top of the broad plasmonic resonance.

(cf. Fig. 7.1). The asymmetric line shape arises from the resonant coupling of the molecular vibration and the plasmonic excitation.

7.1 MEASUREMENT OF HIGH CONCENTRATIONS

A first measurement was carried out in transmission on an existing sample with antennas resonant at 1750 cm^{-1} . A drop of 100 mmol/l glucose solution was applied to the sample surface and was subsequently allowed to dry. The resulting Fourier-transform infrared (FTIR) spectrum (Fig. 7.3) exhibits the broad plasmonic resonance at 1750 cm^{-1} with weak absorption features on its right side. Those signals, denoted by red arrows, can be attributed to the glucose absorption bands at 1460 cm^{-1} , 1378 cm^{-1} , and 1347 cm^{-1} (cf. Fig. 7.2).

In order to further investigate the behaviour, we designed several plasmonic antennas with resonances between 1000 cm^{-1} and 1500 cm^{-1} using S-matrix simulations and fabricated arrays of them on a CaF_2 substrate by electron beam lithography (EBL). CaF_2 was used due to its transparency in the infrared wavelength range.

Because we intended to detect glucose in aqueous solutions, we adapted our measurements in several ways. To cleanly

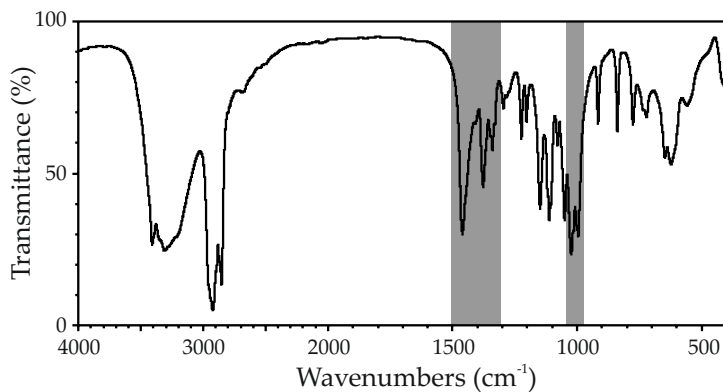


FIGURE 7.2: Infrared transmittance spectrum of D-glucose. Source: Spectral Database for Organic Compounds, National Institute of Advanced Industrial Science and Technology, Japan

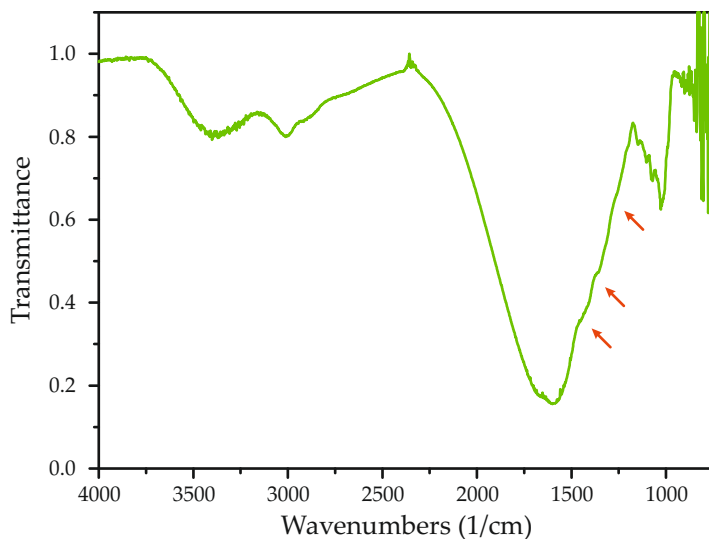


FIGURE 7.3: SEIRA measurement of a dried glucose film. It exhibits the broad plasmonic resonance with weak absorption features on its right side (denoted by the red arrows).

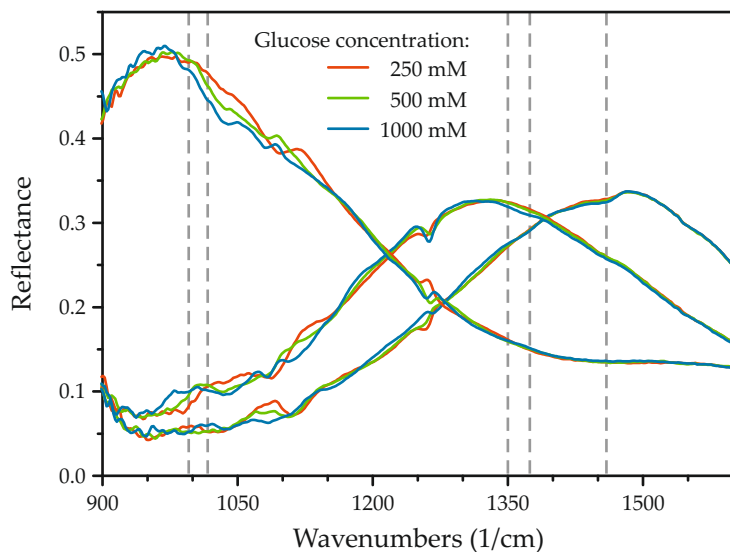


FIGURE 7.4: SEIRA measurement of aqueous analyte solutions containing high concentrations of glucose. The vertical dashed lines indicate positions of absorption bands of glucose. No clear signals can be identified for any of the antenna arrays.

handle the fluids, we used the microfluidic cell described in chapter 4. Furthermore, as water is quite absorptive in this wavelength range, we switched from transmission to reflection measurements and measured from the rear side of our sample. Considering the weak signals in the first measurement, we prepared and measured three analyte solutions with glucose concentrations of 250 mmol/l, 500 mmol/l and 1000 mmol/l. The corresponding spectra are plotted in Fig. 7.4. The vertical dashed lines denote positions of pronounced spectral features of glucose, according to Fig. 7.2. Despite the, in comparison to the hydrogel functionalized glucose sensor (cf. chapter 6), rather high glucose concentrations, there is no clear and unambiguous signal for any of the investigated antenna arrays.

In the next two sections we will therefore estimate the signal that can be expected for aqueous glucose solutions and discuss possible approaches for improvement.

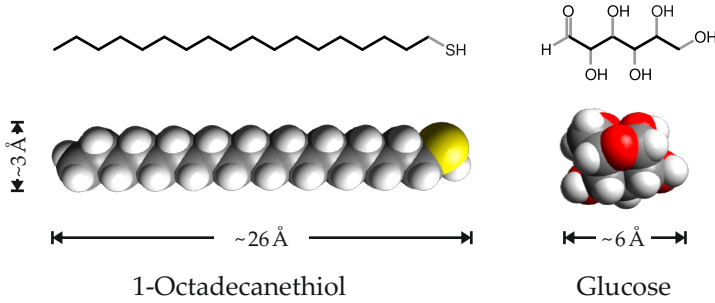


FIGURE 7.5: Structure, van der Waals surfaces, and dimensions of octadecanethiol and glucose molecules.

7.2 ESTIMATION OF THE SIGNAL STRENGTH

In order to estimate the SEIRA signal of a aqueous glucose solution, we compare our experiment to work of Neubrech et al. where the detection of a self-assembled monolayer of octadecanethiol (ODT) on a plasmonic nanoantenna is demonstrated [35]. The structural formulas and van der Waals surfaces for the alkanethiol ODT and glucose molecule are depicted in Fig. 7.5. For our calculation we consider a typical gold antenna with a top surface of $1500 \text{ nm} \times 80 \text{ nm}$. In a self-assembled monolayer of alkanethiols the typical surface area per molecule is 21.6 \AA^2 [143]. Hence, the number of molecules in a monolayer on top of the antenna is approximately

$$N_{\text{ODT}} = \frac{A_{\text{Antenna}}}{A_{\text{Molecule}}} \approx 5.5 \cdot 10^5. \quad (7.1)$$

Furthermore, the molecules in the monolayer are tilted with respect to the surface normal by 30° [143], which yields a layer height of roughly 23 \AA [144]. We now calculate the number of glucose molecules in the same volume as taken up by the ODT molecules, assuming a glucose concentration of 100 mmol/l . The concentration is chosen as it corresponds to the highest value used for the hydrogel functionalized plasmonic sensor. Using the Avogadro constant N_A , we obtain

$$N_{\text{Glucose}} \approx 1.7 \cdot 10^4. \quad (7.2)$$

Additionally, we have to consider the number of bonds per molecule possibly contributing to the signal. For reasons of simplicity, we assume a strong C–H stretch mode and include all bonds, neglecting their different environment. This gives a total of 37 C–H bonds for ODT and 7 for glucose. Multiplying with the number of molecules yields a ratio of approximately 170 : 1. This indicates that the signal of 100 mmol/l glucose solution is about two orders of magnitude lower, than the signal of a monolayer ODT and will not be detectable with this method without further modifications.

7.3 POSSIBLE APPROACHES FOR IMPROVEMENT

The measurements and estimation of the signal strength revealed that, despite the field enhancement around the plasmonic antennas, a 100 mmol/l aqueous solution of glucose is too diluted to yield a suitable signal. Here we will present two possible ways for further improvement, yet at the cost of higher complexity.

The first approach is based on functionalization of the gold antennas in order to accumulate glucose molecules in the areas of highest field enhancement. For this purpose, we make use of the interplay of glucose with phenylboronic acid (PBA) as introduced in Fig. 6.4. The PBA is in this case modified with a thiol group to be immobilized on the surface of the gold antenna [145]. When the glucose molecules in the solution interact with the stationary PBA, they might concentrate around the antenna, leading to an increased signal. A proof of concept measurement exploiting this method was not successful. To further pursue this idea, a closer examination of the functionalization chemistry is necessary. Nevertheless, the additional vibrational bands of the functionalization molecules and the still lower signal from glucose in comparison to ODT could hamper the success of this procedure.

Another potential concept relies on the application of the functionalized hydrogel introduced in chapter 6 to the SEIRA sensor. Coating the plasmonic antennas with this hydroxyethyl-methacrylate (HEMA) based polymer will, owing to the large

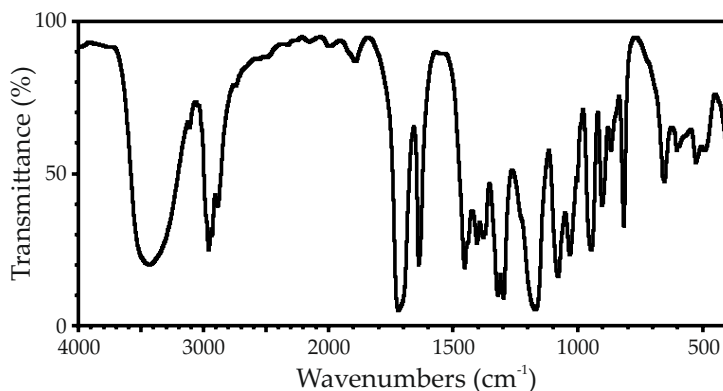


FIGURE 7.6: Infrared transmittance spectrum of hydroxyethyl methacrylate. Source: Spectral Database for Organic Compounds, National Institute of Advanced Industrial Science and Technology, Japan

number of identical molecules, lead to a strong signal. Although the variety of vibrational bands of the polymer, illustrated in Fig. 7.6, will certainly mask those of glucose, they could still give rise to a distinct signal. When the polymer swells in the presence of glucose, two effects occur that might cause a detectable signal. One is the movement of the spectral position of vibrational bands due to stretching of the polymer chains, accompanied by a change of the environment of the involved atoms. The more prominent effect is, however, the decrease of the effective polymer content in the sensing volume as it gets soaked with more water. As a consequence this will lead to a smaller absorption amplitude, which could, for example, be detected at the strong C=O stretch mode at around 1720 cm^{-1} .

Anyhow, both of the suggested improvements will nullify the intrinsic advantage of direct identification of substances by infrared spectroscopy. It remains therefore unclear, if SEIRA can prove its applicability for detection of small molecules in solutions.

Nonlinear effects and sensing have both been active fields in the area of plasmonics and nanooptics. While research on nonlinear plasmonics is mainly focused on the fundamental understanding of the underlying microscopic processes and how to enhance the generation of higher harmonic light [28, 146–153], the concept of linear plasmonic sensing already moves toward applications [71, 92]. Consequently, experiments deal with application-related topics such as large area fabrication [101–103], efficient analyte delivery [104, 154], optimization of the structures with respect to sensitivity [100, 155, 156], and different functionalization methods for specific analytes [105–111]. In plasmonic refractive index sensing narrow line width and hence steep slopes are desirable to track even small changes. Since plasmonic resonances are usually rather broad, due to radiative and ohmic losses, this is a pertinent point for improvement. An already exploited possibility is to employ dark or subradiant modes, as demonstrated with various types of Fano resonances and the plasmonic analog of electromagnetically induced transparency (EIT) [93, 94, 127]. However, experiments in nonlinear plasmonics show that the third harmonic (TH) spectrum of a plasmonic antenna is also spectrally narrower than the linear plasmon resonance. The narrowing in this case is caused by the third-order dependence of the signal on the incident light intensity. These findings suggest that a nonlinear plasmon sensor exhibits a higher sensitivity, which shall be explored in the following.

In general, plasmonic sensors can be used in different ways: First, they can be used as refractive index sensors for bulk surroundings. For example, a liquid surrounds the plasmonic nanoantenna and changes its index. This will shift the plasmonic resonance of the antenna. Second, the refractive index of the antenna itself could change, for example when filling a

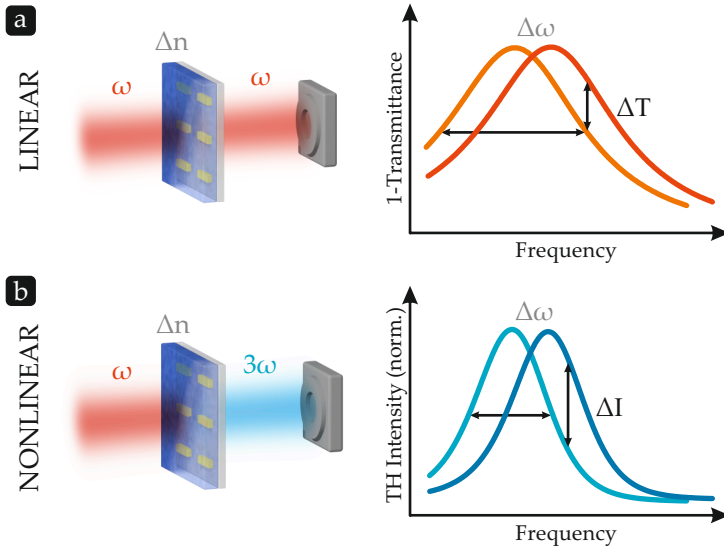


FIGURE 8.1: Principle of linear and nonlinear plasmonic sensing. A refractive index difference Δn in the environment of plasmonic nanostructures causes a shift of their resonance frequency. (a) In the linear configuration, the transmittance difference ΔT upon excitation at a given frequency ω is tracked as the sensor signal. (b) In nonlinear sensing, the plasmonic resonance is driven at frequency ω and the resonantly enhanced third harmonic at frequency 3ω serves as the sensor signal. Due to the narrowing of the TH resonance caused by the nonlinear process, a larger signal ΔI can be expected.

palladium nanoantenna with hydrogen, causing formation of PdH which has a different refractive index than Pd. This also will lead to a shift of the antenna resonance. Third, on the surface of the plasmonic antenna, a layer of molecules could be attached which can act as molecular detector for binding-specific target molecules. When such binding-specific molecular recognition happens, also the refractive index of the surrounding medium changes, as the electric field enhancement is highest in the first few nanometers around the antenna [142].

In the linear sensing configuration, light at a frequency ω is routed through the analyte-covered nanoantennas and the

transmitted or absorbed intensity at the same frequency is measured (Fig. 8.1a). A change in the refractive index of the analyte Δn causes a resonance shift $\Delta\omega$, which directly leads to the detected intensity difference ΔT at frequency ω . Alternately, the shift $\Delta\omega$ of the resonance itself can be tracked, but this requires recording the entire spectrum. The nonlinear configuration introduced here relies on the same fundamental principle, but probes the resonance shift through generated light intensity at the third harmonic frequency 3ω (Fig. 8.1b). As this light is created through a nonlinear optical process, its intensity crucially depends on the incident intensity on the nanoantennas at the fundamental frequency [43]. Consequently, the shape of the linear absorbance spectrum is even more pronounced for the third harmonic intensity spectrum and the detectable relative intensity difference $\Delta I/I$ should be larger.

Our sensor signals are therefore given as

$$s_L = \frac{\Delta T}{T_1} = \frac{T_2}{T_1} - 1 \quad \text{and} \quad s_{NL} = \frac{\Delta I}{I_1} = \frac{I_2}{I_1} - 1, \quad (8.1)$$

with $\Delta T = T_2 - T_1$ and $\Delta I = I_2 - I_1$ for the linear and nonlinear sensor signals, respectively.

In the next sections we introduce a model that describes the nonlinear response of our system, followed by a detailed discussion of the mathematical predictions. Subsequently, we characterize our samples experimentally by nonlinear spectroscopy, and perform an application related sensing experiment, comparing the linear and nonlinear sensing configuration.

8.1 THE ANHARMONIC OSCILLATOR MODEL

In the previous section, we introduced our concept of nonlinear plasmonic sensing and gave an intuitive description of the expected enhancement. To make a more quantitative prediction of what to expect, we model our system by an anharmonic oscillator. Here, the plasmon is treated as a classical harmonic oscillator with a small third-order perturbation. Despite its simplicity, this model has already proven its accuracy when applied to third harmonic spectra of plasmonic nanoan-

tennas [23, 157, 158]. In this chapter, we are going to describe the anharmonic oscillator model in detail and derive an expression for the experimentally accessible quantities of linear absorbance A and generated third harmonic intensity I , respectively.

The model is based on the Lorentz oscillator model discussed in section 2.1. Yet, for high external electromagnetic fields, the assumption of a harmonic potential for the oscillating electrons is not justified anymore. Therefore, we include higher order terms in the binding potential of the electrons $V(x)$:

$$V(x) = \frac{1}{2}m_e\omega_0^2x^2 + \frac{1}{4}m_eax^4 \quad (8.2)$$

As we are interested in third order nonlinear effects, according to section 2.3 we omit the term of third order in the displacement of the electron x and only add an extension term of fourth order. Hence, the potential remains symmetric and we get a term proportional to x^3 in the corresponding differential equation

$$\ddot{x}(t) + 2\gamma\dot{x}(t) + \omega_0^2x(t) + ax(t)^3 = -\frac{e}{m_e}E(t) \quad (8.3)$$

where the coefficient a is related to the strength of the anharmonicities in the potential $V(x)$. Because there is no analytical solution for this equation, we solve it by means of perturbation theory and start with the ansatz

$$x(t) = x^{(0)}(t) + ax^{(1)}(t) + \dots \quad (8.4)$$

If it is inserted into eq. 8.3 the differential equation of the anharmonic oscillator can be split into two equations containing the terms being of the same order of a :

$$a^{(0)} : \ddot{x}^{(0)}(t) + 2\gamma\dot{x}^{(0)}(t) + \omega_0^2x^{(0)}(t) = -\frac{e}{m_e}E(t) \quad (8.5)$$

$$a^{(1)} : \ddot{x}^{(1)}(t) + 2\gamma\dot{x}^{(1)}(t) + \omega_0^2x^{(1)}(t) = -[x^{(0)}(t)]^3 \quad (8.6)$$

The differential equation of zeroth order is equivalent to the unperturbed Lorentz oscillator (cf. eq. 2.15). From section 2.1 we already know the solution in frequency domain to be:

$$x^{(0)}(\omega) = -\frac{e}{m_e}g(\omega)E(\omega) \quad (8.7)$$

with $g(\omega) = -(\omega^2 - \omega_0^2 - 2i\gamma\omega)^{-1}$ which we related to the first order susceptibility in eq. 2.17.

Before solving the equation of first order in a , we want to derive an expression for the linear absorbance A from the current result. For that purpose, we consider the intensity of a plane wave $E(z) = E_0 e^{-ikz}$, using eqs. 2.13 and 2.18, and compare it to Beer's law, which expresses the attenuation of electromagnetic waves in a medium in terms of the attenuation coefficient α [41]:

$$I(z) = I_0 e^{-2\kappa \frac{\omega}{c} z} = I_0 e^{-\alpha z}. \quad (8.8)$$

If we additionally apply eq. 2.18, this leads to

$$\alpha = 2\kappa \frac{\omega}{c} \approx \frac{\omega}{c} \Im \left[\chi^{(1)} \right]. \quad (8.9)$$

Furthermore, we can express the absorbance A in terms of intensities

$$A(z) = \frac{\Delta I(z)}{I_0} = 1 - \frac{I(z)}{I_0} = 1 - e^{-\alpha z} \approx \alpha z \propto \alpha \quad (8.10)$$

where a Taylor expansion was used to estimate the exponential function in the end. Inserting eqs. 2.17 and 8.9, our final expression for the absorbance can now be written as

$$A(\omega) = A_0 \frac{\gamma \omega^2}{(\omega^2 - \omega_0^2)^2 + 4\gamma^2 \omega^2} \quad (8.11)$$

with a proportionality factor A_0 related to the detailed material properties.

To simplify the solution of the second differential equation (8.6), we restrict ourselves to continuous waves for the external electric field, which can be described by $E(t) = E_1 e^{i\omega_1 t}$. This can be written in frequency domain as $\bar{E}(\omega) = 2\pi E_1 \delta(\omega - \omega_1)$ and we can rewrite eq. 8.7 for this case:

$$x^{(0)}(\omega) = -\frac{2\pi e}{m_e} g(\omega) E_1(\omega) \delta(\omega - \omega_1). \quad (8.12)$$

Fourier transformation back to time domain gives

$$x^{(0)}(t) = -\frac{2\pi e}{m_e} g(\omega_1) E_1 e^{i\omega_1 t}. \quad (8.13)$$

Obviously, eqs. 8.5 and 8.6 have a very similar structure. Hence, the right hand side of the latter can be interpreted as an external force and the equation can be solved in analogy to the Lorentz oscillator model (cf. section 2.1) by applying a Fourier transform to the whole equation. This yields

$$\begin{aligned} x^{(1)}(\omega) &= -g(\omega) \mathcal{F} \left\{ [x^{(0)}(t)]^3 \right\} \\ &= -g(\omega) \mathcal{F} \left\{ \left(\frac{2\pi e}{m_e} \right)^3 g(\omega_1)^3 E_1^3 e^{i3\omega_1 t} \right\} \\ &= - \left(\frac{2\pi e E_1}{m_e} \right)^3 g(\omega_1)^3 g(\omega) \delta(\omega - 3\omega_1) \end{aligned} \quad (8.14)$$

with \mathcal{F} denoting the Fourier transformation. We note that $x^{(1)}(\omega)$ is proportional to $g(\omega_1)^3$.

Using the fact that the radiated far-field of a plane of oscillating charges, representing our nanoantenna array, is proportional to the velocity of the electrons $\dot{x}(t)$, we can calculate the third harmonic intensity as [159]¹

$$I(\omega) \propto |E(\omega)|^2 \propto \omega^2 |x^{(1)}(\omega)|^2 \propto \omega^2 |g(\omega_1)^3|^2. \quad (8.15)$$

Hence, our final result for the third harmonic intensity is given by

$$I(\omega) = I_0 \frac{\omega^2}{\left((\omega^2 - \omega_0^2)^2 + 4\gamma^2 \omega^2 \right)^3} \quad (8.16)$$

where I_0 contains all proportionality factors, including the material dependent parameter a , and is used for scaling purposes when dealing with experimental data.

Equations 8.11 and 8.16 now allow us to investigate the sensor signals defined in eq. 8.1 by means of our model.

8.2 MODELING THE NONLINEAR RESPONSE

The equations for the linear absorbance A and the generated third harmonic intensity I that were derived in section 8.1 are

¹ Making use of the fact that the first derivative in time domain yields a factor $i\omega$ in frequency domain.

now used to gain a deeper understanding of our sensor concept. Although in experiments transmittance T is easier accessible for measurements, we start our discussion based on absorbance A as the originally modeled quantity, and discuss the effects of switching to transmittance in the second part of this section. Therefore, we write the sensor signals in analogy to eq. 8.1:

$$s_L = \frac{\Delta A}{A_1} = \frac{A_2}{A_1} - 1 \quad \text{and} \quad s_{NL} = \frac{\Delta I}{I_1} = \frac{I_2}{I_1} - 1. \quad (8.17)$$

Fig. 8.2a shows A and I around a resonance frequency ω_0 . The primary fact to note here is the distinctly lower line width for the third harmonic intensity spectrum. For the investigation of the sensing behaviour, we do a linear approximation for the intensity changes ΔA and ΔI

$$\Delta A = \frac{\partial A}{\partial \omega_0} \Delta \omega_0 \quad \text{and} \quad \Delta I = \frac{\partial I}{\partial \omega_0} \Delta \omega_0 \quad (8.18)$$

which is valid for small shifts $\Delta \omega_0$ and allows for analytical evaluation of the sensor signals. Additionally, we evaluate the signals numerically by evaluating $A(\omega)$ and $I(\omega)$ explicitly for ω_0 and $\omega_0 + \Delta \omega_0$ and calculating the relative intensity changes through $A_2/A_1 - 1$ and $I_2/I_1 - 1$, respectively. The results for $\Delta \omega_0/\omega_0 = 3\%$ are plotted in Fig. 8.2b and confirm that the analytical and numerical solutions agree very well. Furthermore, the nonlinear signal clearly outperforms the linear signal.

We now calculate an enhancement factor by just dividing the nonlinear signal by the linear signal (Fig. 8.2c) and taking the absolute value. The analytically calculated enhancement factor is

$$\frac{s_{NL}}{s_L} = \frac{\Delta I/I}{\Delta A/A} = 3, \quad (8.19)$$

which one might intuitively expect from a third order nonlinear process. Despite the as of yet good agreement, the numerical result reveals a clear deviation. This deviation originates from the fact that the third harmonic signal does not only shift for a change in ω_0 but also changes its maximum value. While

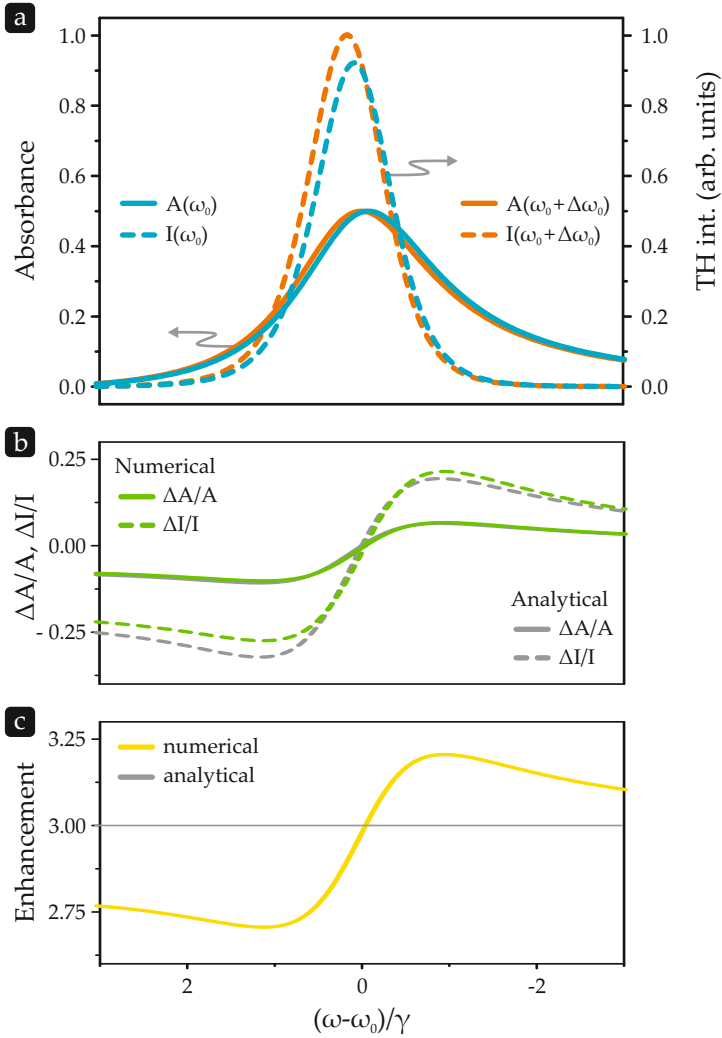


FIGURE 8.2: (a) Modeled absorbance (A) and third harmonic (I) spectra. (b) Numerically and analytically calculated ratios of the corresponding spectra. (c) The analytically (with linear approximation) calculated enhancement for the nonlinear signal yields a factor of three, which one might intuitively expect for a third order nonlinear process. Exact evaluation reveals an additional contribution.

the amplitude at the central wavelength, given as $A(\omega_0) \propto 1/\gamma$ for the linear case, is independent of ω_0 , the TH signal at ω_0 scales as $I(\omega_0) \propto 1/(\gamma^6 \omega_0^4)$, showing a strong dependence on ω_0 . Therefore, the nonlinear signal does, in contrast to the linear signal, exhibit a slightly different line shape. Consequently, this leads to an additional enhancement factor.

Like mentioned at the beginning of this section, in experiments often transmittance T is the measured quantity. Generally, absorbance A , transmittance T , and reflectance R are related through $T + R + A = 1$. Because in our model absolute amplitudes do only act as a scaling factor, and assuming that scattering and absorbance exhibit the same resonant behaviour, we can approximate A as $1 - T$. In some situations it is, however, still necessary to use $\Delta T/T$ as the signal. This has an influence on our model as

$$\frac{\Delta A}{A_1} = \frac{A_2 - A_1}{A_1} = \frac{-\Delta T}{1 - T_1} \neq \frac{\Delta T}{T_1}. \quad (8.20)$$

We therefore take a closer look at the effects on the enhancement factor for this situation. The corresponding spectra are shown in Fig. 8.3a. In analogy to the previous analysis, relative intensity changes are evaluated analytically as well as numerically (Fig. 8.3b). The resulting curves exhibit a flipped sign according to eq. 8.20 for linear signal. Additionally, the linear signal drops off much faster on both sides of the resonance compared to the nonlinear signal. This behaviour originates in the fact that T approaches one far-off the resonance, while A approaches zero instead. This leads to a diverging enhancement factor on both sides of the resonance (Fig. 8.3c), which is generally still not scientifically impossible as noise will also increase with vanishing signals in this spectral region. Anyway, this frequency dependent treatment of the enhancement factor is of minor significance, as one will just compare the maximum achievable signals of both methods independently.

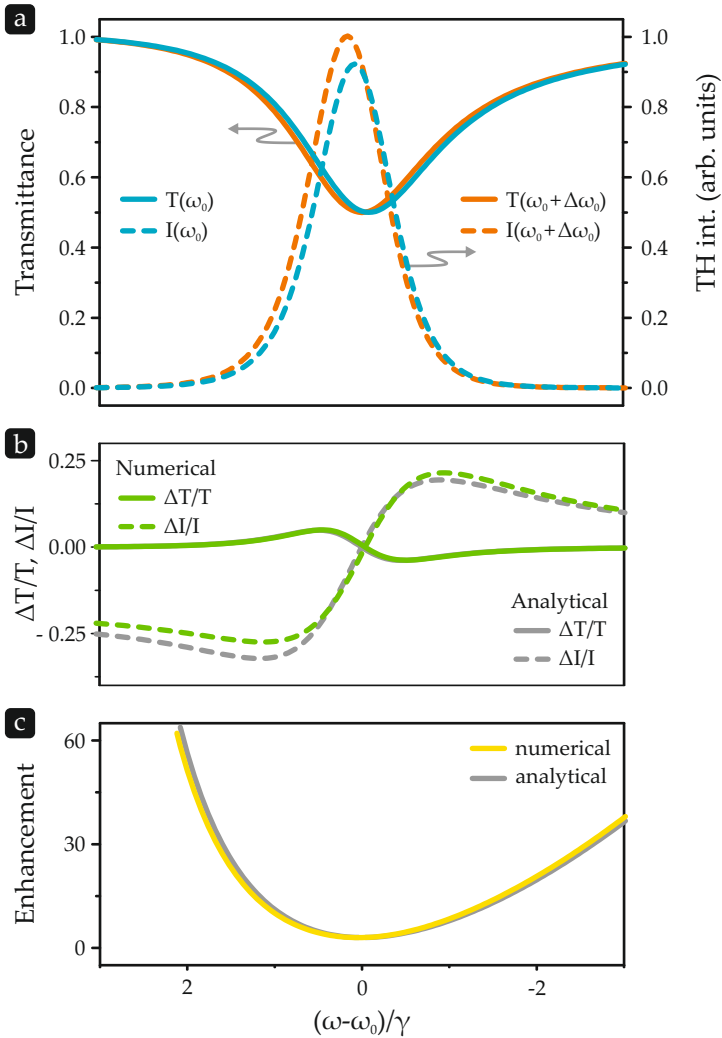


FIGURE 8.3: (a) Modeled transmittance (T) and third harmonic (I) spectra. (b) Numerically and analytically calculated ratios of the corresponding spectra. (c) The enhancement factor in this case diverges at both sides of the resonance, which is of minor significance as noise increases in the same region due to vanishing signals.

8.3 NONLINEAR SPECTROSCOPY

After a detailed discussion of the sensor properties on the basis of the anharmonic oscillator model in the previous section, we will study the linear and nonlinear response of our system experimentally. For characterization of our system and investigation of its spectral behavior, we first do nonlinear spectroscopy.

In our TH spectroscopy setup, laser pulses are focused on $100\ \mu\text{m} \times 100\ \mu\text{m}$ arrays of dipole nanoantennas, polarized parallel to the long antenna axis. Gold nanoantennas are fabricated by standard EBL with parameters estimated by S-matrix simulations in advance (see section 3.1). A sapphire substrate is used to ensure good thermal conductivity and suppress signal drifts through heating effects when conducting experiments with high pulse powers and several hours duration [160]. The sample is mounted in a microfluidic cell with a $70\ \mu\text{m}$ thick liquid channel (see chapter 4). Aqueous analyte solutions can be guided to the nanoantennas by simply connecting the inlet tubing to a reservoir about 20 cm above the cell and placing the outlet to a drain below the cell level. Behind the sample, a grating spectrometer with a Peltier-cooled 2D CCD chip is used to detect the generated third harmonic light. Fundamental and second harmonic light is removed by Schott KG5 and UG11 filters. For linear transmission measurements, a white light source can be coupled into the beam path. Details of the setup are illustrated in Fig. 8.4

To perform TH spectroscopy, we shape 30 fs laser pulses with a Gaussian wavelength distribution and peak wavelengths between 910 nm and 1120 nm in 15 nm steps with an average power of 15 mW with the laser system introduced in section 3.3. For every step we successively record TH intensities for pure water and 8.5 mol/l aqueous ethanol solution. The two analyte solutions have a refractive index difference of $\Delta n \approx 1.5 \times 10^{-2}$. Deionised and filtered water, devoid of biological impurities, was used throughout the experiment. Integration time of the TH signals varies between 10 s and 30 s, depending on signal strength. The different integration times and background effects are accounted for by appropriate normalization. Finally,

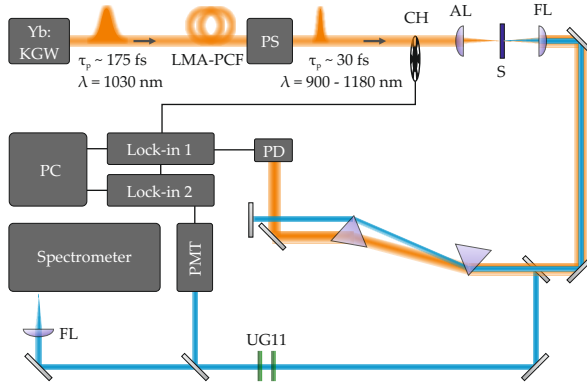


FIGURE 8.4: Illustration of the setup used for third harmonic spectroscopy and nonlinear sensing. Pulses with a Gaussian wavelength distribution and peak wavelengths between 910 nm and 1120 nm can be shaped by the laser system described in section 3.3. Fundamental and third harmonic light can be spatially split by a prism sequence and alternatively be detected by a grating spectrometer or a photo multiplier tube and a silicon diode, respectively.

the TH signal is normalized to the signal generated by the bare substrate (as measured through the cell) and spectrally integrated to deliver a scalar value for the intensity.

In order to map the entire resonant behavior, which exceeds the available tuning range of our laser, we investigated three nanoantenna arrays with varying parameters. All antennas are fabricated with a nominal width of $w = 60$ nm and height of $h = 40$ nm, but differ in length. Scanning electron microscope (SEM) images in Figure Fig. 8.6 (right column) depict the respective antennas with lengths of $l = 150$ nm, 165 nm, and 180 nm.

Linear and third harmonic spectra with increasing resonance wavelength are shown in Fig. 8.5a-c for pure water (blue) and 8.5 mol/l ethanol solution (orange) surrounding the nanoantennas, and are evaluated by fitting eq. 8.11 and eq. 8.16 to the respective measurement data. The linear resonances exhibit spectral shifts between 5.6 nm and 7.1 nm. The impression of a broadened TH spectrum for the nanoantennas covered with ethanol solution (cf. Fig. 8.5b) is not confirmed by

the fit and has its origin in the combination of spectral shift and intensity change. Furthermore, the data point at 910 nm in Fig. 8.5c and Fig. 8.6c had to be omitted as the laser system did not allow for pulses with shape and power comparable to the previous measurements at this edge of the tuning range. Despite the lower absolute TH intensity for the shortest antennas, all their respective ratios exhibit the expected dispersive shape centered on the resonance, and clearly indicate a much higher relative signal change for the nonlinear signal (Fig. 8.6a-c). All trends agree nicely with the modeled behavior displayed in section 8.2. Variations in absolute signal levels and deviations from the modeled behavior are well within the expected uncertainties in nonlinear spectroscopy measurements and can be attributed to tolerances in fabrication of the nanoantennas and measurements. Additionally, in a first approximation, the TH sensitivity does not depend on the excitation power. Even though the incident intensity certainly has a strong influence on the absolute TH intensity, the sensor signal, as a differential signal, is not affected. In order to further investigate the behavior, we choose the spectral position denoted by the vertical dashed line in Fig. 8.6a to directly compare linear and nonlinear sensing in the following. This wavelength is close to the maximum sensitivity for both methods and the selected antenna array exhibits the maximum nonlinear sensitivity $\Delta I/I$ of the presented structures.

8.4 NONLINEAR SENSING

Using linear and third harmonic spectroscopy, we characterized the linear and nonlinear response of our gold nanoantenna arrays. In the following we compare the two sensing concepts in a scheme closer related to applications, monitoring concentration variations in analyte solutions by measuring transmittance changes in a narrow spectral region.

For a sound comparison, it is most favorable to detect linear and nonlinear signals simultaneously. Therefore, we modify our setup and replace the spectrometer by two separate detectors. Light at the fundamental and third harmonic wavelengths

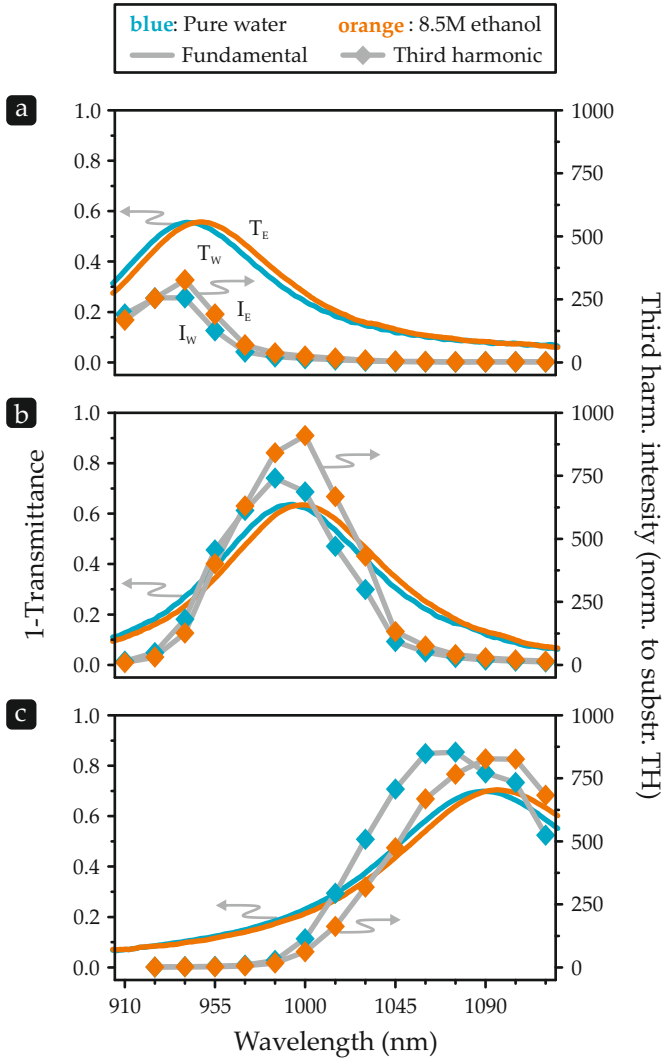


FIGURE 8.5: (a-c) Measured $1 - T$ (solid lines) and third harmonic (connected dots) spectra for water (index W) and 8,5 mmol/l aqueous ethanol solution (index E), corresponding to $\Delta n \approx 1.5 \cdot 10^{-2}$. Three plasmonic nanoantenna arrays with different antenna length, depicted in Fig. 8.6 were investigated.

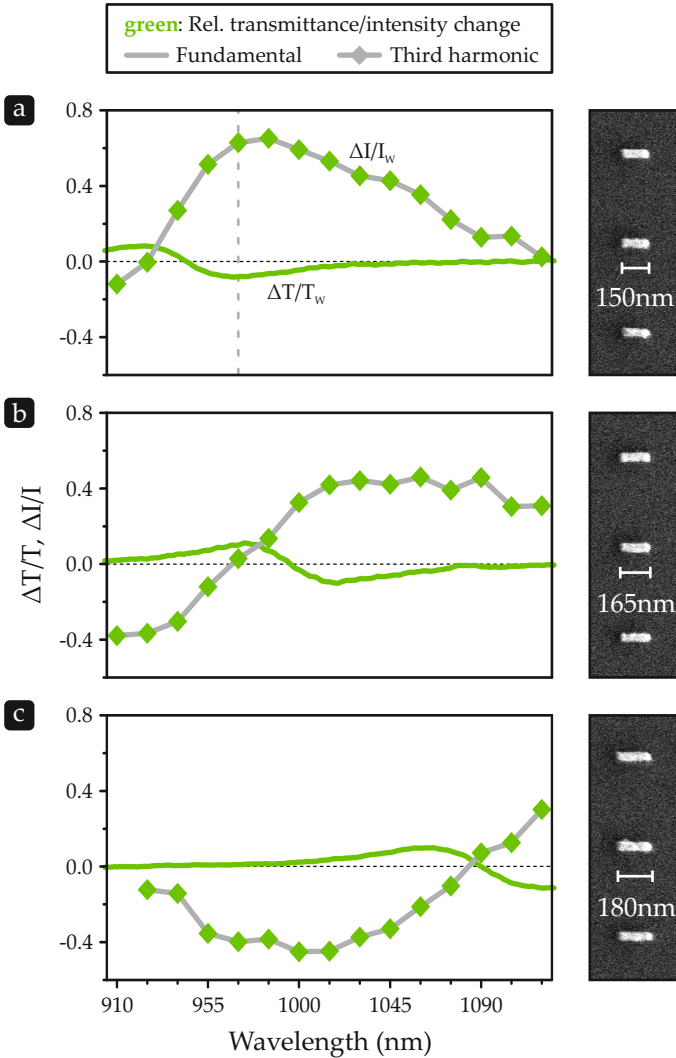


FIGURE 8.6: (a-c) The ratios of the linear and nonlinear spectra, respectively, exhibit the expected dispersive shape with an extremum on both sides of the resonance, clearly indicate a much higher relative intensity change for the nonlinear signal, and are in good agreement with the model.

is split spatially by a prism sequence and routed into a silicon photodiode and a photomultiplier tube (PMT), respectively. The two detector signals are fed into identical lock-in amplifiers to ensure equal signal treatment. The associated light chopper is inserted in front of the focusing optics of the beam incident to the sample. Again, Schott UG11 filters are used to protect the PMT from stray light.

The measurement is carried out on the 150 nm antenna array at 970 nm incident wavelength (as denoted in Fig. 8.6a), with an average on sample power of 5 mW, focused onto a diameter of 50 μm . Six aqueous ethanol analyte solutions are prepared by a dilution series, with concentrations corresponding to $\Delta n \approx (150, 60, 30, 15, 6, 3) \times 10^{-4}$ with respect to the refractive index of pure water. Decreasing concentrations of analyte solutions are, alternately with pure water, filled into the sensor cell in a continuous measurement. Data points are recorded every 200 ms and are subsequently averaged by a percentile filter with a span of 60 s.

The resulting time traces are plotted in Fig. 8.7a. The nonlinear signal shows a maximum increase as high as 70% for concentrated ethanol solution, whereas the linear signal decreases by approximately 10% for the same concentration. Those results are consistent with the values from the previous spectroscopy measurements (at the spectral position indicated by the vertical dashed line in Fig. 8.6a. Although high signals are desirable for a sensor, equally important values are signal-to-noise ratio (SNR) and, closely related, the limit of detection. In order to compare those quantities for both methods, we invert the linear signal and normalize both signals to an interval from 0 to 1 (Fig. 8.7b). In this representation it becomes apparent that the signal-to-noise ratio is almost equal for both methods, leading to an estimated detection limit of $\Delta n \approx 1 \times 10^{-3}$.

8.5 CONCLUSIONS

In summary, we introduced in this chapter nonlinear plasmonic sensing to enhance the sensitivity of localized surface plasmon resonance sensors. The strong dependence on the local elec-

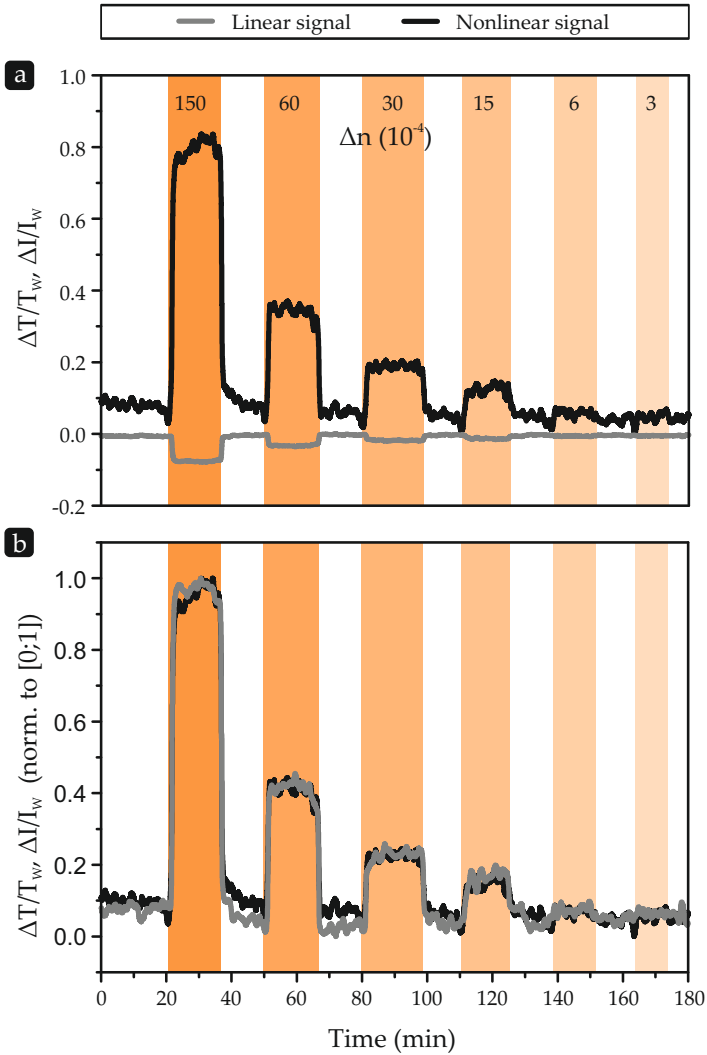


FIGURE 8.7: Simultaneously recorded time traces of linear and nonlinear signals for decreasing concentrations of ethanol in water (W). (a) The nonlinear signal increases by about 70% for concentrated ethanol solution, whereas the linear signal decreases by approximately 10%. (b) Normalized to an interval of 0 to 1, it becomes apparent that the signal to noise ratio is almost equal.

tric fields of the nanoantennas in the process of third harmonic generation gives rise to a distinct increase of the sensor signal. The spectral behavior of the nonlinear signal obtained by third harmonic spectroscopy could also be described by an anharmonic oscillator model. In direct comparison it turns out that both methods reproduce the refractive index changes equally well and no distortion occurs due to the nonlinear process.

Anyhow, special attention has to be paid to the almost equal signal-to-noise ratio of the two concepts. Both methods simultaneously probe the same (linear) process, namely the resonance shift upon a change in the dielectric environment of the antenna. Therefore, we suspect that the main source of noise in our system is the laser system. Consequently, enhancement factors, like discussed in section 8.2, generally have to be treated with caution and are of minor significance without a detailed investigation of the underlying process and the respective sources of noise. Nevertheless, the fact that the nonlinear signal is comparable to the linear one, despite its many orders of magnitude lower absolute amplitude, leads to the conclusion that experimental techniques allow to use linear and nonlinear processes equally in such applications.

Future investigations could include nonlinear sensors that do not just rely on a shift of the resonance frequency, but on a change of the damping parameter γ , such as for example in palladium-based plasmonic hydrogen sensors [161, 162]. The benefit of this method lies in the fact that damping contributes drastically to the generated third harmonic intensity. Therefore, even higher enhancement might be achievable. Other sensing schemes that rely on alternative nonlinear wave mixing processes are also available, such as second harmonic generation (SHG) [163–165], sum frequency generation (SFG), difference frequency generation (DFG), or four wave mixing (FWM). Particularly interesting could be the combination of anisotropic liquids with resonant nanoantennas, which break inversion symmetry and enhance especially $\chi^{(2)}$ processes. This will also become relevant when going from bulk refractive index sensing toward surface-functionalized sensing, where individual small molecules or thin molecular layers, directly on the sur-

face in the region of highest field enhancement, generate the nonlinear optical effects. Especially when considering second harmonic generation, the symmetry of the molecules and their specific orientation might result in additional nonlinear optical signals [166].



SUMMARY & OUTLOOK

This thesis dealt with different aspects of localized surface plasmon resonance (LSPR) sensing. It covered the topics of optimizing the plasmonic structure itself, the often necessary functionalization for the recognition of a specific analyte, and the detection scheme for the changes of the plasmonic resonance.

We analyzed the sensing performance of a complex coupled plasmonic structure by means of perturbation theory and numerical simulations. This structure consists of a dipole antenna in the bottom layer and two parallel antennas in the top layer, which are perpendicular to the first one and support a quadrupolar mode. The coupling strength can be adjusted by the displacement of dipole antenna from its symmetric position. Because of the coupling of the two initial modes, the optical spectrum of the structure exhibits two hybrid modes. We have seen that the shift of the resonant modes under a local refractive index change is directly related to the energy storage in the analyte volume, that is, the energy stored in the plasmonic mode. Different sensing scenarios, such as refractive index changes in the bulk volume or in a thin layer around the structures were investigated. Both can either be detected via a shift of the resonance or a intensity difference at the slope of the resonance. We observed that resonance shifts are maximal for low coupling strength at the high energy mode. In contrast, intensity differences for a given refractive index change are best monitored using the distinct spectral features and steep slopes provided in the strong coupling regime. The behavior in the case of changes limited to the structure surface follows the trend for refractive index variations in the bulk surroundings. In general, the transition from the uncoupled to the coupled structure leads to an enhancement of the sensor performance, indicating its superiority in comparison to simple dipole antennas.

As it is impossible to distinguish between the different origins of a refractive index change with just a bare plasmonic structure, functionalization is of crucial importance. Ideally, it limits the response of the sensor to a single desired analyte and at the same time enhances the signal. By coating arrays of gold nanoantennas with a thin layer of a hydrogel, which is functionalized to respond to glucose with a reversible swelling, we demonstrated such a clear signal enhancement in comparison to the changes induced by the glucose molecules alone. This allowed to detect concentrations in the physiological range. Another important aspect, especially in the realm of biological sensing, is the influence of proteins. These bulky and sticky molecules easily affect a sensitive detector. We have shown that the hydrogel layer successfully prevents them to enter the sensitive area around the plasmonic structures and ensures clear readings for varying glucose concentrations. What is more, the biocompatibility of the hydrogel as well as the gold structures enables applications in biomedical devices.

Owing to slow diffusion processes in the unswollen polymer, the response time of the hydrogel covered sensor increases for low glucose concentrations. The strongly confined fields around the nanostructures permit to counteract this issue by further decreasing the thickness of the hydrogel layer. Therefore, we adapted a layer-by-layer fabrication approach to obtain an ultrathin hydrogel film. Here, the polymer film is grown by alternately depositing monomolecular layers of differently functionalized polymers. However, even though we could successfully grow the multilayered structure, the system did not respond to glucose solutions as expected. Further chemical modifications are expected to resolve this issue. Therefore, the technique still is an interesting alternative for hydrogel coated sensors.

Obviously, chemical functionalization is a challenging step in the sensor design. Hence, identifying substances via their unique molecular fingerprints in the infrared spectral region is a tempting alternative, which we pursued by studying the same analyte with surface enhanced infrared absorption (SEIRA). In contrast to the previous results, in SEIRA we can only make

use of the enhanced plasmonic near-fields, while no additional enhancement scheme comparable to the hydrogel is available. Thus, we expect to not be able to detect concentrations as low as in the case of hydrogel assisted refractive index sensing. An estimation of the signal strength reveals that also in this system functionalization is required in order to accumulate the analyte molecules of dilute aqueous solutions in the areas of high field enhancement and thus boost the response. This approach, however, is in conflict with the inherent advantage of identifying analytes by their molecular vibration spectra.

Finally, we introduced the novel concept of nonlinear plasmonic sensing to enhance the sensitivity of LSPR sensors by a nonlinear detection scheme. The strong dependence on the local electric fields of the nanoantennas in the process of third harmonic generation gives rise to a distinct increase of the sensor signal. Our nonlinear spectroscopic results are well described by an anharmonic oscillator model. Direct comparison of linear and nonlinear sensing in continuous measurements yet lead to an equal signal-to-noise ratio. Real enhancement is therefore restricted to systems where the analyte has a fundamental influence on the nonlinear process, that is, in which the analyte enables an additional contribution to the nonlinear signal.

From the aforementioned results we can draw a number of general conclusions: First of all, we have to note the eminent enhancement of the sensor response by the hydrogel functionalization. It clearly outperforms the gain acquired through the use of a complex coupled structure. Considering the additional benefit of its specificity and filtering capabilities, it will be the system of choice in many applications for aqueous analyte solutions. Particularly the fact that hydrogels can be functionalized to respond to a multitude of analytes and are yet not even optimized for the specific task in plasmonic sensing underlines the large potential of the technique. The use of high refractive index polymers in the hydrogels could for instance lead to an enhanced refractive index difference upon hydrogel swelling.

Moreover, it is noteworthy that all results keep their validity when moving from arrays of nanostructures to single particles.

In contrast to other techniques such as quartz crystal microbalances or surface plasmon resonance spectroscopy, one of the main advantages of LSPR sensors, namely the ultras-small sensing volume, can be fully exploited in this case.

The different measurements also reveal that tracking a resonance shift of a spectral feature is in almost all situations preferable, compared to intensity differences at the slope of the resonance. Using the entire spectral information with the centroid evaluation method, allows to monitor minute shifts even in the case of broad resonances. Furthermore, the resonance position is directly related to the physical properties of interest, while the recorded intensity differences, in contrast, suffer from fluctuations of the utilized light source, which can often not be neglected.

Apparently, coupled plasmonic structures are extremely sensitive to minute changes in the relative position and distance of the constituent particles. Using the reversible swelling of hydrogels in the presence of the desired analyte consequently allows to manipulate the optical properties of plasmonic nanoparticle groupings and is thus a highly interesting route for further optimization of the sensor structures presented in this thesis.



BIBLIOGRAPHY

- [1] M. Faraday. The Bakerian Lecture: Experimental Relations of Gold (and other Metals) to Light. *Phil. Trans. R. Soc. London A*, 147:145–181, 1857.
- [2] R. W. Wood. On a remarkable case of uneven distribution of light in a diffraction grating spectrum. *Proc. Phys. Soc. London*, 18(1):269, 1902.
- [3] L. Rayleigh. On the Dynamical Theory of Gratings. *P. R. Soc. London A*, 79:399–416, 1907.
- [4] M. J. C. Garnett. Colours in Metal Glasses and in Metallic Films. *Phil. Trans. R. Soc. London A*, 203:385–420, 1904.
- [5] G. Mie. Beiträge zur Optik trüber Medien, speziell kolloidaler Metallösungen. *Ann. Phys.*, 330:377–445, 1908.
- [6] R. Gans. Über die Form ultramikroskopischer Goldteilchen. *Ann. Phys.*, 342:881–900, 1912.
- [7] F. Kirchner and R. Zsigmondy. Über die Ursachen der Farbänderungen von Gold-Gelatinepräparaten. *Ann. Phys.*, 320(13):573–595, 1904.
- [8] V. G. Veselago. The electrodynamics of substances with simultaneously negative values of ϵ and μ . *Soviet Phys. Uspekhi*, 10(4):509–514, 1968.
- [9] R. A. Shelby, D. R. Smith, and S. Schultz. Experimental Verification of a Negative Index of Refraction. *Science*, 292:77–79, 2001.
- [10] G. Dolling, M. Wegener, C. M. Soukoulis, and S. Linden. Negative-index metamaterial at 780 nm wavelength. *Opt. Lett.*, 32(1):53–55, 2007.

- [11] D. R. Smith, J. B. Pendry, and M. C. K. Wiltshire. Metamaterials and Negative Refractive Index. *Science*, 305:788–792, 2004.
- [12] J. B. Pendry. Negative Refraction Makes a Perfect Lens. *Phys. Rev. Lett.*, 85(18):3966–3969, 2000.
- [13] C. M. Soukoulis, S. Linden, and M. Wegener. Negative Refractive Index at Optical Wavelengths. *Science*, 315:47–49, 2007.
- [14] D. Schurig, J. J. Mock, B. J. Justice, S. A. Cummer, J. B. Pendry, A. F. Starr, and D. R. Smith. Metamaterial Electromagnetic Cloak at Microwave Frequencies. *Science*, 314(5801):977–980, 2006.
- [15] T. Ergin, N. Stenger, P. Brenner, J. B. Pendry, and M. Wegener. Three-Dimensional Invisibility Cloak at Optical Wavelengths. *Science*, 328(5976):337–339, 2010.
- [16] D. Dregely, K. Lindfors, J. Dorfmüller, M. Hentschel, M. Becker, J. Wrachtrup, M. Lippitz, R. Vogelgesang, and H. Giessen. Plasmonic antennas, positioning, and coupling of individual quantum systems. *Phys. Stat. Sol. B*, 249(4):666–677, 2012.
- [17] T. H. Taminiau, F. D. Stefani, F. B. Segerink, and N. F. van Hulst. Optical antennas direct single-molecule emission. *Nature Photonics*, 2:234–237, 2008.
- [18] A. G. Curto, G. Volpe, T. H. Taminiau, M. P. Kreuzer, R. Quidant, and N. F. van Hulst. Unidirectional Emission of a Quantum Dot Coupled to a Nanoantenna. *Science*, 329:930–933, 2010.
- [19] M. Quinten, A. Leitner, J. R. Krenn, and F. R. Aussenegg. Electromagnetic energy transport via linear chains of silver nanoparticles. *Opt. Lett.*, 23(17):1331–1333, 1998.
- [20] D. Dregely, K. Lindfors, M. Lippitz, N. Engheta, M. Totzeck, and H. Giessen. Imaging and steering an optical wireless nanoantenna link. *Nature Communications*, 5(4354), 2014.

- [21] T. Kosako, Y. Kadoya, and H. F. Hofmann. Directional control of light by a nano-optical Yagi-Uda antenna. *Nature Photonics*, 4:312–315, 2010.
- [22] A. Alu and N. Engheta. Wireless at the Nanoscale: Optical Interconnects using Matched Nanoantennas. *Phys. Rev. Lett.*, 104(213902), 2010.
- [23] M. Hentschel, T. Utikal, H. Giessen, and M. Lippitz. Quantitative Modeling of the Third Harmonic Emission Spectrum of Plasmonic Nanoantennas. *Nano Lett.*, 12:3778–3782, 2012.
- [24] M. Schäferling, D. Dregely, M. Hentschel, and H. Giessen. Tailoring Enhanced Optical Chirality: Design Principles for Chiral Plasmonic Nanostructures. *Phys. Rev. X*, 2(031010):1–9, 2012.
- [25] M. Hentschel, M. Schäferling, B. Metzger, and H. Giessen. Plasmonic Diastereomers: Plasmonic Diastereomers: Adding up Chiral Centers. *Nano Lett.*, 13:600–606, 2013.
- [26] S. Kim, J. Jin, Y.-J. Kim, I.-Y. Park, Y. Kim, and S.-W. Kim. High-harmonic generation by resonant plasmon field enhancement. *Nature*, 453:757–760, 2008.
- [27] Y. Zhang, F. Wen, Y.-R. Zhen, P. Nordlander, and N. J. Halas. Coherent Fano resonances in a plasmonic nanocluster enhance optical four-wave mixing. *Proc. Natl. Acad. Sci.*, 110(23):9215–9219, 2013.
- [28] M. W. Klein, C. Enkrich, M. Wegener, and S. Linden. conditions, the simulated traces are virtually free of adjustable parameters as C Q 4 C. *Science*, 313:502–504, 2006.
- [29] B. Metzger, M. Hentschel, T. Schumacher, M. Lippitz, X. Ye, C. B. Murray, B. Knabe, K. Buse, and H. Giessen. Doubling the Efficiency of Third Harmonic Generation by Positioning ITO Nanocrystals into the Hot-Spot of Plasmonic Gap-Antennas. *Nano Lett.*, 14:2867–2872, 2014.

- [30] B. Metzger, L. Gui, J. Fuchs, D. Floess, M. Hentschel, and H. Giessen. Strong Enhancement of Second Harmonic Emission by Plasmonic Resonances at the Second Harmonic Wavelength. *Nano Lett.*, 15:3917–3922, 2015.
- [31] Z. Lu, X. Pan, Y. Ma, Y. Li, L. Zheng, D. Zhang, Q. Xu, Z. Chen, S. Wang, B. Qu, F. Liu, Y. Huang, L. Xiao, and Q. Gong. Plasmonic-enhanced perovskite solar cells using alloy popcorn nanoparticles. *RSC Adv.*, 5:11175–11179, 2015.
- [32] E. S. Arinze, B. Qiu, G. Nyirjesy, and S. M. Thon. Plasmonic Nanoparticle Enhancement of Solution-Processed Solar Cells: Practical Limits and Opportunities. *ACS Photonics*, 3:158–173, 2016.
- [33] R. B. Dunbar, T. Pfadler, and L. Schmidt-Mende. Highly absorbing solar cells - a survey of plasmonic nanostructures. *Optics Express*, 20:A177–A189, 2012.
- [34] H. A. Atwater and A. Polman. Plasmonics for improved photovoltaic devices. *Nature Materials*, 9:205–213, 2010.
- [35] F. Neubrech, A. Pucci, T. Cornelius, S. Karim, A. García-Etxarri, and J. Aizpurua. Resonant Plasmonic and Vibrational Coupling in a Tailored Nanoantenna for Infrared Detection. *Phys. Rev. Lett.*, 101(15):157403, 2008.
- [36] K. Kneipp, Y. Wang, H. Kneipp, L. T. Perelman, I. Itzkan, R. R. Dasari, and M. S. Feld. Single Molecule Detection Using Surface-Enhanced Raman Scattering (SERS). *Phys. rev. Lett.*, 78(9):1667–1670, 1997.
- [37] I. Ament, J. Prasad, A. Henkel, S. Schmachtel, and C. Sönnichsen. Single Unlabeled Protein Detection on Individual Plasmonic Nanoparticles. *Nano Lett.*, 12:1092–1095, 2012.
- [38] P. Zijlstra, P. M. R. Paulo, and M. Orrit. Optical detection of single non-absorbing molecules using the surface plasmon resonance of a gold nanorod. *Nature Nanotechnology*, 7:379–382, 2012.

- [39] J. D. Jackson. *Classical Electrodynamics*. John Wiley & Sons, New York, third edition, 1999.
- [40] S. A. Maier. *Plasmonics: Fundamentals and Applications*. Springer, New York, 2007.
- [41] Demtröder, W. *Experimentalphysik 2: Elektrizität und Optik*. Springer, Berlin Heidelberg New York, fourth edition, 2006.
- [42] P. B. Johnson and R. W. Christy. Optical constants of the noble metals. *Phys. Rev. B*, 6:4370–4379, 1972.
- [43] R. W. Boyd. *Nonlinear Optics*. Elsevier, New York, third edition, 2008.
- [44] R. H. Stolen and C. Lin. Self-phase-modulation in silica optical fibers. *Phys. Rev. A*, 17(4):1448–1454, 1978.
- [45] CST Microwave Studio Documentation, 2015.
- [46] D. M. Whittaker and I. S. Culshaw. Scattering-matrix treatment of patterned multilayer photonic structures. *Phys. Rev. B*, 60(4):2610–2618, 1999.
- [47] S. G. Tikhodeev, A. L. Yablonskii, E. A. Muljarov, N. A. Gippius, and T. Ishihara. Quasiguidded modes and optical properties of photonic crystal slabs. *Phys. Rev. B*, 66:045102, 2002.
- [48] T. Weiss, G. Granet, N. A. Gippius, S. G. Tikhodeev, and H. Giessen. Matched coordinates and adaptive spatial resolution in the Fourier modal method. *Optics Express*, 17(10):8051–8061, 2009.
- [49] S. Essig and K. Busch. Generation of adaptive coordinates and their use in the Fourier Modal Method. *Optics Express*, 18(22):23258–23274, 2010.
- [50] Mack, C. *Fundamental Principles of Optical Lithography*. John Wiley & Sons, Chichester, first edition, 2007.
- [51] I. F. Burgess. The mode of action of dimeticone 4% lotion against head lice, *Pediculus capitis*. *BMC Pharmacology*, 9(3), 2009.

- [52] J. C. McDonald, D. C. Duffy, J. R. Anderson, D. T. Chiu, H. Wu, O. J. A. Schueller, and G. M. Whitesides. Fabrication of microfluidic systems in poly(dimethylsiloxane). *Electrophoresis*, 21:27–40, 2000.
- [53] R. Höfer, F. Jost, M. J. Schwuger, R. Scharf, J. Geke, J. Kresse, H. Lingmann, R. Veitenhansl, and W. Erwied. Foams and Foam Control. In *Ullmann's Encyclopedia of Industrial Chemistry*, pages 572–598. Wiley-VCH Verlag GmbH & Co. KGaA, 2000.
- [54] J. N. Lee, C. Park, and G. M. Whitesides. Solvent Compatibility of Poly(dimethylsiloxane)-Based Microfluidic Devices. *Anal. Chem.*, 75(23):6544–6554, 2003.
- [55] B. D. Gates. Nanofabrication with molds & stamps. *Materials Today*, 8:44–49, 2005.
- [56] J. A. Rogers and R. G. Nuzzo. Recent progress in soft lithography. *Materials Today*, 8(2):50–56, 2005.
- [57] Demtröder, W. *Experimentalphysik 3: Atome, Moleküle und Festkörper*. Springer, Berlin Heidelberg New York, third edition, 2005.
- [58] A. B. Dahlin, J. O. Tegenfeldt, and F. Höök. Improving the Instrumental Resolution of Sensors Based on Localized Surface Plasmon Resonance. *Anal. Chem.*, 78(13):4416–4423, 2006.
- [59] B. Metzger, A. Steinmann, and H. Giessen. High-power widely tunable sub-20 fs Gaussian laser pulses for ultrafast nonlinear spectroscopy. *Opt. Express*, 19:24354–24360, 2011.
- [60] B. Metzger, A. Steinmann, F. Hoos, S. Pricking, and H. Giessen. Compact laser source for high-power white-light and widely tunable sub 65 fs laser pulses. *Opt. Lett.*, 35(23):3961–3963, 2010.
- [61] G. P. Agrawal. *Nonlinear fiber optics*. Elsevier, Academic Press, Amsterdam; Heidelberg [u.a.], fifth edition, 2013.

- [62] A. M. Heidt, A. Hartung, G. W. Bosman, P. Krok, E. G. Rohwer, H. Schwoerer, and H. Bartelt. Coherent octave spanning near-infrared and visible supercontinuum generation in all-normal dispersion photonic crystal fibers. *Opt. Express*, 19(4):3775–3787, 2011.
- [63] T. A. Birks, W. J. Wadsworth, and P. S. J. Russell. Supercontinuum generation in tapered fibers. *Opt. Lett.*, 25(19):1415–1417, 2000.
- [64] S. Pricking and H. Giessen. Tailoring the soliton and supercontinuum dynamics by engineering the profile of tapered fibers. *Opt. Express*, 18(19):20151–20163, 2010.
- [65] D. C. Duffy, J. C. McDonald, O. J. A. Schueller, and G. M. Whitesides. Rapid Prototyping of Microfluidic Systems in Poly(dimethylsiloxane). *Anal. Chem.*, 70:4974–4984, 1998.
- [66] K. Haubert, T. Drier, and D. Beebe. PDMS bonding by means of a portable, low-cost corona system. *Lab on a chip*, 6(12):1548–9, 2006.
- [67] A. Grimes, D. N. Breslauer, M. Long, J. Pegan, L. P. Lee, and M. Khine. Shrinky-Dink microfluidics: rapid generation of deep and rounded patterns. *Lab on a chip*, 8:170–172, 2008.
- [68] C.-S. Chen, D. N. Breslauer, J. I. Luna, A. Grimes, W.-C. Chin, L. P. Lee, and M. Khine. Shrinky-Dink microfluidics: 3D polystyrene chips. *Lab on a chip*, 8(4):622–4, 2008.
- [69] D. Taylor, D. Dyer, V. Lew, and M. Khine. Shrink film patterning by craft cutter: complete plastic chips with high resolution/high-aspect ratio channel. *Lab on a chip*, 10(18):2472–5, 2010.
- [70] K. A. Willets and R. P. van Duyne. Localized surface plasmon resonance spectroscopy and sensing. *Annual review of physical chemistry*, 58:267–97, 2007.

- [71] J. N. Anker, W. P. Hall, O. Lyandres, N. C. Shah, J. Zhao, and R. P. van Duyne. Biosensing with Plasmonic Nanosensors. *Nat. Mater.*, 7(6):442–453, 2008.
- [72] L. J. Sherry, S.-H. Chang, G. C. Schatz, R. P. van Duyne, B. J. Wiley, and Y. Xia. Localized Surface Plasmon Resonance Spectroscopy of Single Silver Nanocubes. *Nano Lett.*, 5(10):2034–2038, 2005.
- [73] M. M. Miller and A. A. Lazarides. Sensitivity of Metal Nanoparticle Surface Plasmon Resonance to the Dielectric Environment. *J. Phys. Chem. B*, 109(46):21556–21565, 2005.
- [74] B. Otte, M. A. and Sepúlveda, W. Ni, J. Pérez, L. M. Liz-Marzán, and L. M. Lechuga. Identification of the Optimal Spectral Region for Plasmonic and Nanoplasmonic Sensing. *ACS Nano*, 4(1):349–357, 2010.
- [75] G. J. Nusz, A. C. Curry, S. M. Marinakos, A. Wax, and A. Chilkoti. Rational Selection of Gold Nanorod Geometry for Label-Free Plasmonic Biosensors. *ACS Nano*, 3(4):795–806, 2009.
- [76] A. Unger and M. Kreiter. Analyzing the Performance of Plasmonic Resonators for Dielectric Sensing. *J. Phys. Chem. C*, 113:12243–12251, 2009.
- [77] J. Becker, A. Trügler, A. Jakab, U. Hohenester, and C. Sönnichsen. The Optimal Aspect Ratio of Gold Nanorods for Plasmonic Bio-sensing. *Plasmonics*, 5(2):161–167, 2010.
- [78] B. Luk'yanchuk, N. I. Zheludev, S. A. Maier, N. J. Halas, P. Nordlander, H. Giessen, and C. T. Chong. The Fano resonance in plasmonic nanostructures and metamaterials. *Nature materials*, 9(9):707–15, 2010.
- [79] N. Liu, L. Langguth, T. Weiss, J. Kästel, M. Fleischhauer, T. Pfau, and H. Giessen. Plasmonic analogue of electromagnetically induced transparency at the Drude damping limit. *Nature Materials*, 8:758–762, 2009.

- [80] F. Vollmer and L. Yang. Label-free detection with high-Q microcavities: a review of biosensing mechanisms for integrated devices. *Nanophotonics*, 1:267–291, 2012.
- [81] N. L. Bocchio, A. Unger, M. Álvarez, and M. Kreiter. Thin Layer Sensing with Multipolar Plasmonic Resonances. *J. Phys. Chem. C*, 112:14355–14359, 2008.
- [82] H. M. Lai, P. T. Leung, K. Young, P. W. Barber, and S. C. Hill. Time-independent perturbation for leaking electromagnetic modes in open systems with application to resonances in microdroplets. *Phys. Rev. A*, 41:5187–5198, 1990.
- [83] R. Ruppin. Electromagnetic energy density in a dispersive and absorptive material. *Phys. Lett. A*, 299:309–312, 2002.
- [84] S. A. Maier. Plasmonic field enhancement and SERS in the effective mode volume picture. *Opt. Express*, 14(5):1957–64, 2006.
- [85] P. T. Kristensen, C. van Vlack, and S. Hughes. Generalized effective mode volume for leaky optical cavities. *Opt. Lett.*, 37(10):1649–1651, 2012.
- [86] A. F. Koenderink. On the use of Purcell factors for plasmon antennas. *Opt. Lett.*, 35(24):4208–10, 2010.
- [87] B. Gallinet and O. J. F. Martin. Ab initio theory of Fano resonances in plasmonic nanostructures and metamaterials. *Phys. Rev. B*, 83(23):1–6, 2011.
- [88] B. Gallinet and O. J. F. Martin. Relation between near-field and far-field properties of plasmonic Fano resonances. *Opt. Express*, 19(22):1664–1670, 2011.
- [89] B. Gallinet and O. J. F. Martin. Influence of Electromagnetic Interactions on the Line Shape of Plasmonic Fano Resonances. *ACS Nano*, 5(11):8999–9008, 2011.
- [90] T. Weiss, M. Mesch, M. Schäferling, H. Giessen, W. Langbein, and Muljarov E. A. From dark to bright: First-order perturbation theory with analytical mode normalization for

- plasmonic nanoantenna arrays applied to refractive index sensing. *Phys. Rev. Lett.*, 116:237401, 2016.
- [91] E. M. Larsson, S. Syrenova, and C. Langhammer. Nanoplasmonic Sensing for Nanomaterials Science. *Nanophotonics*, 1(3-4):249–266, 2012.
- [92] K. M. Mayer and J. H. Hafner. Localized Surface Plasmon Resonance Sensors. *Chem. Rev.*, 111(6):3828–3857, 2011.
- [93] F. Hao, Y. Sonnefraud, P. van Dorpe, S. A. Maier, N. J. Halas, and P. Nordlander. Symmetry Breaking in Plasmonic Nanocavities: Subradiant LSPR Sensing and a Tunable Fano Resonance. *Nano Lett.*, 8(11):3983–3988, 2008.
- [94] B. Gallinet and O. J. F. Martin. Refractive Index Sensing with Subradiant Modes: A Framework To Reduce Losses in Plasmonic Nanostructures. *ACS Nano*, 7:6978–6987, 2013.
- [95] A. Jakab, C. Rosman, Y. Khalavka, J. Becker, A. Trügler, U. Hohenester, and C. Sönnichsen. Highly Sensitive Plasmonic Silver Nanorods. *ACS Nano*, 5:6880–6885, 2011.
- [96] A. A. Lazarides, K. L. Kelly, T. R. Jensen, and G. C. Schatz. Optical Properties of Metal Nanoparticles and Nanoparticle Aggregates Important in Biosensors. *J. Mol. Struct.: THEOCHEM*, 529:59–63, 2000.
- [97] J. M. McMahon, J. Henzie, T. W. Odom, G. C. Schatz, and S. K. Gray. Tailoring the Sensing Capabilities of Nanohole Arrays in Gold Films with Rayleigh Anomaly–Surface Plasmon Polaritons. *Opt. Express*, 15:18119–18129, 2007.
- [98] A. J. Haes, S. Zou, G. C. Schatz, and R. P. van Duyne. A Nanoscale Optical Biosensor: The Long Range Distance Dependence of the Localized Surface Plasmon Resonance of Noble Metal Nanoparticles. *J. Phys. Chem. B*, 108:109–116, 2004.
- [99] M. König, M. Rahmani, L. Zhang, D. Y. Lei, T. R. Roschuk, V. Giannini, C.-W. Qiu, M. Hong, S. Schlücker, and S. A.

- Maier. Unveiling the Correlation between Nanometer-Thick Molecular Monolayer Sensitivity and Near-Field Enhancement and Localization in Coupled Plasmonic Oligomers. *ACS Nano*, 8:9188–9198, 2014.
- [100] Y. Zhan, D. Y. Lei, X. Li, and S. A. Maier. Plasmonic Fano Resonances in Nanohole Quadrumers for Ultra-sensitive Refractive Index Sensing. *Nanoscale*, 6:4705–4715, 2014.
- [101] C. L. Haynes and R. P. van Duyne. Nanosphere Lithography: A Versatile Nanofabrication Tool for Studies of Size-Dependent Nanoparticle Optics. *J. Phys. Chem. B*, 105(24):5599–5611, 2001.
- [102] L. J. Guo. Nanoimprint Lithography: Methods and Material Requirements. *Adv. Mater.*, 19(4):495–513, 2007.
- [103] S. Aksu, A. A. Yanik, R. Adato, A. Artar, M. Huang, and H. Altug. High-Throughput Nanofabrication of Infrared Plasmonic Nanoantenna Arrays for Vibrational Nanospectroscopy. *Nano Lett.*, 10(7):2511–2518, 2010.
- [104] A. A. Yanik, M. Huang, A. Artar, T.-Y. Chang, and H. Altug. Integrated Nanoplasmonic-Nanofluidic Biosensors with Targeted Delivery of Analytes. *Appl. Phys. Lett.*, 96:021101, 2010.
- [105] A. A. Yanik, M. Huang, O. Kamohara, A. Artar, T. W. Geisbert, J. H. Connor, and H. Altug. An Optofluidic Nanoplasmonic Biosensor for Direct Detection of Live Viruses from Biological Media. *Nano Lett.*, 10(12):4962–4969, 2010.
- [106] G. Raschke, S. Kowarik, T. Franzl, C. Sönnichsen, T. A. Klar, J. Feldmann, A. Nichtl, and K. Kürzinger. Biomolecular Recognition Based on Single Gold Nanoparticle Light Scattering. *Nano Lett.*, 3(7):935–938, 2003.
- [107] D. Buso, G. Busato, M. Guglielmi, A. Martucci, V. Bello, G. Mattei, P. Mazzoldi, and M. L. Post. Selective Optical Detection of H₂ and CO with SiO₂ Sol–Gel Films Containing

- NiO and Au Nanoparticles. *Nanotechnology*, 18(47):475505, 2007.
- [108] S. Szunerits and R. Boukherroub. Sensing Using Localised Surface Plasmon Resonance Sensors. *Chem. Commun.*, 48:8999–9010, 2012.
- [109] M. Ando, T. Kobayashi, S. Iijima, and M. Haruta. Optical CO Sensitivity of Au–CuO Composite Film by Use of the Plasmon Absorption Change. *Sens. Actuators B*, 96:589–595, 2003.
- [110] L. E. Kreno, J. T. Hupp, and R. P. van Duyne. Metal - Organic Framework Thin Film for Enhanced Localized Surface Plasmon Resonance Gas Sensing. *Anal. Chem.*, 82:8042–8046, 2010.
- [111] C. Rosman, J. Prasad, A. Neiser, A. Henkel, J. Edgar, and C. Sönnichsen. Multiplexed Plasmon Sensor for Rapid Label-Free Analyte Detection. *Nano Lett.*, 13:3243–3247, 2013.
- [112] D. A. Stuart, J. M. Yuen, N. Shah, O. Lyandres, C. R. Yonzon, M. R. Glucksberg, J. T. Walsh, and R. P. van Duyne. In Vivo Glucose Measurement by Surface-Enhanced Raman Spectroscopy. *Anal. Chem.*, 78:7211–7215, 2006.
- [113] J. M. Weissman, H. B. Sunkara, A. S. Tse, and S. A. Asher. Thermally Switchable Periodicities and Diffraction from Mesoscopically Ordered Materials. *Science*, 274:959–960, 1996.
- [114] T. Tanaka, D. Fillmore, S.-T. Sun, I. Nishio, G. Swislow, and A. Shah. Phase Transitions in Ionic Gels. *Phys. Rev. Lett.*, 45(20):1636–1639, 1980.
- [115] K. Kataoka, H. Koyo, and T. Tsuruta. Novel pH-Sensitive Hydrogels of Segmented Poly(amine ureas) Having a Repetitive Array of Polar and Apolar Units in the Main Chain. *Macromolecules*, 28:3336–3341, 1995.

- [116] K. Lee and S. A. Asher. Photonic Crystal Chemical Sensors: pH and Ionic Strength. *J. Am. Chem. Soc.*, 122(39):9534–9537, 2000.
- [117] V. L. Alexeev, A. C. Sharma, A. V. Goponenko, S. Das, I. K. Lednev, C. S. Wilcox, D. N. Finegold, and S. A. Asher. High Ionic Strength Glucose-Sensing Photonic Crystal. *Anal. Chem.*, 75:2316–2323, 2003.
- [118] S. A. Asher, S. F. Peteu, C. E. Reese, X. Lin, and D. Finegold. Polymerized Crystalline Colloidal Array Chemical-Sensing Materials for Detection of Lead in Body Fluids. *Anal. Bioanal. Chem.*, 373(7):632–638, 2002.
- [119] T. Miyata, N. Asami, and T. Urugami. A Reversibly Antigen-Responsive Hydrogel. *Nature*, 399:766–769, 1999.
- [120] M. Watanabe, T. Akahoshi, Y. Tabata, and D. Nakayama. Molecular Specific Swelling Change of Hydrogels in Accordance with the Concentration of Guest Molecules. *J. Am. Chem. Soc.*, 120:5577–5578, 1998.
- [121] G. Odian. *Principles of polymerization*. Wiley-Interscience, Hoboken, NJ, fourth edition, 2004.
- [122] L. I. Bosch, T. M. Fyles, and T. D. James. Binary and ternary phenylboronic acid complexes with saccharides and Lewis bases. *Tetrahedron*, 60:11175–11190, 2004.
- [123] J. H. Holtz and S. A. Asher. Polymerized colloidal crystal hydrogel films as intelligent chemical sensing materials. *Nature*, 389:829–832, 1997.
- [124] W. J. Moore. *Physikalische Chemie*. de Gruyter, Berlin [u.a.], fourth edition, 1986.
- [125] Y.-J. Lee, S. A. Pruzinsky, and P. V. Braun. Glucose-Sensitive Inverse Opal Hydrogels: Analysis of Optical Diffraction Response. *Langmuir*, 20(8):3096–3106, 2004.

- [126] D. Roy, J. N. Cambre, and B. S. Sumerlin. Triply-responsive boronic acid block copolymers: solution self-assembly induced by changes in temperature, pH, or sugar concentration. *Chem. Commun.*, pages 2106–2109, 2009.
- [127] N. Liu, T. Weiss, M. Mesch, L. Langguth, U. Eigenthaler, M. Hirscher, C. Sönnichsen, and H. Giessen. Planar Metamaterial Analogue of Electromagnetically Induced Transparency for Plasmonic Sensing. *Nano Lett.*, 10:1103–1107, 2010.
- [128] C. Zhang, M. D. Losego, and P. V. Braun. Hydrogel-Based Glucose Sensors: Effects of Phenylboronic Acid Chemical Structure on Response. *Chem. Mater.*, 25(15):3239–3250, 2013.
- [129] G. Decher and J.-D. Hong. Buildup of ultrathin multilayer films by a self-assembly process: I. consecutive adsorption of anionic and cationic bipolar amphiphiles on charged surfaces. *Makromol. Chem. Macromol. Symp.*, 46:321–327, 1991.
- [130] G. Decher, J. D. Hong, and J. Schmitt. Buildup of ultrathin multilayer films by a self-assembly process: III. Consecutively alternating adsorption of anionic and cationic polyelectrolytes on charged surfaces. *Thin Solid Films*, 210-211:831–835, 1992.
- [131] J. J. Richardson, M. Björnmalm, and F. Caruso. Technology-driven layer-by-layer assembly of nanofilms. *Science*, 348(6233):aaa2491, 2015.
- [132] S. Li, E. N. Davis, J. Anderson, Q. Lin, and Q. Wang. Development of Boronic Acid Grafted Random Copolymer Sensing Fluid for Continuous Glucose Monitoring. *Biomacromolecules*, 10(1):113–118, 2009.
- [133] Z. Ding, Y. Guan, Y. Zhang, and X. X. Zhu. Layer-by-layer multilayer films linked with reversible boronate ester bonds with glucose-sensitivity under physiological conditions. *Soft Matter*, 5:2302–2309, 2009.

- [134] X. Zhang, Y. Guan, and Y. Zhang. Ultrathin Hydrogel Films for Rapid Optical Biosensing. *Biomacromolecules*, 13:92–97, 2012.
- [135] R. Gabai, N. Sallacan, V. Chegel, T. Bourenko, E. Katz, and I. Willner. Characterization of the Swelling of Acrylamidophenylboronic Acid - Acrylamide Hydrogels upon Interaction with Glucose by Faradaic Impedance Spectroscopy, Chronopotentiometry, Quartz-Crystal Microbalance (QCM), and Surface Plasmon Resonance (SPR) Experiments. *J. Phys. Chem. B*, 105:8196–8202, 2001.
- [136] H. V. Hsieh, Z. A. Pfeiffer, T. J. Amiss, D. B. Sherman, and J. B. Pitner. Direct Detection of Glucose by Surface Plasmon Resonance with Bacterial Glucose/Galactose-Binding Protein. *Biosens. Bioelectron.*, 19:653–660, 2004.
- [137] A. Ersöz, A. Denizli, A. Özcan, and R. Say. Molecularly Imprinted Ligand-Exchange Recognition Assay of Glucose by Quartz Crystal Microbalance. *Biosens. Bioelectron.*, 20:2197–2202, 2005.
- [138] V. L. Alexeev, S. Das, D. N. Finegold, and S. A. Asher. Photonic Crystal Glucose-Sensing Material for Noninvasive Monitoring of Glucose in Tear Fluid. *Clin. Chem.*, 50(12):2353–2360, 2004.
- [139] Roux, C. and Maynard, P. and Dawson, M. Ftir spectroscopy applications in forensic science. *Chem. Aust.*, 66:11–15, 1999.
- [140] J. M. Chalmers, editor. *Handbook of vibrational spectroscopy*. Wiley, Chichester; Weinheim [u.a.], 2002.
- [141] F. Neubrech and A. Pucci. Plasmonic Enhancement of Vibrational Excitations in the Infrared. *IEEE J. Sel. Top. Quant.*, 19:4600809, 2013.
- [142] F. Neubrech, S. Beck, T. Glaser, M. Hentschel, H. Giessen, and A. Pucci. Spatial Extent of Plasmonic Enhancement of Vibrational Signals in the Infrared. *ACS Nano*, 8(6):6250–6258, 2014.

- [143] F. Schreiber. Structure and growth of self-assembling monolayers. *Prog. Surf. Sci.*, 65:151–256, 2000.
- [144] E. K. Seo, J. W. Lee, H. M. Sung-Suh, and M. M. Sung. Atomic Layer Deposition of Titanium Oxide on Self-Assembled-Monolayer-Coated Gold. *Chem. Mater.*, 16:1878–1883, 2004.
- [145] D. Barriet, C. M. Yam, O. E. Shmakova, A. C. Jamison, and T. R. Lee. 4-Mercaptophenylboronic Acid SAMs on Gold: Comparison with SAMs Derived from Thiophenol, 4-Mercaptophenol, and 4-Mercaptobenzoic Acid. *Langmuir*, 23:8866–8875, 2007.
- [146] M. Lippitz, M. A. van Dijk, and M. Orrit. Third-Harmonic Generation from Single Gold Nanoparticles. *Nano Lett.*, 5:799–802, 2005.
- [147] S. Palomba, M. Danckwerts, and L. Novotny. Nonlinear plasmonics with gold nanoparticle antennas. *J. Opt. A*, 11:114030, 2009.
- [148] S. Palomba, H. Harutyunyan, J. Renger, R. Quidant, N. F. van Hulst, and L. Novotny. Nonlinear plasmonics at planar metal surfaces. *Phil. Trans. R. Soc. A*, 369:3497–3509, 2011.
- [149] T. Utikal, T. Zentgraf, T. Paul, C. Rockstuhl, F. Lederer, M. Lippitz, and H. Giessen. Towards the Origin of the Nonlinear Response in Hybrid Plasmonic Systems. *Phys. Rev. Lett.*, 106:133901, 2011.
- [150] H. Harutyunyan, G. Volpe, R. Quidant, and L. Novotny. Enhancing the Nonlinear Optical Response Using Multifrequency Gold-Nanowire Antennas. *Phys. Rev. Lett.*, 108:217403, 2012.
- [151] M. Kauranen and A. V. Zayats. Nonlinear plasmonics. *Nat. Photonics*, 6:737–748, 2012.
- [152] M. F. Ciappina, S. S. Aćimović, T. Shaaran, J. Biegert, R. Quidant, and M. Lewenstein. Enhancement of high

- harmonic generation by confining electron motion in plasmonic nanostructures. *Optics Express*, 20(24):26261–26274, 2012.
- [153] T. Hanke, J. Cesar, V. Knittel, U. Hohenester, A. Leitenstorfer, and R. Bratschitsch. Tailoring Spatiotemporal Light Confinement in Single Plasmonic Nanoantennas. *Nano Lett.*, 12:992–996, 2012.
- [154] S. S. Aćimović, M. A. Ortega, V. Sanz, J. Berthelot, J. L. Garcia-Cordero, J. Renger, S. J. Maerkl, M. P. Kreuzer, and R. Quidant. LSPR Chip for Parallel, Rapid, and Sensitive Detection of Cancer Markers in Serum. *Nano Lett.*, 14:2636–2641, 2014.
- [155] Y. Khalavka, J. Becker, and C. Sönnichsen. Synthesis of Rod-Shaped Gold Nanorattles with Improved Plasmon Sensitivity and Catalytic Activity. *J. Am. Chem. Soc.*, 131:1871–1875, 2009.
- [156] S. S. Aćimović, M. P. Kreuzer, M. U. González, and R. Quidant. Plasmon near-field coupling in metal dimers as a step toward single-molecule sensing. *ACS nano*, 3(5):1231–1237, 2009.
- [157] M. W. Klein, T. Tritschler, M. Wegener, and S. Linden. Lineshape of harmonic generation by metallic nanoparticles and metallic photonic crystal slabs. *Phys. Rev. B*, 72:115113, 2005.
- [158] B. Metzger, M. Hentschel, M. Lippitz, and H. Giessen. Third-harmonic spectroscopy and modeling of the nonlinear response of plasmonic nanoantennas. *Opt. Lett.*, 37:4741–4743, 2012.
- [159] Feynman, R. P. and Leighton, R. B. and Sands, M. *The Feynman Lectures on Physics*. Addison-Wesley, Reading, Mass., fifth edition, 1970.
- [160] M. Siviš, M. Duwe, B. Abel, and C. Ropers. Extreme-ultraviolet light generation in plasmonic nanostructures. *Nat. Phys.*, 9:304–309, 2013.

- [161] C. Langhammer, I. Zoric, B. Kasemo, and B. M. Clemens. Hydrogen Storage in Pd Nanodisks Characterized with a Novel Nanoplasmonic Sensing Scheme. *Nano Lett.*, 7:3122–3127, 2007.
- [162] N. Strohhfeldt, A. Tittl, and H. Giessen. Long-term stability of capped and buffered palladium-nickel thin films and nanostructures for plasmonic hydrogen sensing applications. *Opt. Mater. Express*, 3:151–157, 2013.
- [163] J. Butet and O. J. F. Martin. Refractive index sensing with Fano resonant plasmonic nanostructures: a symmetry based nonlinear approach. *Nanoscale*, 6:15262–15270, 2014.
- [164] J. Butet and O. J. F. Martin. Nonlinear Plasmonic Nanorulers. *ACS Nano*, 8(5):4931–4939, 2014.
- [165] S. Shen, L. Meng, Y. Zhang, J. Han, Z. Ma, S. Hu, Y. He, J. Li, B. Ren, T.-M. Shih, Z. Wang, Z. Yang, and Z. Tian. Plasmon-Enhanced Second-Harmonic Generation Nanorulers with Ultrahigh Sensitivities. *Nano Lett.*, 15:6716–6721, 2015.
- [166] S. Roke and G. Gonella. Nonlinear Light Scattering and Spectroscopy of Particles and Droplets in Liquids. *Annu. Rev. Phys. Chem.*, 63:16.1–16.26, 2012.



ACKNOWLEDGMENTS

Like many things in life this thesis and the work presented therein could not have been accomplished by one sole person. Therefore I am deeply grateful to many people who contributed scientifically or in one of many other ways, and accompanied me during this time:

- Prof. Dr. Harald Giessen for giving me the opportunity to work at his institute, for his advice, all the contacts he made, and his general support.
- Prof. Dr. Martin Dressel and Prof. Dr. Christian Holm for taking their time and kindly agreeing to be part of my examination committee.
- Prof. Dr. Paul V. Braun and Chunjie Zhang for introducing me to hydrogels, many helpful discussions, as well as for the pleasant and productive stay at University of Illinois at Urbana-Champaign.
- Prof. Dr. Cristina Tarin, Tanja Teutsch and Philipp Rapp for the good collaboration in the context of the Ideenwettbewerb Biotechnologie und Medizintechnik and the following proposals and projects.
- Prof. Dr. Ravi Hegde for the collaboration regarding perturbation theory and his expertise on CST simulations.
- Dr. Timo Gissibl for the great time we had in our office and beyond.
- Dr. Mario Hentschel who provided essential help and good advice at numerous occasions and was involved in virtually every project.
- Dr. Bernd Metzger for the excellent team work in the Nonlinear Plasmonic Sensing project.

- Dr. Frank Neubrech for many fruitful discussions, particularly on sensing, his support with the SEIRA project and his help with organizing the SCoPE volleyball tournament.
- Dr. Richard Taubert and Dr. Daniel Drégely for a great time.
- Dr. Martin Schäferling for all the bright and dark times we had with IT administration.
- Dr. Christine von Rekowski for her help with all administrative tasks.
- Monika Ubl for her support in the chemistry lab and in the MSL.
- Ralf Kamella and his team of the mechanical workshop for the precise work, particularly for the sensor cell.
- All current and former members of the 4th Physics Institute for the nice working atmosphere.
- My sister Maria for her support with all the chemical issues of my work and our frequent exchange about life as a PhD student in science.
- My brother Matthias for adding variety to the scientific daily routine with music, sailing or other shared activities.
- My parents Christa and Johann Mesch for more than 30 years of unconditional support in every possible sense.
- My fiancé Larissa who shares all the good and bad times with me and somehow always manages to successfully encourage me.



COLOPHON

This document was typeset with L^AT_EX 2_ε using Hermann Zapf's *Palatino* type face. The layout is based on the typographical look-and-feel `classicthesis` developed by André Miede.